Sulphide Stress Cracking in X80 Pipeline Steel Weld Metals

by

Yuji Kisaka

A thesis
presented to the University of Waterloo
in fulfillment of the
thesis requirement for the degree of
Doctor of Philosophy
in
Mechanical and Mechatronics Engineering

Waterloo, Ontario, Canada, 2020

Examining Committee Membership

The following served on the Examining Committee for this thesis. The decision of the Examining Committee is by majority vote.

Supervisors   Adrian Gerlich, PhD

                                 Associate Professor, Mechanical and Mechatronics Engineering,

                                 University of Waterloo

External Examiner   Michel Guillot, PhD

                                 Professor, Department of Mechanical Engineering, Laval University

Internal Examiner   Mary Wells, PhD

                                 Professor, Mechanical and Mechatronics Engineering, University of Waterloo

Internal Examiner   Carolyn Hansson, PhD

                                 Professor, Mechanical and Mechatronics Engineering, University of Waterloo

Internal/External Examiner   Stan Potapenko, PhD

                                 Associate Professor, Civil and Environmental Engineering,

                                 University of Waterloo

Author's Declaration

This thesis consists of material all of which I authored or co-authored: see Statement of Contributions included in the thesis. This is a true copy of the thesis, including any required final revisions, as accepted by my examiners.

I understand that my thesis may be made electronically available to the public.

Statement of Contributions

The following co-authors have contributed to the current work:

- Professor Adrian P. Gerlich supervised this work.

- Dr. Nick Senior who is a corrosion research scientist in CanmetMaterials conducted Sulphide Stress Cracking test mentioned in Chapter 3 and thermal desorption analysis in Chapter 4.

- Dr. Abdelbaset Midawi helped producing all weld joints shown in Chapter 2, Chapter 3, and Chapter 4, performing tensile test applying Digital Image Correlation mentioning in Chapter 4, and lectured me how to use welding equipment, cutting machine, hardness test machine, etc.

- Dr. Nazmul Huda also helped performing tensile test applying Digital Image Correlation shown in Chapter 4, Scanning Electron Microscopy works mentioned in Chapter 4, and lectured me how to use welding equipment, cutting machine, hardness test machine, etc.

- The EM research described in Chapter 2 and Chapter 3 and Chapter 4 was performed at the Canadian Centre for Electron Microscopy at McMaster University, which is supported by NSERC and other government agencies.

- The balance of the research is my own work.

Abstract

The utilization of high strength linepipes provides various benefits, including reducing construction cost, and operational cost. On the other hand, the girth welds for such pipelines are welded onsite, and simultaneously require strength overmatching of the weld joint, high fracture toughness, and low hardness, regardless of whether these mechanical properties are potentially at odds with each other. Moreover, hardness in the welds must be maintained below HV250 for high strength pipe grades used in natural gas pipelines if they are used for severe sour service applications, where severe sour is defined as SSC region 3 in the NACE standard MR0175/ISO 15156, as the range where H_2S partial pressure exceeds 1 kPa, and below a pH of 3.5, and above 100 kPa and below a pH of 5.5. Thus, it is very difficult to employ high strength pipeline materials such as those exceeding API X70 grade for such applications.

This particular hardness criterion has been standardized by NACE standard MR0175/ISO 15156 and European Federation of Corrosion publication number 16 (EFC No.16) to avoid sulphide stress cracking (SSC) initiation, and was determined by experience and testing; however, the tests had been performed several decades ago on rather different steel chemistries than those used today. Since recent steels and weld metals have significantly different chemical composition and grain size, thus this hardness criterion has become controversial. Meanwhile, some recent research papers mention that acicular ferrite is one of the fine microstructures and argued that intragranular can improve resistance to hydrogen embrittlement. Thus, the present work evaluates these issues on API X80 grade weld metals. This involves establishing a control method of acicular ferrite volume fraction in the weld metals. The relationship between kinds of microstructures and SSC susceptibility for GMA weld metals is then compared to validate a critical hardness value. The actual microstructural features which provide a hydrogen trap mechanism in particular are demonstrated for the acicular ferrite microstructure in the GMA weld metal, by using a combination of electron microscopy and hydrogen

micro-printing. The role of microstructure on SSC susceptibility and the influence of hydrogen charging on strength and hardness properties are then compared.

The results show that it was possible to produce X80 grade weld metals with differing intragranular ferrite (acicular ferrite) volume fractions, by controlling the relationship between the titanium and oxygen ratio. The most effective balance between titanium and oxygen contents for maximizing intragranular ferrite corresponds to an ideal stoichiometry of Ti_2O_3. Next, SSC tests are performed in accordance with NACE MR0175/ISO 15156 (using a test solution) based on the (3 and 4 points bending method) on this material with varying intragranular ferrite volume fraction. These results confirm that weld metals exceeding 98% intragranular ferrite volume fraction and low grain boundary ferrite are able to pass the SSC test even if their hardness value exceeded 250HV. Furthermore, in order to reveal the roles of intragranular ferrite microstructure for SSC susceptibility, the hydrogen microprint technique combined with Scanning Electron Microscopy observation was used to compare the microstructures of specimens which passed and failed the SSC test. It was confirmed that grain boundaries within the intragranular ferrite are effective hydrogen trapping sites, and it appeared that nano-carbides prevent motion of dislocations which carrying diffusible hydrogen. Moreover, intragranular ferrite exhibits high toughness due to fine grains which promote crack deflection more effectively than grain boundary ferrite. Thus, it is suggested that intragranular ferrite can increase SSC resistance based on these mechanisms resulting from the desirable microstructural features. Finally, mechanical properties, such as tensile behaviour was investigated following hydrogen charging for two weld metals with differing intragranular ferrite volume fractions. The stress-strain curves for weld metals involving a higher intragranular ferrite volume fraction were less affected by hydrogen compared to the case of low intragranular volume fraction, and this is attributed to the difference of hydrogen trapping as revealed by thermal desorption analysis. In conclusion, this research proposes that intragranular ferrite dominant structures in high strength steels can decrease

SSC susceptibility and stabilize mechanical properties in sour environments by providing strong trapping sites.

Acknowledgements

Table of Contents

List of Figures

List of Tables

Chapter 1
Introduction and literature review

1.1 Background and history of hardness guideline to avoid sulphide stress cracking

Transporting natural gas via pipelines is one of the economical modes of energy transmission. Utilizing high strength steels for linepipes provides many benefits such as reducing construction and operational costs, since thinner wall thickness pipes can be applied in place of low grade and thicker linepipes are employed. This makes it possible to save material costs and leads to the reduction of construction cost in terms of welding time at construction sites, which involves labor intensive girth welding for connecting individual sections of pipes. Also, when high strength steel linepipes are used, pressure for the gas transportation can be increased during operation. This clearly improves efficiency in gas transportation; hence reducing operational cost. Therefore, steel providers and pipeline contractors have developed high strength steels and welding procedures for new construction projects for over the past few decades.

When a pipeline is constructed, onsite girth welding is performed typically by using automatic/mechanized welding machines moving in an orbital manner around the pipes. This girth weld requires strength overmatching (owning higher strength than the base material), high fracture toughness, while also maintaining hardness below a critical value. These mechanical properties are potentially at odds with each other, making it difficult to satisfy required standards. On the other hand, if new natural gas pipelines are constructed for severe sour service, then sulphide stress cracking (SSC) becomes a concern, where severe sour service is defined as SSC region 3 in NACE standard MR0175/ISO 15156 [1], H_2S partial pressure exceeds 1kPa and pH is below than 3.5, or when the pH is below 4.5 when the pressure H_2S partial pressure is 10kPa, or below a pH of 5.5 when the H_2S partial pressure exceeds 100 kPa. It is well known that SSC occurs through a series of steps as follows [1]. First, hydrogen atoms which are included in water and in natural gas contact the inner surface of the pipes, and these will either stay near the surface or diffuse into the pipe wall by

a chemical reaction. Next, absorbed hydrogen atoms can diffuse into the steels and will be trapped at preferred sites with defects, which elevate the hardness in the microstructure such as impurities, dislocations, and grain boundaries, leading to accumulation of hydrogen. Finally, SSC occurs from this hydrogen accumulating area once the hydrogen concentration reaches the crack initiation limit and a tensile stress is introduced, which provides a trigger for the crack initiation. The mechanism is similar to hydrogen crack, which forms after the absorption of hydrogen atoms. Hence, it has been recognized that reducing hardness is the most effective way to prevent SSC initiation. Therefore, in the case of construction of pipelines for a severe sour environment, utilizing high strength linepipe will be more difficult because the increasing priority for low hardness is at odds with the increased material strength.

As a common hardness guideline, NACE standard MR0175/ISO 15156 [2] and European Federation of Corrosion publication number 16 (EFC No.16) [3], both require the maximum hardness of the materials including welds to be below 250 Vickers regardless of pipe grade, and this has been widely applied since their inception. This hardness criterion, however, has become more controversial in recent years. Originally, NACE MR0175 was established in 1975 by the National Association of Corrosion Engineers (NACE), which is an organization for corrosion in US. The hardness criterion has been applied without major modifications since the first issue, with few revisions issued over the last 40 years, and this has been part of the reason for recent debate over its current validity [4]. Reviewing the history of this criterion, one can better appreciate why its application has come under scrutiny.

According to Patrick, the starting point for this standard arose from two accidents in west Texas in the US in the late 1940's to 50's and western Canada in the 1950's [5]. Following these events, NACE established one committee chaired by R.S. Treseder, and the committee investigated in order to clarify the problem and they proposed a possible solution over the 1960's. Finally, the T-

1F group which is a committee organized a report called 1F166 (Sulphide Cracking Resistant Metallic for Valves for Production and Pipeline Service) in 1966 [5]. At that time, the maximum hardness criterion in order to avoid sulphide stress cracking was suggested [6]. Following this, NACE issued the MR0175 recommendations in 1975, which initially mentioned only valve components, however the applicable hardness range was extended for all components involving sour-gas-containing wells when revised in 1978. Later, revisions addressed only minor changes, including the addition of new materials including corrosion resistance alloy (CRA) material [5].

One should consider that this original hardness criterion was proposed in 1966, based on experience with steels from the 1960's which significantly differ in chemical compositions and mechanical properties compared to recent linepipe steels. Typically, steels in the 1960's could contain high carbon contents exceeding 0.1 wt.%, coarser grain sizes, and significantly different microstructures compared to modern steels produced with thermo-mechanical-control-process technology (TMCP). Furthermore, although the hardness criterion has been applied to weld metals without unconditionally, the microstructures in weld metals are also drastically different from the base materials since the oxygen content in weld metal is normally much higher. Moreover, weld metals in the past are also quite different compared to most recent pipeline weld metals which contain finer acicular ferrite microstructures, which is achieved by utilizing titanium and oxidation developed in the 1980's, many years after publishing the 1F166 document.

From the history regarding the origin of the hardness criterion, progress in steel production, and welding technologies, the present work argues that the SSC susceptibility criteria based on hardness should be re-considered from the standpoint of how the volume fraction of trapping sites, distribution of hard regions related to impurities, and carbon content, rather than simply hardness value. Moreover, the grain size and the kind of microstructure should also affect SSC susceptibility since hydrogen permeability and diffusivity are all directly contributing to SSC susceptibility.

It is suggested that this hardness criterion is unreasonably strict for high strength weld metals, since it has been intended for evaluating base metals. In contrast, pipeline welds are required strength overmatching to avoid fracture starting from the weld metals, which implies that the weld metals must be inherently harder than the base metals. Hence, it is worth evaluating the relevance of the hardness criterion for weld metals, since diligence requires that engineering standards should be discussed and re-evaluated with historical circumstances in perspective.

Based on a review of the recent literature in this area, three methods can be considered to provide SSC resistance for pipeline welds (which may even exceed the critical hardness) as follows; 1) reducing impurities that would produce hard phases that gather diffusible hydrogen, 2) producing fine and homogeneous grain structures in order to increase the resistance to crack initiation and propagation, 3) controlling microstructures in the welds in order to maximize regions with high hydrogen permeability, solubility, and low diffusivity. In the following section, a literature review related to these three methods will be presented, and the objectives for the present work will be defined.

1.2 Microstructures, roles of chemistries, and cooling rate

1.2.1 Microstructures

This section explains the different microstructures for steels, which often appear in actual pipeline materials and this thesis, as shown in **Figure 1-1**. According to Thewlis, each microstructure is defined as follows [7]. First of all, grain boundary ferrite (GBF) is defined as allotriomorphic ferrite located at prior austenitic grain boundaries [7]. Next, intragranular ferrite referred to as acicular ferrite has three forms: polygonal ferrite, Widmanstätten ferrite, and bainitic ferrite [7]. Polygonal ferrite has polygonal and blocky or equiaxed shape, and forms in the intra-grain locations [7]. Widmanstätten ferrite has a sharp shape and is often randomly oriented within prior austenite grains [7].
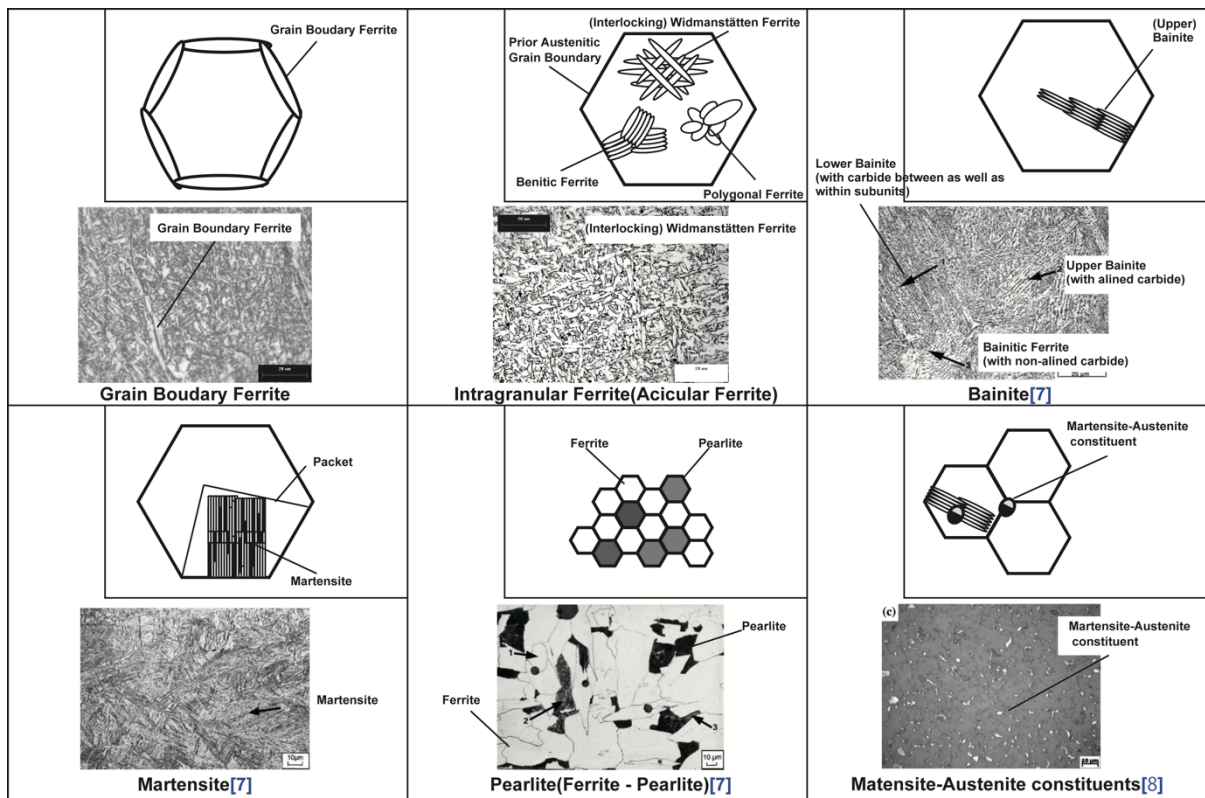
Figure 1-1 Microstructures for steels which often appear in high strength pipeline weld metals, along with the respective examples from the literature.

The last form is bainitic ferrite, which may nucleate from intragranular inclusions or prior austenitic grain boundaries, or by sympathetic nucleation on the ferrite/bainite interfaces, and exhibits a primary feature in which carbide particles are not aligned [7]. On the other hand, bainite has aligned carbide in the structure as well as the nucleation grows from grain boundaries [7]. A visible feature of martensite is highly concentrated carbon shown as dark lath shape in this structure, which are caused by insufficient carbon diffusion resulting from rapid cooling. Martensite has a character which high strength and low fracture toughness typically. Ferrite/pearlite structures can be found in low strength steels (base metals). Pearlite is also generated as a result of carbon segregation, but the carbon concentration is lower than within martensite because of slow cooling. Finally, Martensite-austenite (MA) constituents are grains which have a martensite and retained austenite mixture in their interior structure. Typically, this is generated with rapid cooling from two-phase region between austenite and ferrite, so generally, this appears in heat affected zone (in base metal) and heat affected previous weld pass.

1.2.2 Roles of Alloying elements

In the case of weld metals, microstructures are determined by chemical composition and cooling rate during the austenite to ferrite transformation that typically occurs below 900℃. In this section, the roles of each chemical element added to pipeline weld metals is explained. It can be noted that the chemical composition for weld metals are determined as a result of dilution of base metals and welding consumables, in the case of utilizing welding consumable such Gas Metal Arc (GMA) welding.

Carbon: Carbon increases the yield strength and tensile strength and hardness by forming carbide. On the other hand, excessive carbon content reduces ductility and fracture toughness. Furthermore, it may increase hardenability and reduce weldability, so this may lead to increase risks of both hot crack and cold crack initiation [9-12].

Silicon: Silicon increase strength and hardness by solid solution mechanisms. In addition, silicon acts as a strong reduction element. Therefore, it is added to control oxygen content in a weld metal, typically [9-10,12-13].

Manganese: Manganese also increases strength and hardness. In addition, suitable amount of manganese can increase fracture toughness as it can promote acicular ferrite nucleation [9-10,14-15].

Sulphur: Sulphur is basically an impurity in steels, and is a known low melting point element, often causing hot cracking. On the other hand, Sulphur can promote a smooth weld bead shape, lead to deeper penetration due to reduction of surface tension of molten pool [10, 16].

Nickel: Nickel increases yield and tensile strength by the solid solution mechanism. Furthermore, it especially improves fracture toughness, however, the element cost is expensive. Nickel is also a strong austenite stabilizer, typically added to austenitic stainless steels for example [9-10, 13, 15].

Chromium: Chromium increases strength and hardness due to formation of stable carbides. Up to 1% chromium leads to a bainitic microstructure with high strength, but reduced fracture toughness [9-10, 13].

Vanadium: Vanadium offers strengthening by forming fine carbide and nitride precipitates. This can prevent austenite grain growth in previous weld metals and heat affected zone during heating up by multi pass welding since it disperses at austenitic grain boundaries [9-10, 13, 17].

Niobium: Niobium also improves strength, especially yield strength. It typically leads to formation of NbC, which have a similar effect as vanadium carbides [9-10, 17-20].

Titanium: Titanium acts as strong reduction element and improve yield strength and tensile strength by generating acicular ferrite. Titanium typically forms nitrides like TiN, oxide such as TiO, TiO_2, and Ti_2O_3, which then form nucleation sites of acicular ferrite [9-10, 19, 21-22].

Boron: Boron acts as strong hardenability element. This element disperses at austenitic grain boundaries and prevents growth of grain boundary ferrite. Adding a suitable amount leads to

improved fracture toughness by promoting intragranular ferrite; however, excessive inclusions deteriorate toughness due to martensite formation [9-10, 13, 23-24].

Molybdenum: Molybdenum can improve strength and facture toughness simultaneously by precipitation strengthening particularly in combination with Niobium. In addition, Molybdenum shows excellent recovery rate (ie: alloying efficiency from the wire chemistry) since it does not combine readily with oxygen and nitrogen [9-10, 13, 24-25].

Oxygen: Suitable amounts of oxygen are necessary to balance with titanium content and improve fracture toughness and strength due to formation of acicular ferrite, characterized by a fine grain size. It is well known that titanium oxide dispersing at intragrain locations acts as nucleation site of intragranular ferrite. On the other hand, excessive oxygen deteriorates fracture toughness due to larger sized inclusions which can be a crack nucleation site [9-10, 12-14, 26-27].

Nitrogen: Nitrogen is typically undesirable due to decreasing fracture toughness and porosity which is one of the common weld flaws. Normally, in order to prevent nitridation (including oxidation), the molten pool will be shielded by an inert gas like argon [9-10, 13, 19].

1.2.3 Influence of cooling rate in weld metals

As mentioned at the previous section (1.2.2), the microstructures in weld metals are determined by both chemical composition and cooling rate. Especially in the case of steels, cooling rates in the range of approximately 800 to 500 ℃ are important because steels typically experience the characteristic transformation of austenite to other phases in that temperature range. It is well known that in the case of slow cooling, the equilibrium microstructure will be generated in accordance with typical iron-carbon phase diagram. On the other hand, the microstructure determined by continuous cooling temperature (CCT) diagram is used to describe the case of rapid cooling rate.

An example CCT diagram is illustrated in **Figure 1-2**. It should be noted that a cooling curve is continuous cooling rate due to the log scale on the horizontal axis in this figure. The lines to indicate each ferrite, bainite, and martensite initiation depending on chemical composition in materials, where the materials mean deposit metals mixed with a base metal, welding consumable, and shielding gas in the case of weld metals. In order to generate acicular ferrite, the chemical composition and cooling rate should be controlled to cross the initiation line for acicular ferrite. For the weld metals, although chemical composition can be controlled easily through the composition of the welding consumable and shielding gas, the cooling rate controlling is difficult since one cannot use furnaces, or chill water for cooling as in the case of steel production. Normally, in a welding process we can only vaguely affect the peak temperature and approximate cooling rate by controlling the welding parameters and maintaining the preheating and interpass temperature.
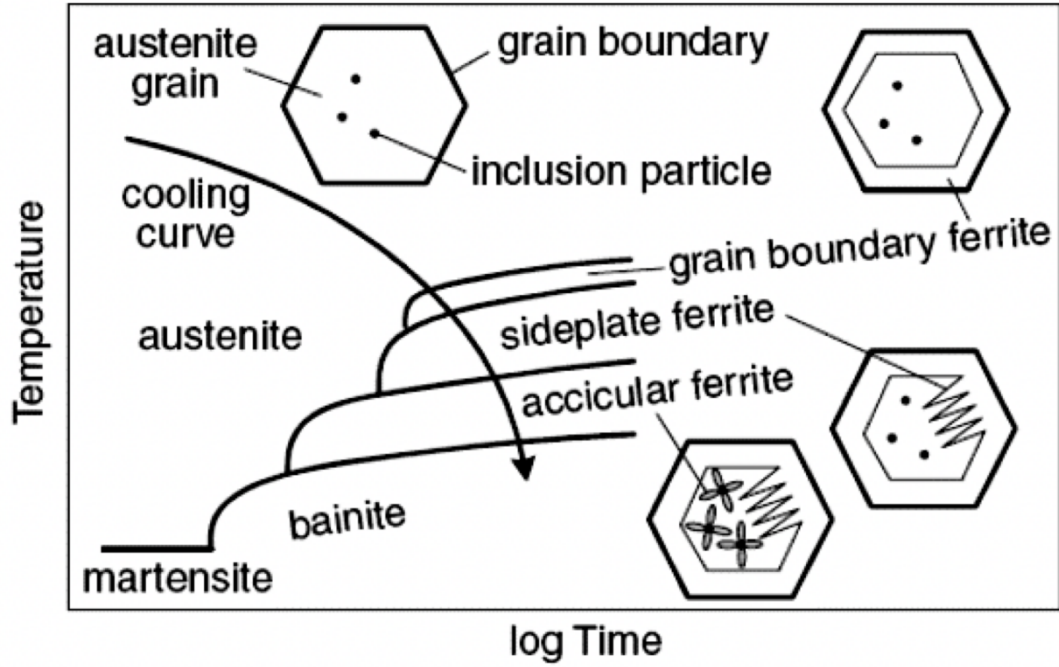
Figure 1-2 Schematic representation of microconstituents expected in a CCT diagram for typical high

strength low alloy steels [9, 28]

1.3 Sulphide stress cracking

Sulphide stress cracking (SSC) is one form of hydrogen cracking, and the NACE standard MR0175/ISO 15156 defines the cracking as follows: "SSC is a form of hydrogen stress cracking and involves embrittlement of the metal by atomic hydrogen that is produced by acid corrosion on the metal surface"[2]. Basically, the crack is caused by an environment containing hydrogen sulphide gas in the case of gas pipelines. The hydrogen sources come from natural gas and moisture in the gas by cathodic reaction onto the inside surface of the pipe. Some of the absorbed hydrogen atoms will migrate through grain boundaries and will be transported via dislocations, though some diffusible hydrogen will be trapped at hard phases such as precipitates and compounds etc. Finally, SSC initiates if embrittlement of the material by the accumulating hydrogen exceeds the limit of crack initiation and tensile stresses are induced. The mechanism is similar to stress corrosion cracking (SCC) although the mechanism of introducing hydrogen differs. The cracking mechanism is similar to hydrogen induced cracking (HIC) or stress oriented hydrogen induced cracking (SOHIC) [29]. HIC occurs regardless of welding as it does not require applied or residual stresses.

In comparison, the HIC process occurs when a crack initiates at the middle thickness of materials and propagates in a parallel direction to material surface along impurities such as manganese sulfide. Cracks occur by expansion when hydrogen atoms accumulate at impurities and form molecules. Typically, the high level of impurities are formed by the rolling process in steel production. By contrast, SSC is initiated or triggered by a tensile stress as mentioned above. Typically, large welds in steel members have residual stress if there was no post welding heat treatment (PWHT) applied. This residual stress will be a trigger so that SSC may happen; thus, the occurrence of HIC in weld metals should be difficult. SOHIC occurs by combining some HICs with tensile stress, which may often be resulting from residual stresses, as in the case of welding joints, especially those which contain impurities.

1.4 Circumferential welding at on-site for pipeline constructions

Many welding methods for on-site circumferential welding have been considered by many researchers in order to improve productivity for a long time, for example, arc welding, laser welding, forge welding, and so on have been investigated [30]. Mechanized dual welding torched gas metal arc welding is most successful method, and it has been widely applied for pipeline constructions [30]. Recently, automatic welding machines that do not need manual welding skills have been developed and applied to many pipeline construction projects [31,32]. This thesis focuses on pipeline welds installed in severe sour environment; these are typically offshore pipelines near natural gas sources; thus, it is worth discussing the methods in offshore pipeline construction. For example, a special barge is used with welding stations, non-destructive test stations, and pipe coating equipment. Welding, non-destructive test, coating operations are performed concurrently, as the barge goes forward, a pipe length distance once the predetermined works at all stations are finished. Those works are repeated to completing the pipeline construction. Pipeline circumferential welds generate residual stress typically because welding is performed while the pipe is fixed in position. According to Lee and Chang, this residual stress level for circumferential welds reach the nearly the yield strength of the base material [33]. Typically, on-site circumferential welding for pipelines has been performed in accordance with a specification regulated by oil and gas providers based on the standards described by API 1104, DNV-GL ST F101, and NACE standard MR0175/ISO 15156. These specifications define the criteria of non-destructive tests, the methodology of mechanical tests including an SSC test in order to evaluate SSC susceptibility, and procedures for conducting welding procedure qualification tests, welder qualification test, and base material acceptance.

1.5 Literature review

1.5.1 Influence of impurities

It is well known that hard inclusions such as impurities like manganese sulphides, carbide, and constituents such as Martensite-austenite (MA) in the materials will be preferential sites for diffusible hydrogen [34], and thus the SSC resistance should be improved by reducing the fraction of these inclusions. This section reviews the role of hard portions for hydrogen embrittlement mechanisms including both SSC and hydrogen induced cracking (HIC), where HIC is one of the hydrogen cracks, the difference between these embrittlement mechanisms being that HIC can initiate without stress [2].

First of all, a review of the base metals will be provided and compared to the weld metals. In the case of base materials, it is known that segregation during casting will lead to formation of manganese sulphides (MnS), which are gathered at the mid-thickness of steels, and often have a flat shape elongated resulting from rolling during steel production. Typically, they have higher hardness than surrounding grains, and can promote HIC. The actual phenomenon in which diffusible hydrogen atoms are accumulated at MnS when a cathode reaction occurs in steels had been observed using a silver decoration method by Shinozaki et al. [35]. Reducing the amount of MnS and changing the morphology of these particles, such as the tip shape, are considered an effective method to avoid HIC. Therefore, the recent linepipe base metals designated as resistant to sour environments are improved by not only reducing sulfur content in the metals but also modifying the tip radius of inclusions by generating CaS through alloying with calcium [1].

Also, it is known that MA constituents act as a preferential site for hydrogen. Typically, this is generated by rapid cooling from the two-phase region where ferrite and austenite are stable, which coincides with temperatures that occur in the heat-affected zone (HAZ) of a weld. MA constituents have features of both hard martensite and soft retained austenite. Completely avoiding MA

14

constituent formation is difficult; however, reducing martensite constituent is possible, and this will be effective in preventing diffusible hydrogen from accumulating, since martensite constituents are one of the main sinks for diffusible hydrogen atoms because of their interaction with the dispersed carbon the body-centered cubic structure. Thus, materials should not include excessive chemical elements which promote martensite formation or increase hardenability. The main indicator of hardenability is usually based on the carbon equivalent, which includes elements aside from carbon such as manganese, chromium and others, and these should be reduced since they will generate martensite and increase hardness. In addition, in the case of welding, preheating and managing interpass temperature during welding are also effective in suppressing martensite transformation.

The SSC susceptibility has been investigated for various pipes, in the grades ranging from API 5L X52 (with a yielding stress exceeding 350 MPA) to API 5L X80 (with a yielding stress exceeding 550MPa) and in various heat treatments such as normalized, thermo-mechanical control process (TMCP), and quench-tempered (QT) by Kermani et al. [36]. The study indicated that low carbon steels demonstrate lower SSC susceptibility compared with high carbon steels, although the high carbon steels examined were actually a lower strength grade than low carbon steels. On the other hand, Omweg et al. had investigated the SSC susceptibility in the HAZ of a X80 pipe weld with low carbon content and compared it to a high carbon X70 pipe, with almost the same carbon equivalent [37]. It was found that the low carbon X80 pipe exhibits higher SSC resistance than the high carbon X70 pipe. Based on this work, it was concluded that reducing carbon will help to improve SSC resistance. The influence of hard phases in the weld metal should also be addressed in terms of SSC susceptibility. A source of impurities such as sulphur should be reduced regardless of base metals and weld metals, due to numerous issues that arise during processing or mechanical testing.

Currently, automatic or mechanized gas metal arc welding (GMAW) is typically applied for on-site welding for pipeline constructions [30-31], where a narrow groove and high welding speeds are

applied to reduce construction time and costs. In that case, impurities such as MnS will segregate at the center of the weld bead, which is the region of final solidification, since a narrower groove promotes columnar grain solidification towards the centerline [32]. Segregated impurities formed by welding do not have a sharp elongated shape since no rolling process is applied, however these still provide potent hydrogen trapping sites since their hardness is higher than other areas. Therefore, it is expected that a low volume of impurities in the weld metals will reduce SSC susceptibility as in the case of base metals.

On the other hand, in the case of multi-pass welding, MA constituents will appear at the reheated zone of the previous weld pass, similar to the HAZ in base metals, and so it is preferred that the carbon content of the weld should be as low as possible to reduce MA constituents. However, weld metals require high strength to satisfy strength overmatching (meaning they have a higher strength than the base material), and this contradicts the motivation to reduce alloying content. Hence, optimizing carbon content in the welds is an ongoing issue which requires careful selection of welding consumables, and welding parameters for a given base metal and welding process.

1.5.2 Influence of grain size

In terms of the influence of grain size on SSC susceptibility, it is interesting to note that completely opposite and conflicting opinions have been reported. First of all, as a negative connotation, Timmins claims in the ASM handbook that "… grain boundaries are hydrogen traps, decreasing the grain size is tantamount to increasing the grain boundary surface (i.e., the density of hydrogen traps)" [38]. The conclusion is that the grain boundary areas provide trap sites which make the material more prone to initiate SSC.

On the other hand, some researchers have stated that a fine and homogeneous grain structure can improve resistance to SSC. For example, Al-Mansour et al. claim that a fine and homogeneous microstructure can disperse hydrogen trapping sites, and this prevents hydrogen from reaching the critical concentration for SSC/HIC initiation in local areas of the microstructure [39]. Moreover, a relationship has been drawn between austenite grain size and SSC critical strength (σ_c^{85}), which is a value to evaluate SSC initiation in which the material is stressed in bending to 85% of the yield stress, as was mentioned by Asahi and Ueno [40]. This is shown in **Figure 1-3**, which illustrates the critical stress for SSC increases with decreasing grain size. This is further justified by the fact that the size, distribution, and amount of precipitates, which are also significant factors to controlling SSC, do not depend on grain size, while the grain boundary strength contribution increases with decreasing grain size [40]. When both effects are combined, the finer grain size leads to the improvement of SSC resistance. Furthermore, Takasawa et al. conducted notch tensile testing with in-situ hydrogen charging in an autoclave, with thermal desorption analysis for the hydrogen measurement by employing specimens with various grain sizes [41]. It is observed that hydrogen content in the unit boundary area decreases with a decrease in the grain size as illustrated inFigure **1-4** [41]. The relationship between hydrogen mass in the unit boundary area and the fracture surface ratio of intergranular with quasi-cleavage (IQC) region is illustrated in **Figure 1-5**. This reveals that the

fracture surface ratio increases with an increase of hydrogen mass in the unit boundary area. By combining the results in both figures, it appears that finer grain sizes will prevent crack initiation arising from hydrogen embrittlement [41].
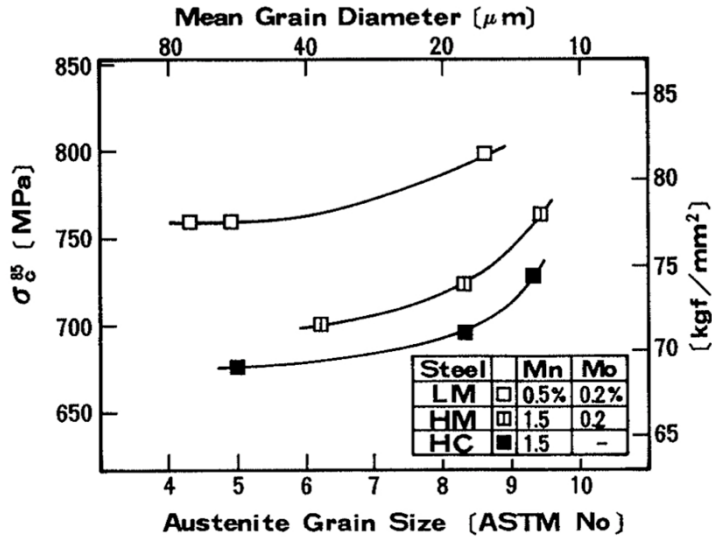
Figure 1-3 Effect of prior austenite grain size number (per ASTM, or mean grain diameter) and critical 85% yield stress for SSC cracking [40]
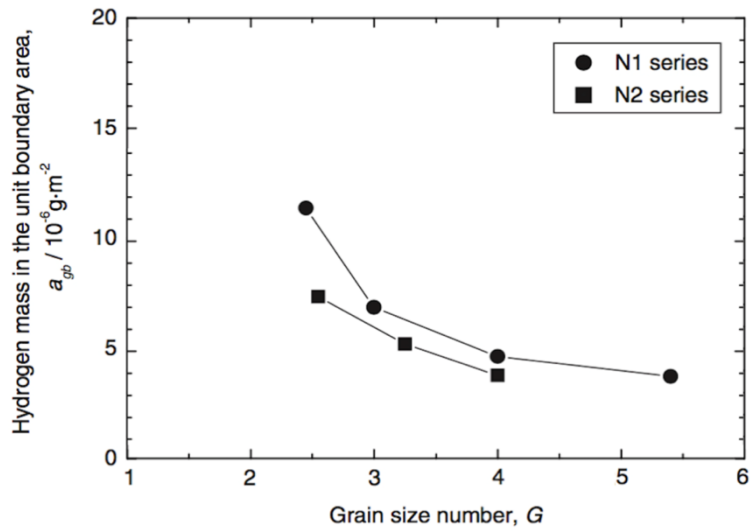
Figure 1-4 Dependence of grain size number on stored hydrogen mass in the unit grain boundary area [41]
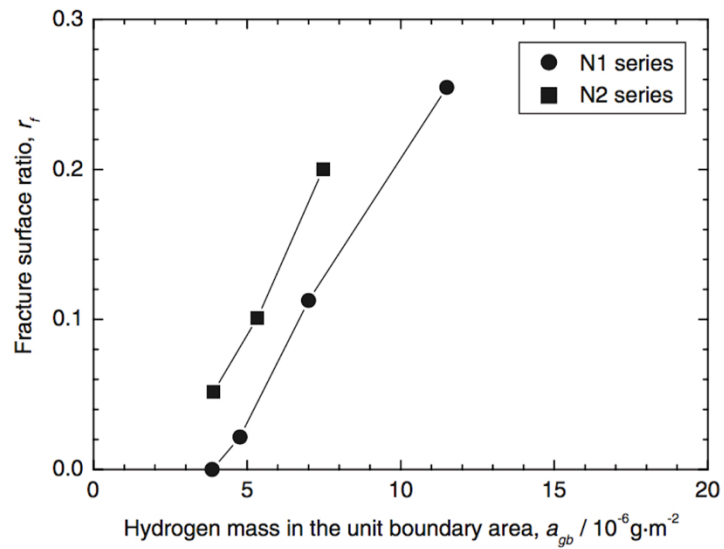
Figure 1-5 Relationship between stored hydrogen mass in the unit boundary area and the fracture

surface ratio of intergranular with quasi-cleavage region [41]

Moreover, some researchers have claimed intermediate opinions. Hydrogen diffusivity and solubility for aluminum alloys which have grain sizes ranging from a single crystal material to sub-micro scale were investigated by Ichimura et al. [42]. A relationship between grain size and diffusion coefficient (which can be used to evaluate hydrogen diffusivity), is shown with the dashed line in **Figure 1-6**. It is noted that the diffusion coefficient has a peak, which indicates that the hydrogen diffusion coefficient is a maximum value between 10 to 30 μm. According to Ichimura et al., this results from two competing grain boundary effects [42]. One involves hydrogen atoms which can diffuse through the grain boundaries, and the other is that diffusible hydrogen atoms can be trapped at the junction-points of grain boundaries [42]. This means that in the case of coarser grains, the path for diffusible hydrogen atoms to move will be reduced, so that coarser grains lead to decreased hydrogen diffusivity. On the other hand, finer grains provide more junction-points which prevent diffusible hydrogen atoms from moving. Also, there will be an increased possibility that diffusible hydrogen atoms are trapped at inclusions and dislocations that typically lie on grain boundaries, and so finer grains will reduce the hydrogen diffusivity. In addition, Yazdipur et al. investigated the relationship between grain size and hydrogen diffusion coefficient for steels by calculating with Cellular Automaton (CA) model, which can simulate diffusion processes [43], where **Figure 1-6** indicates their result as a solid line. It seems that their calculated result correlated well with the line drawn by Ichimura et al. [42]. From this result, it can be noted that hydrogen diffusivity also has a peak when the grain size is in the 10 to 30 μm range and hydrogen diffusivity can be drastically reduced when grain size is less than this range.

Figure 1-6 Comparison of relationships between grain size and diffusion coefficient of aluminum

alloys measured by an experiment and steels calculated by CA model [42-43]

Based an assessment of a wide range of findings, it is clear that the effects of grain size on

hydrogen diffusivity would be controversial considering the complex interaction of multiple

mechanisms. However, grain size is definitely one of the key factors which need to be considered in

the case of actual pipeline welding. Typically, pipeline girth welds require, not only SSC resistance,

but also strength overmatching and high fracture toughness. It is known that both of these other

mechanical properties are improved when grain size is fine and homogeneous; therefore, producing

fine and homogeneous grain size could be a general target. The grain size of prior austenite in weld

metals produced with gas metal arc welding (GMAW) is at least dozens of micrometers; however,

much smaller grain sizes are usually obtained by introducing an acicular ferrite microstructure.

Fairchild et al. state that the average lath width of acicular ferrite in weld metals produced by a

mechanized GMAW system with a heat input of approximately 0.9 kJ/mm and a narrow U shape

groove, typically range from 0.3 to 0.6 μm [44]. Also, a relationship between acicular ferrite lath width

21

and welding heat input was investigated by Motohashi et al. as shown in **Figure 1-7** [45]. This figure

illustrates the relationship between ferrite grain size and heat input for two GMAW consumables and

submerged arc welding (SAW), where GMAW results are illustrated as square and circle markers,

and SAW results are triangular points. The GMAW fusion zones were also produced by mechanized

equipment, with a narrow V shaped groove. As shown in this figure, the acicular ferrite lath width

(which can be considered equivalent to grain size) is approximately 1.0 to 1.5 μm for the range of

heat input applied during GMAW. Although the influence of microstructure will be stated in next

section in detail, promoting an acicular ferrite microstructure can be effective in obtaining a fine and

homogeneous grain size.
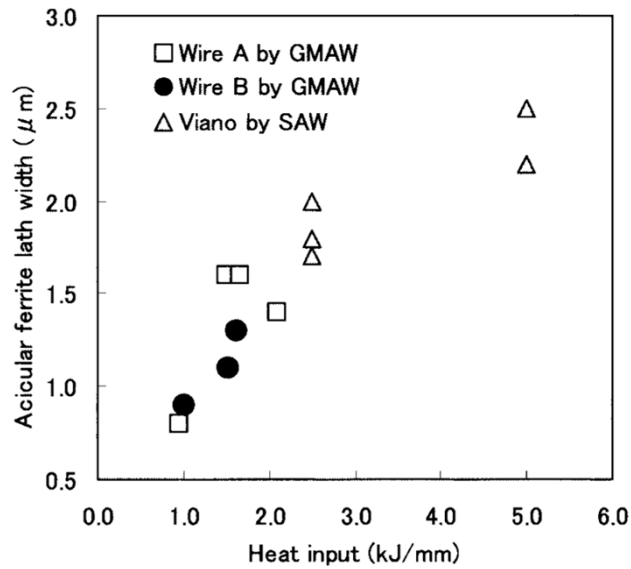
Figure 1-7 Relationship between acicular ferrite lath width and heat input [45]

1.5.3 Effects of Microconstituents

The effect of microstructure on SSC susceptibility, particularly the fraction and types of different steels microconstituents has been investigated by several researchers. Hydrogen diffusivity, permeability, and solubility for various steel microstructures were measured by Park et al. [46], and the measurement data are shown in **Table 1-1**. It was noted that the ferrite/acicular ferrite structure offers the lowest hydrogen diffusivity, lowest permeability, and second highest solubility compared with other microstructures. This implies that acicular ferrite structure is capable of trapping and slowing a significant amount of hydrogen in this microstructure. Also, Koh et al. investigated that HIC susceptibility for two types of steels in accordance with NACE standard TM0177, applying NACE A solution containing 5%NaCl and 0.5% CH_3COOH saturated with H_2S, where a steel dominated by ferrite/acicular ferrite structures and was compared to another composed of ferrite/bainite structures [47]. The relationship between diffusible hydrogen content and HIC susceptibility is shown in **Figure 1-8**, which indicates that ferrite/acicular ferrite microstructures offer excellent HIC resistance compared to ferrite/bainite microstructures.

Table 1-1 Hydrogen permeation data [46]

Specimen	Microstructure	Fraction of DP/AF/B	Apparent diffusivity ($\times 10^{-10} m^2 s^{-1}$)	Permeability ($\times 10^{-9}$ mol $Hm^{-1} s^{-1}$)	Apparent solubility ($\times$ mol Hm^{-3})
A1	Ferrite/ Degenerated Pearlite	3.75	9.27	13.3	14.33
A2	Ferrite/ Acicular Ferrite	8.12	4.05	8.47	20.91
A3	Ferrite/ Degenerated Pearlite	3.93	9.38	12.9	13.79
A4	Ferrite/Bainite	9.38	4.44	12.0	27.13
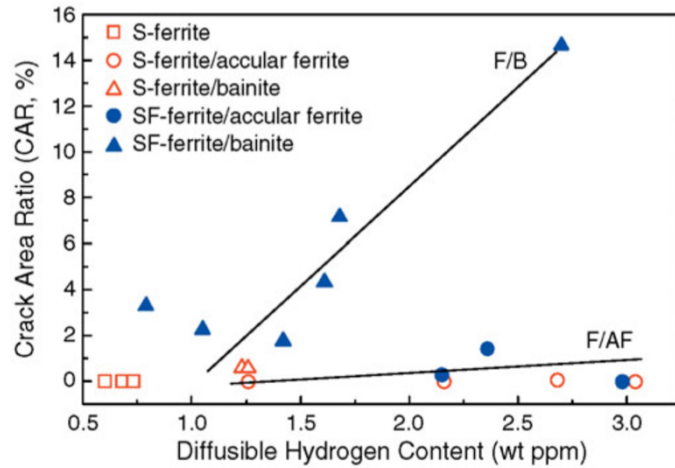
Figure 1-8 Relationship between diffusible hydrogen content and HIC susceptibility [47]

Furthermore, Zhao et al. also claims that an acicular ferrite dominating microstructure exhibits higher SSC resistance than ultrafine ferrite and ferrite/pearlite microstructure, based on SSC testing, which was performed in accordance with NACE TM017-96 Method A and B employing 0.5% mass fraction of CH_3COOH saturated with H_2S as test solution [48-51]. They attributed this to moving dislocations that can trap hydrogen atoms into the acicular ferrite, and these are interrupted by the pinning effect of nano-carbides such as titanium carbides, a phenomenon shown in **Figure 1-9**.
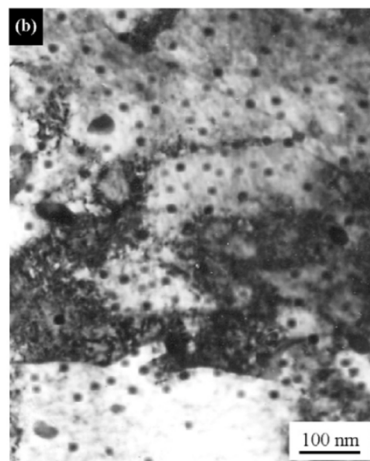
Figure 1-9 TEM micrograph showing a large number of nano-scale carbides distributed in acicular

ferrite [48]

24

If an acicular ferrite microstructure offers excellent SSC resistance, it will be expected that modern weld metals should perform well in sour service applications. Presently, several welding wires are available to promote acicular ferrite in weld metals compared to base metals. In general, promoting acicular ferrite weld microstructures is not difficult, although acicular ferrite nucleation mechanisms have still not been completely clarified, aside from a confirmation that titanium oxides act as acicular ferrite nucleation sites [52]. There are few research papers discussing the SSC susceptibility of GMA weld metals; however, some research indicates how submerged arc weld metals perform. For instance, SSC susceptibility of submerged arc weld metals produced for API 5L X70 pipes had been investigated by Beidokhti et al. [53]. They conducted SSC tests in accordance with NACE standard TM0177-96 Method B using a consisting of 0.5% glacial acetic acid dissolved in distilled water saturated with H_2S as the test solution. In their work, ten weld metals produced by employing different amounts of Fe-Ti powder as a flux was used in order to control acicular ferrite volume fraction while applying two types of welding wires with differing manganese content. The hardness values and the SSC test results for each specimen are shown in **Table 1-2**. It was found that specimens with a hardness value less than 250 HV, satisfy the NACE hardness criterion, passed in SSC test regardless of manganese content. It is also noted that L30, which contained low manganese was composed of approximately 60% acicular ferrite fraction, despite that it exhibited a hardness exceeding 250 HV, also passed the SSC test.

Table 1-2 Acicular ferrite volume fraction, hardness and SSC test results by Beidokhti et al. [53]

Specimen No.	Specimen series	Acicular ferrite volume fraction (%)	Maximum hardness (Hv)	SSC test results	
				80%YS as applied stress	110%YS as applied stress
L00		61.0	202	Pass	Pass
L10	Low	72.3	211	Pass	Pass
L20	manganese	74.2	225	Pass	Pass
L30	series	62.1	260	Pass	Pass
L40		54.9	275	Fail	Fail
H00		72.1	218	Pass	Fail
H10	High	75.6	232	Pass	Pass
H20	manganese	73.7	240	Pass	Fail
H30	series	46.0	292	Fail	Fail
H40		31.6	323	Fail	Fail

Moreover, the SSC susceptibility of heat-affected zones in weld metals produced by GMA-welding on submerged arc weld metals, contained a microstructure dominated by acicular ferrite, and were also evaluated for SSC by Kasuya et al. [54]. They were investigated SSC susceptibility with four point bending method in NACE TM0177 test solution, containing 5%NaCl, 0.5% CH_3COOH saturated with H_2S at 1atm pressure. This test derived the relationship between the carbon equivalent (CE) for varied compositions of weld metals and critical hardness value for carbon equivalent and critical hardness for SSC initiation, which is are summarized in **Figure 1-10**. This figure illustrates that, when the CE is more than 0.32%, the hardness criterion for SSC initiation is approximately 250 HV, which is equivalent to the NACE MR0175 standard, while SSC does not initiate even if the maximum hardness value exceeds 250 Vickers if the CE is less than 0.32%. Furthermore, Wang et al. investigated that the hydrogen trapping mechanism via the hydrogen microprint technique, which is a method to reveal the trapping sites for diffusible hydrogen in at the microscopic scale by utilizing a reaction of silver bromide and hydrogen [55]. The distribution of hydrogen atoms in the acicular ferrite structures resulting from hydrogen microprint technique is shown in **Figure 1-11**. As illustrated in this picture, it seems that hydrogen atoms are accumulating at grain boundaries of randomly oriented

acicular structures. The feature of hydrogen trapping is similar to the grain size effect as mentioned in the previous section.
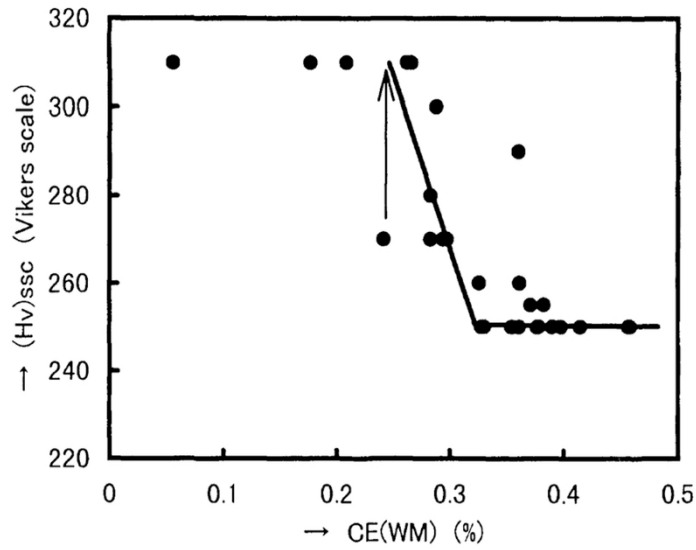
Figure 1-10 Relationship between carbon equivalent modified for weld metals and hardness criterion for SSC initiation [54]
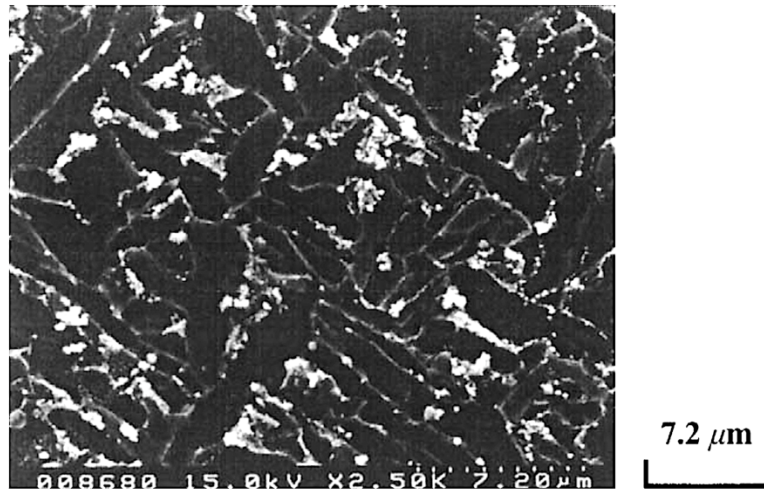
Figure 1-11 Distribution of hydrogen atoms introduced by electrical charging into the acicular ferrite microstructure and revealed via the hydrogen microprint technique [55]

From the published results, it is clear that diffusible hydrogen can be trapped at grain boundaries in acicular ferrite microstructures in the case of submerged arc weld metals; thus it appears that acicular ferrite microstructures in the weld metals can be effective to improve SSC susceptibility in a similar way that has improved base metal performance, although the mechanism for improvement may be a little different. In addition, the results also mention that the critical hardness value for SSC initiation would be more than 250 HV in some cases. GMA weld metals produced with auto/mechanized GMA welding systems, commonly applied for girth welds of actual pipelines can be expected to have more low SSC susceptibility than submerged arc weld metals because of smaller grain size due to low heat input extremely; however, the SSC susceptibility of GMA weld metals should be evaluated more comprehensively. Furthermore, it is expected that the influence of an acicular ferrite volume fraction for SSC susceptibility in GMA weld metals should be investigated in the hardness range above 250 HV. Although acicular ferrite might provide improved SSC resistance as discussed earlier, the present work will consider the role of microstructure in terms of SSC susceptibility and compare this to microstructures with varying fractions of acicular ferrite. Additionally, in this work, the influence acicular ferrite volume fraction to other mechanical properties such as tensile behavior after hydrogen charging will be evaluated more closely.

1.5.4 Summary of re the literature review

Based on the literature review, the following general observations regarding SSC performance can be summarized:

- Reducing impurities such as sulphur and carbon should be an effective method to improve SSC resistance for not only base metals but also weld metals.

- The correlation between grain size and SSC susceptibility remains controversial; however, recent research mentions that finer grain sizes improve SSC performance. Moreover, in order to satisfy all requirements such as strength overmatching, low hardness, high fracture toughness, fine grain structures may offer the best combination of these properties.

Acicular ferrite microstructures can be increased SSC resistance. Recent research papers mention that weld metals which have high acicular ferrite volume fraction were able to pass the SSC test conducted in accordance with NACE standard, even if the hardness value was more than the 250 HV criterion. Hence, more research will be needed to confirm this point.

1.6 Objectives and research plan

The main objectives of this research are shown in below.

[1] Establishing a control method of acicular ferrite volume fraction in the weld metals

[2] Evaluating relationship between kinds of microstructures and SSC susceptibility for GMA weld metals and validate a critical hardness value

[3] Investigating the role of microstructures and establish a minimum acicular ferrite value to prevent SSC initiation

To conduct the first objective, a technique will be needed to control acicular ferrite volume fraction in GMA weld metals. Thus, first of all, this research will establish a method to control acicular ferrite volume fraction in GMA welds by controlling titanium and oxygen content in weld metals, which is described in Chapter 2.

Then, in accordance with NACE NR0175/ISO 15156-2 standard and European Federation of Corrosion Publications Number 16, SSC tests will be conducted employing some welded joints which have various acicular ferrite volume fraction. Moreover, this research will investigate hydrogen trapping mechanism with hydrogen microprint technique which is a method to observe hydrogen trapping site [56] by utilizing a reaction between silver bromides and hydrogen. Furthermore, density for dislocations which can carry diffusible hydrogen to harder area will be compared with TEM. The investigated results will be described at Chapter 3.

Furthermore, the influence of microstructures in GMA weld metals on some mechanical properties such as tensile behavior and hardness after hydrogen charging, will be investigated. Moreover, hydrogen trapping ability will be compared between high and low intragranular ferrite volume fraction with thermal desorption analysis. Those investigated results will be mentioned in Chapter 4. Finally, the conclusions of this research will be summarized in Chapter 5.

Chapter 2
Maximization of acicular ferrite volume fraction in pipeline GMA welds - Effects of titanium and oxygen contents on acicular ferrite volume fraction-

2.1 Introduction

As mentioned in Chapter 1, microstructures with high fractions of acicular ferrite volume may promote SSC resistance since this microstructure exhibits properties which include low hydrogen diffusivity, low permeability, and high solubility. Although pipeline girth welds require satisfying multiple mechanical properties simultaneously, including those potentially at odds with each other, the acicular ferrite microstructure is expected be effective in achieving those requirements since it can provide not only high strength, but also high toughness resulting from fine, homogeneous, and interlocking ferrite grain structures. Moreover, it offers low hardness compared with other microstructures such as martensite, pearlite, and bainite (both upper and lower bainite types). Therefore, the formation of acicular ferrite has been a general strategy to satisfy all mechanical requirements for weld metals of pipelines up to the API 5L X100 grade. The acicular ferrite microstructure is considered a type of intragranualar ferrite (IGF) since the acicular needles form within the prior austenite grains typically at non-metallic nucleation points, whereas intergranular forms of ferrite such as grain boundary ferrite, grows from the prior austenite grain boundaries, as schematically shown in **Figure 1-1** in Chapter 1.

Nowadays, many wire and stick welding consumables are available for high strength steels, which promote mainly IGF microstructures with excellent mechanical properties. Although the IGF nucleation mechanisms still remain controversial, it is widely accepted that titanium oxides strongly act as IGF nucleation sites [52, 57-72]. Many researchers have investigated the effects of both titanium and oxygen content in the weld metals respectively; however, most papers have examined weld metals containing less than 0.3 wt.% of titanium [57-67, 71, 72]. On the other hand, some researchers have investigated the effects of chemical content on IGF volume fraction in the case of titanium content

exceeding 0.5 wt.% [68-70]. One method suggested to investigate the effect of titanium, involves adding a very thin pure titanium wire to the molten pool directly [68-70]. Those authors have indicated that the volume fraction of IGF in the weld metals can be controlled with this method; however, they did not mention the combined effects of both titanium and oxygen. It is considered that titanium oxide plays the key role, and dissolved titanium atoms in solution do not cause acicular ferrite nucleation; hence, the combined effects of these elements should be considered in order to maximize IGF volume fraction in weld metals.

In this chapter, weld metals with varying IGF volume fraction and hardness are produced by in-situ alloying thin pure titanium wires during welding and applying various premixed shielding gases with different Ar/CO_2 ratios. Then IGF volume fraction, chemical composition, and hardness are investigated for each weld metal, respectively. Moreover, a focus is made on whether a suitable balance of titanium and oxygen content in the weld metal can maximize the volume fraction of IGF. Furthermore, a hardness evaluation method will be investigated in terms of how well this correlates to the carbon equivalent formula for weld metals.

2.2 Materials and experimental methods

The specimen list for this work is shown in **Table 2-1**. All weld joints were produced using a robotic GMA welding machine. The base material was 1/8 circumference segments of API 5L X80 linepipe material with a thickness of 15.1 mm, 24 inches diameter, and two different welding wires were employed. Those chemical compositions of the pipe and welding wires are shown in

Table 2-2 and **Table 2-3**, while a commercially pure titanium (CP-Ti) wire with a composition shown in **Table 2-4** was employed for alloying in-situ to the weld metals. A U-shape weld groove was used to produce the weld metal specimens, which consisted of J-bevel design on each side, using an angle of 3º, a 1.8mm root face, and groove width of approximately 6.4mm at the outer surface of pipes, which is illustrated in **Figure 2-1**.

Table 2-1 Specimen list (summarizing in put wires and shielding gases used)

Specimen ID	Welding wire	Titanium wire	Shielding gas
AA-15	Wire A	Added	85%Ar-15%CO_2
AA-30	Wire A	Added	70%Ar-30%CO_2
AA-50	Wire A	Added	50%Ar-50%CO_2
B-15	Wire B		85%Ar-15%CO_2
B-30	Wire B		70%Ar-30%CO_2
B-50	Wire B		50%Ar-50%CO_2
A-30	Wire A		70%Ar-30%CO_2

Table 2-2 Chemical composition for the pipe (mill certificate, wt.%)

C	Si	Mn	Cr	Ni	V	Cu
0.048	0.18	1.76	0.03	0.13	<0.01	0.12

Al	Mo	Ti	Nb	N	O	
0.03	0.22	0.01	0.04	0.0038	0.0013	

Table 2-3 Chemical compositions for the welding wires (mill certificate, wt.%)

	Dia. (mm)	C	Si	Mn	P	S	Mo	Ti
Wire A	1.2	0.09	0.70	1.96	0.004	0.004	0.63	-
Wire B	1.2	0.07	0.68	1.96	0.011	0.004	0.69	0.06

Table 2-4 Chemical compositions for the pure titanium wire (mill certificate, wt.%)

	Dia.(mm)	C	Ti	Fe	H	O
CP-Ti wire	0.2	<0.01	Bal.	0.03	0.0063	0.04
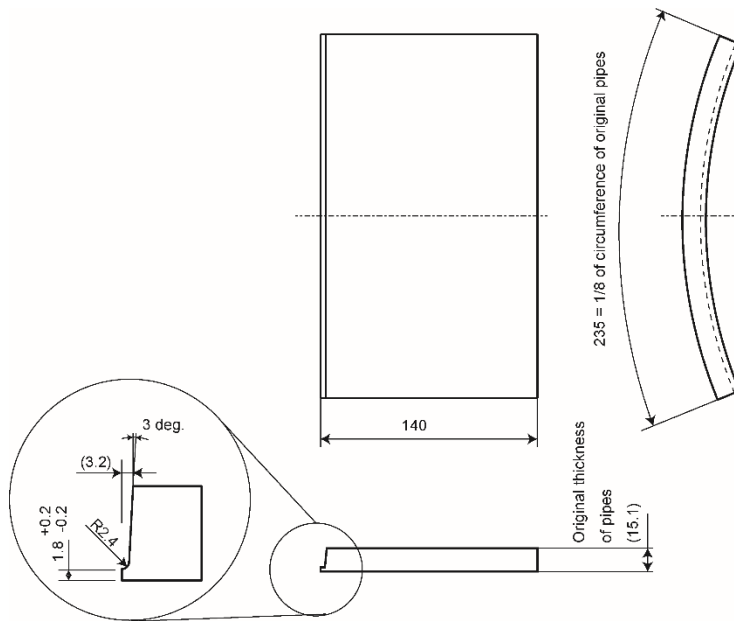
Figure 2-1 Drawing of weld bevel used in the present study

The welding parameters when applying 70%Ar-30%CO_2 shielding gas are shown in **Table 2-5**. These welding parameters were determined based on a welding procedure applied in actual pipeline girth welds [32]. The welding was performed with six passes with one layer of weld metal per pass. The arc length during welding depends on the shielding gas since the electrical potential gradient is affected by the gas properties. In this study, in order to maintain a constant arc length, (and prevent changes in weldability and defects), the input voltage was slightly changed to compensate for the change in arc length with different gases. For example, the voltage was decreased 1.5V when 85%Ar-15%CO_2 gas was employed compared with 70%Ar-30%CO_2 gas to avoid a longer arc length with decreasing CO_2 ratio in shielding gas due to higher electrical potential gradient. On the other hand, in the case where 50%Ar-50%CO_2 gas was used, the voltage was increased by 1.5V for each pass to compensate for the inherent electrical potential change with the higher CO_2 content. All weld specimens were produced in a butt weld configuration in the flat position. As shown in **Figure 2-2**, two 1/8 circumferential sections of the pipe base material cut from 24" (610 mm) diameter pipe sections. The first series of welds labelled AA-series were produced with the addition of a 0.2 mm titanium wire for alloying in-situ during welding. A thin titanium wire was tack-welded by resistance spot welding onto the bevel every few centimeters for the root pass and the bead surface for hot and filler pass in order to avoid the wire being blown away by the arc plasma and gas flow.

Table 2-5 Welding parameters in when using 70%Ar-30%CO_2 shielding gas

Welding pass	Target Current (A)	Wire Feeding Speed (m/min)	Voltage (V)	Travel Speed (cm/min)	Expected Heat Input (kJ/cm)
Root	300	9.5	26.0	120	3.9
Hot	280	8.5	26.0	60	6.3
Filler 1	280	8.5	26.0	60	6.3
Filler 2	280	8.5	26.0	60	6.3
Filler 3	280	8.5	26.0	60	6.3
Cap	220	6.0	23.0	30	10.1
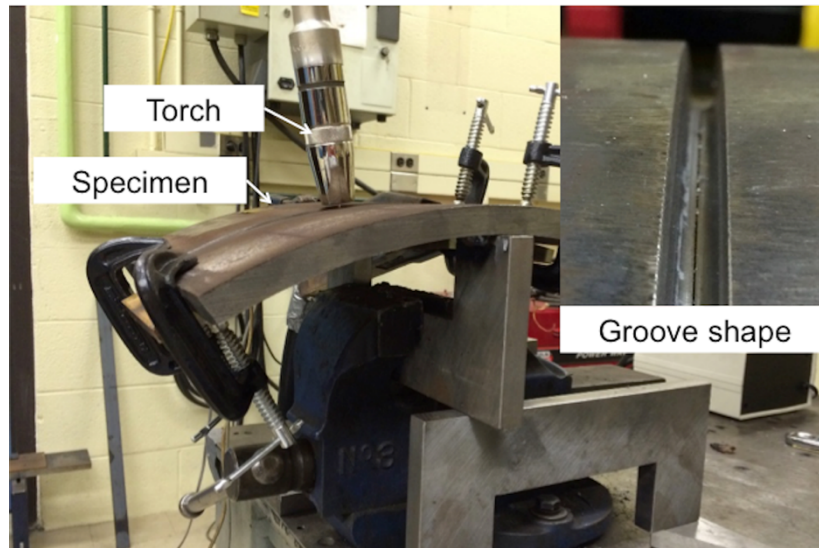
Figure 2-2 Layout of fixtures for robotic welding of pipe segment

After welding, microstructures of all weld metals were observed at 200X and 500X magnifications with an Olympus BX51M optical microscope after polishing and etching with 5% Nital solution for few seconds. Microstructure examination observation was performed at the bead center of the as-deposited weld metal in the hot pass. Volume fractions of IGF were measured with the point counting method, in which a lattice was drawn with a 10 micrometer spacing at a 200X

magnification, and the number of line intersections containing IGF were counted over a total of 896 points per micrograph, with the volume fraction values determined by averaging measurements for five micrographs in order to avoid bias. Moreover, chemical analysis of the weld metals was conducted to investigate the actual chemical compositions of each weld metal. Furthermore, titanium oxide precipitates were observed with transmission electron microscopy (TEM), where FEI Titan 80-300LB was used as TEM equipment and operated at 300 kV.

The sample for TEM observation was extracted carefully from the root area in the weld metals by punching, and milling using focused ion beam (FIB), where a Zeiss NVision 40 was used as FIB equipment. A layer of tungsten was deposited initially to prevent excavating the material on the plane of the sample. Then, low energy milling was conducted in steps at 10kV and 5V to remove amorphous material which was produced during prior steps of milling and deposition of tungsten on the surface. Such prepared sample was employed for TEM observation. Furthermore, the distribution for chemicals around/on the precipitates was investigated by energy dispersive x-ray spectroscopy (EDX) during TEM observation. Also the Vickers hardness in the weld metals was measured for each specimen, where the hardness tests were performed with a 9.8N load and a 0.5 mm pitch along the through-thickness direction at the bead center of a cross-section and also along the transverse direction on a 2 mm line from inner surface of pipes. It is noted that this location 2 mm within the inner wall diameter is also the location evaluated for sulphide stress cracking, as discussed in the next chapter.

2.3 Experimental results

An optical macro-photograph for weld specimen B-15 is shown in **Figure 2-3** as an example of the weld cross-section. The optical micrographs for weld metals in the AA series and B series are shown in **Figure 2-4**, while the results of the IGF volume fraction measurements in each weld are indicated in **Table 2-6**. The intragranular ferrite is defined as the total of intragranular Widmanstätten ferrite, polygonal ferrite, and bainitic ferrite according to the definitions introduced by Thewlis [7].
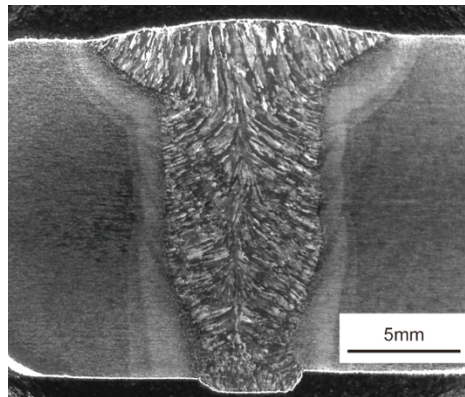
Figure 2-3 Optical macro-photograph for weld specimen (B-15)
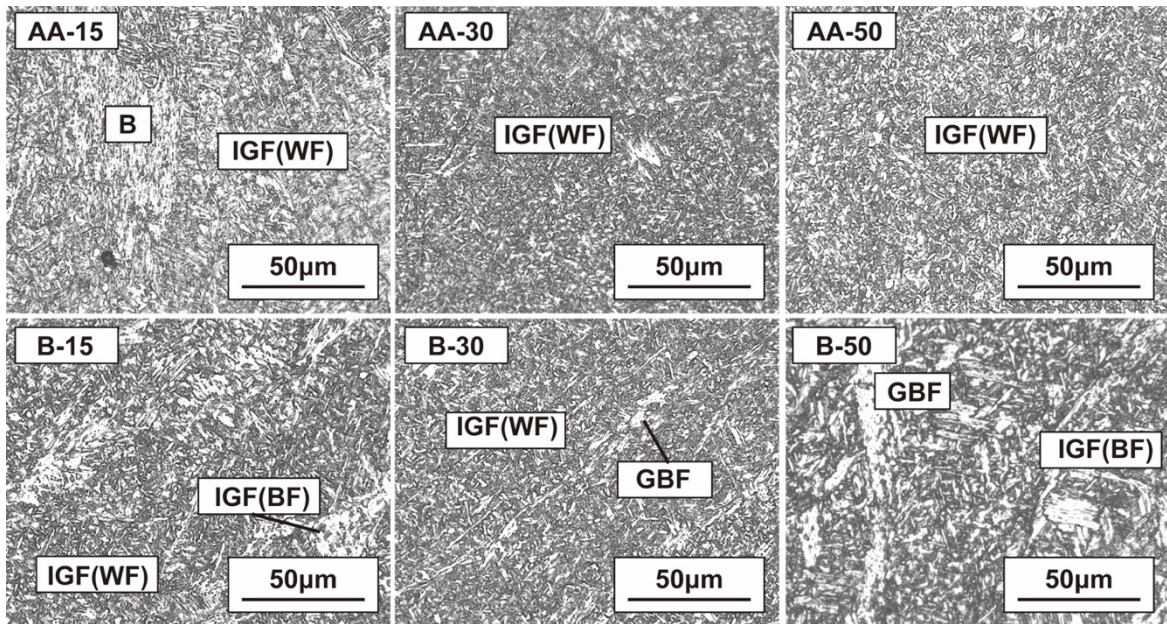
Figure 2-4 Optical micrographs for AA series and B series as-deposited hot pass weld metal

microstructures

Table 2-6 Results of measurements for intragranular ferrite volume fraction

Specimen ID	Volume fraction of intragranular ferrite (%)			
	Average	Maximum	Minimum	Standard deviation
AA-15	71.4	84.4	45.0	14.2
AA-30	96.4	97.0	95.9	0.4
AA-50	96.9	98.8	95.2	1.2
B-15	94.3	97.5	91.2	2.3
B-30	95.2	97.7	93.1	1.5
B-50	80.9	87.4	71.0	5.6
A-30	87.5	91.6	82.9	3.3

As shown in
Table 2-6 and **Figure 2-4**, IGF is the dominant microconstituent in all cases. It is noted,

however, that in the AA-15 weld metal, which was produced with 85%Ar-15%CO_2 shielding gas has

a much higher fraction of bainitic microstructures with some aligned carbide. In contrast, B series

weld metals also contain more IGF microstructures; however, higher amounts of grain boundary

ferrite appeared in weld metal B-50 which employed 50%Ar-50%CO_2 shielding gas. The results for

chemical analysis for each weld metal are shown in **Table 2-7**. Those chemical composition were measured in accordance with ASTM E1019-11, E1097-12(modified) and E1479-99, respectively. The relationship between CO_2 ratio in the shielding gas and the content of titanium in the weld metals is compared in **Figure 2-5**, and the relationship between CO_2 ratio in the shielding gas and the oxygen content in the weld metals is compared in **Figure 2-6**. It can be noted that increasing CO_2 concentration in shielding gas leads to the decrease in titanium content in the weld metals, while oxygen content in the weld metals shows the opposite relationship with shielding gas CO_2 content.

Table 2-7 Results of the chemical analysis for the weld metals (wt.%)

Specimen ID	C	Si	Mn	Al	Ti	O	N
AA-15	0.084	0.57	1.79	<0.01	0.06	0.018	0.0032
AA-30	0.082	0.53	1.72	<0.01	0.04	0.026	0.0036
AA-50	0.079	0.47	1.63	<0.01	0.03	0.027	0.0036
B-15	0.056	0.54	1.68	<0.01	0.04	0.022	0.0032
B-30	0.055	0.50	1.66	<0.01	0.03	0.031	0.0039
B-50	0.057	0.45	1.57	<0.01	0.03	0.034	0.0033
A-30	0.082	0.48	1.69	<0.01	0.01	0.029	0.0032
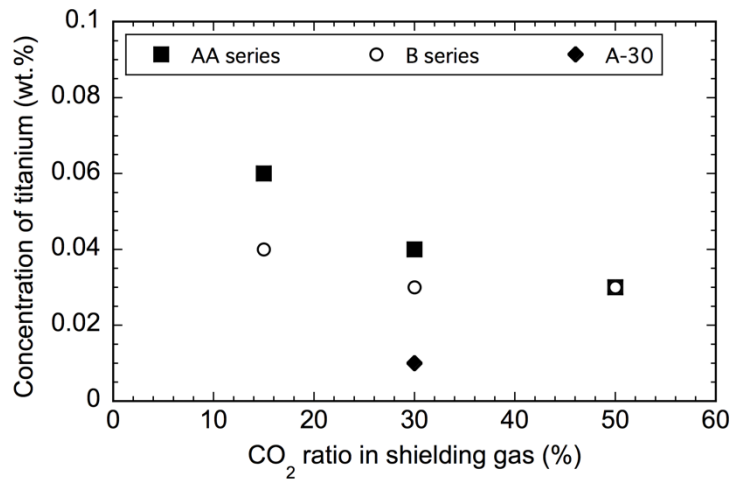
Figure 2-5 Relationship between CO_2 ratio in the shielding gas and titanium concentration

in the weld metals
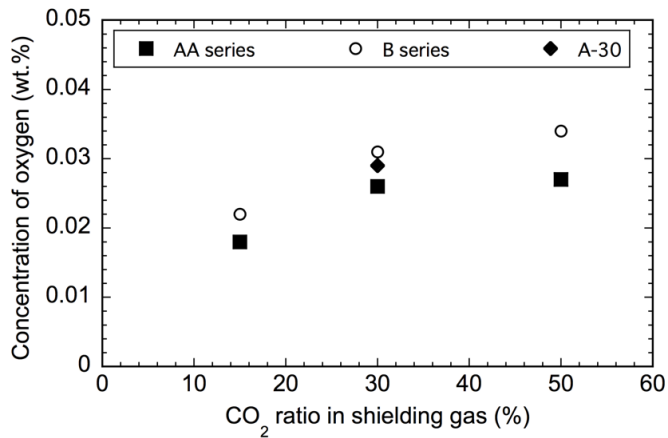
Figure 2-6 Relationship between CO_2 ratio in the shielding gas and oxygen concentration

in the weld metals

A titanium oxide precipitate observed with TEM and the corresponding EDX results around

and through the precipitate are shown in **Figure 2-7**. It seems that the precipitate has a layered

structure, in which a titanium dominant structure is at the center and an outer shell consisting of

manganese sulphide which appears on the edge of the titanium dominant core. Additionally, it is

noted that a manganese depletion zone (MDZ) occurs around the phase, which is suspected to be due

to the manganese sulphide because both elements indicate a peak at same position.
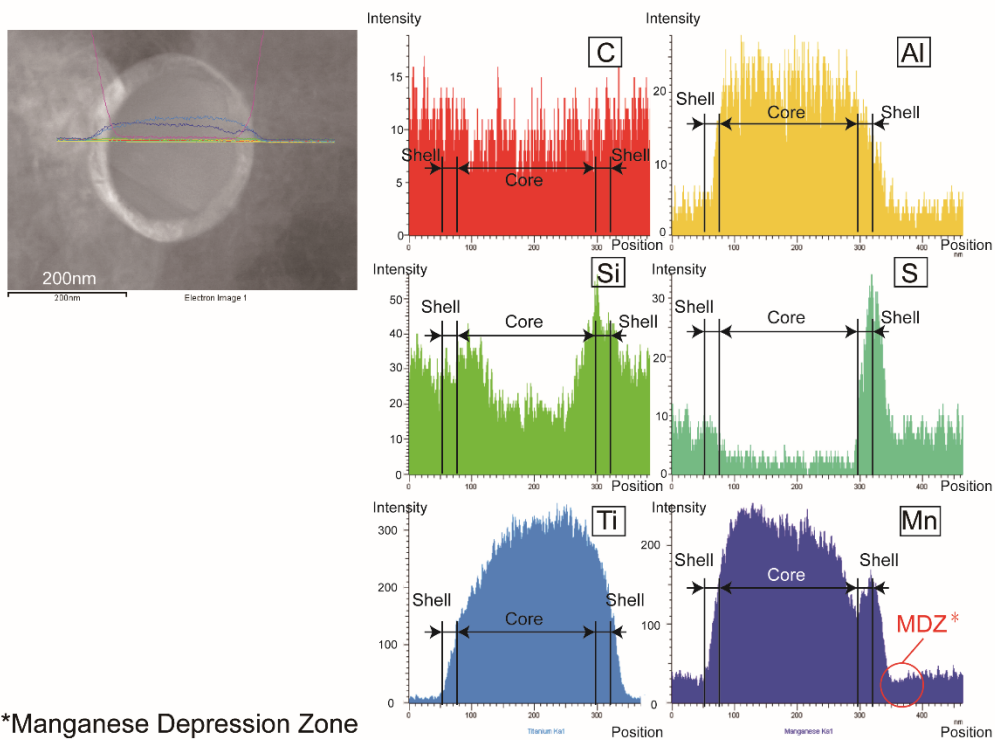
Figure 2-7 A titanium oxide precipitate observed with TEM and the EDX results for around/on the

precipitate

A summary of hardness test results is provided in **Table 2-8**, where hardness test results at

2mm line from the pipe inner surface and a location 2 to 7 mm from the inner surface at the bead

center of a cross-section are shown in the table. The 2 mm line corresponds to tensile side surface,

and the location 2 to 7 mm corresponds to the extracted coupon area for Sulphide Stress Cracking

(SSC) tests described in next chapter. As one of the examples, the hardness distribution along the

through-thickness at the bead center of specimen AA-50 is shown in **Figure 2-8**. Although the

deviation around the average hardness was highest in specimen AA-15 with a value of 16.2 HV,

others exhibited scatter less than 10.0 HV. In addition, the relationship between average IGF volume

fraction and hardness is shown in **Figure 2-9**. The hardness values indicate the average hardness

values in the range of 2 to 7 mm from the weld root surface through the centerline. Comparing to the

hardness results, clear correlation between IGF volume fraction and hardness cannot be detected in

Figure 2-9.

Table 2-8 Summary of the hardness tests

Specimen ID	Hardness values $Hv_{9.8}$ (-) @2-8mm position from inner surface at the bead center of a cross-section				Hardness values $Hv_{9.8}$ (-) @transverse direction on a 2 mm line from inner surface of pipes			
	Average	Maximum	Minimum	Standard deviation	Average	Maximum	Minimum	Standard deviation
AA-15	290.7	329	267	16.2	284.5	308	256	19.7
AA-30	273.1	287	256	8.0	273.6	295	259	11.7
AA-50	259.5	268	249	5.0	256.5	268	249	5.6
B-15	266.0	277	254	6.7	263.6	283	250	9.7
B-30	258.8	263	243	6.2	259.4	267	244	6.3
B-50	240.0	251	233	5.7	237.0	249	226	6.8
A-30	263.2	281	250	9.5	250.5	258	242	5.4
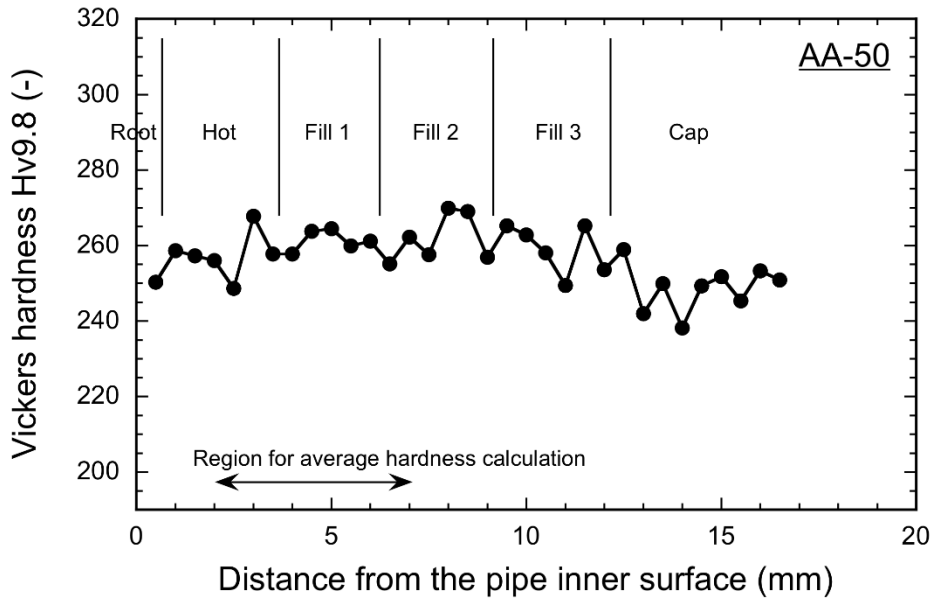
Figure 2-8 Hardness distributions along through-thickness at the bead center of AA-50
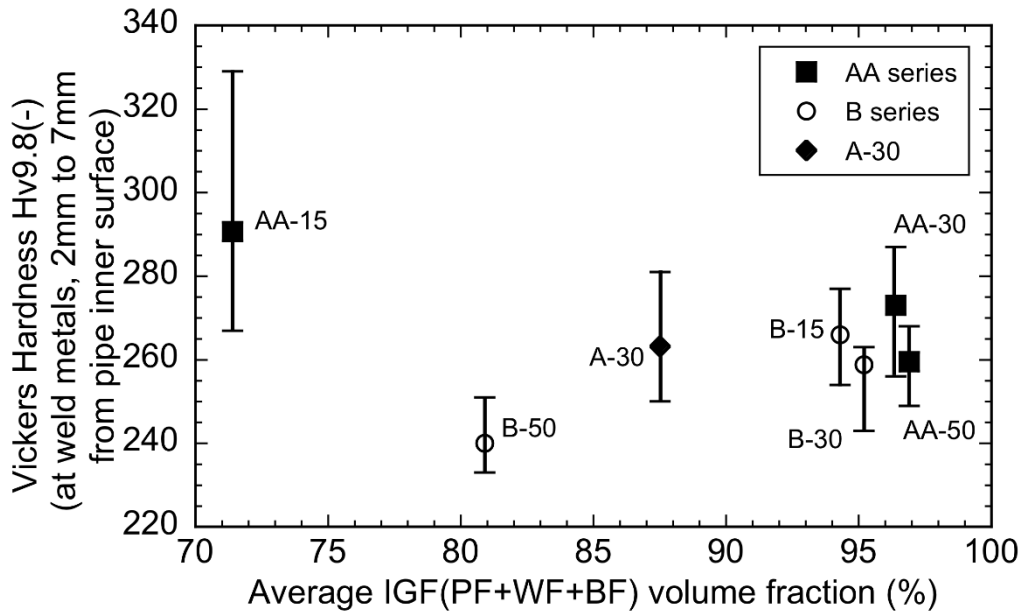
Figure 2-9 Relationship between average of IGF volume fraction and hardness value

2.4 Discussions

First of all, the element recovery rate for titanium (determined by the amount of titanium vaporized and lost by the welding arc) should be considered when further investigating the reaction between titanium added from welding consumables and oxygen in the shielding gas as shown in **Figure 2-10**. This recovery rate was calculated by dividing the titanium content in the weld metal measured using chemical analysis by the initial titanium content in the weld metals contributed by either the 0.2mm diameter titanium wire or within the titanium alloyed consumable wire B. According to the calculation for the initial titanium content in the case of AA series, the volume of titanium wire per unit length is 0.13 wt.%. On the other hand, in the case of B series, titanium content contributed by the welding wire B is 0.06 wt.% as mentioned in **Table 2-3**. As shown in **Figure 2-10**, the recovery rate of titanium has a negative correlation with the CO_2 ratio in the shielding gas.
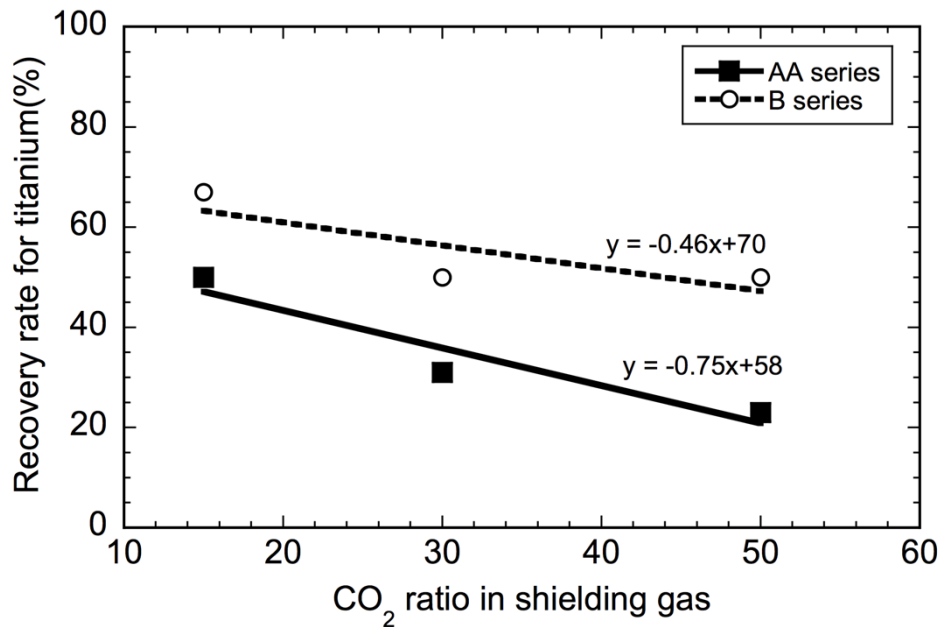
Figure 2-10 Comparison of titanium recovery rate between AA-series and weld B-series

That the recovery rate becomes the negative correlation can be explained by the fact that titanium reacts with oxygen and produces titanium oxides, then, most of those will be discharged as slag, since titanium acts as deoxidizer. Also, it can be seen that titanium recovery rate for AA series is less than B series. This is explained by the difference in titanium surface area exposed at high temperature during welding. For instance, in the case of the AA series specimens the added pure titanium wire placed onto the previous weld bead, will have a high area of pure titanium exposed to the high temperature because the wire is exposed to the arc plasma directly. In contrast, for the B series specimens which include titanium from the welding wire, only the small alloy content of titanium located at the surface area can react at the tip of welding wire. The difference for the efficiency for the reaction between titanium and oxygen results from this difference in titanium surface area exposed to high temperature; thus, it is suggested that this leads to the difference in recovery rate. Additionally, oxygen content in the B series is higher than AA series as illustrated in **Figure 2-6**. This also can be explained by the difference in the reaction area between AA series and B series and supports the cause of the difference for the recovery rate. The relationships between titanium and oxygen contents in the weld metals and volume fraction of IGF are illustrated in Figure 2-11 and, Figure **2-12**, respectively. Both figures exhibit a peak that indicates IGF volume fraction exceeds approximately 90% when titanium content is approximately 0.03 to 0.04 wt.% and oxygen content is 0.025 to 0.028 wt.%. One can expect that some optimal relations between titanium and oxygen will maximize IGF volume fraction. The nucleation mechanism for IGF (acicular ferrite) may help to reveal the ratio for this optimization. The IGF nucleation mechanism, however, remains controversial even although many studies about acicular ferrite nucleation have been conducted since the acicular ferrite microstructure was developed.
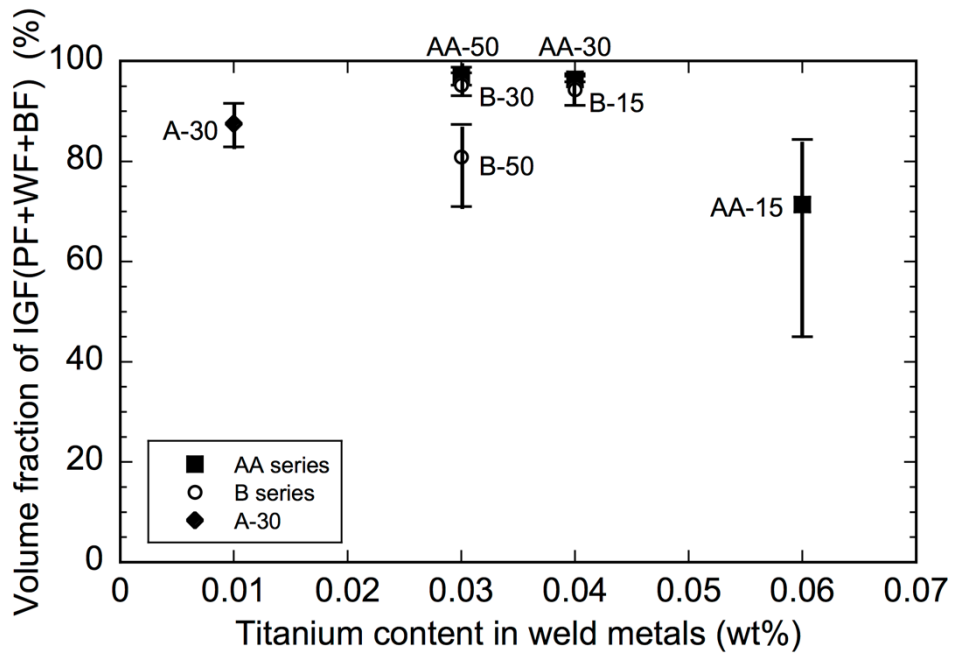
Figure 2-11 Relationship between titanium content in the weld metals and IGF volume fraction
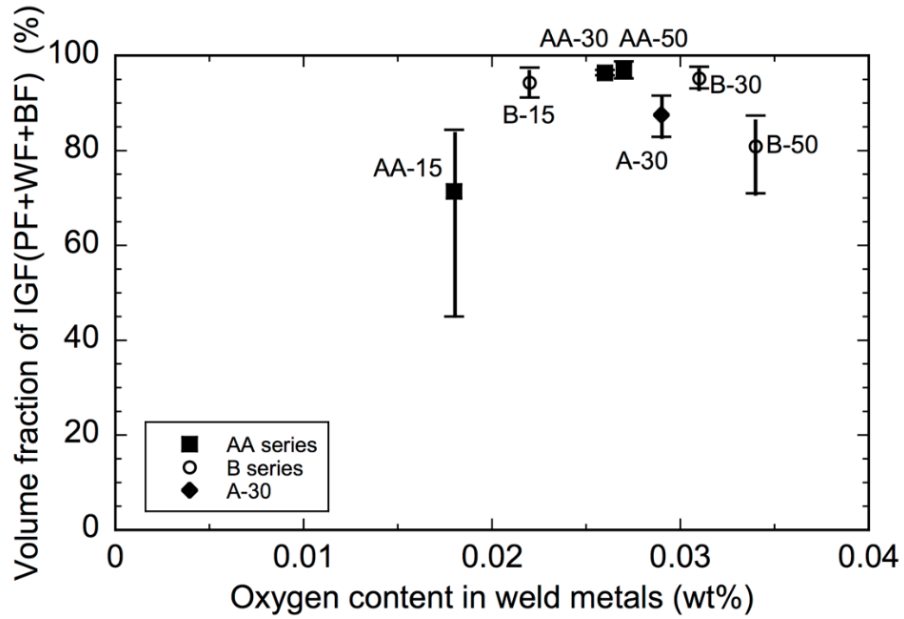
Figure 2-12 Relationship between oxygen content in the weld metals and IGF volume fraction

Before considering the results in this work, two opinions regarding acicular ferrite (IGF) nucleation mechanism that have been discussed are reviewed. First of all, the lattice misfit theory by Yamada et al., states that a TiO layer around inclusions having spinel construction like $MnAl_2O_4$ provides the nucleation sites for IGF resulting from TEM observation they performed [61-64]. A TiO layer is expected to have a good lattice fit with ferrite grains because of low lattice misfit strain compared with other titanium oxide form [61-64] (the lattice misfit value for TiO is 3.0%). On the other hand, Yamamoto et al. claim that MnS and TiN adhere on the surface of Ti_2O_3 particles and these act as the main IGF nucleation sites [71]. In detail, the manganese depletion zone (MDZ), which is generated around MnS phases contributes to IGF nucleation [52, 71, 72]. The presence of the MDZ around the particle increases the Ar3 transformation temperature locally, and this promotes the ferrite nucleation from this local zone. Additionally, the lattice misfit value between TiN and ferrite is 4.6%, which is also low, hence it is possible to be a favourable nucleation site. Although this prior work had focused on weld metals or steels with less than 0.3 wt.% for titanium content, a study of intragranular ferrite nucleation in weld metals with high titanium concentration had been performed by Seo et al. [65-67]. They have not mentioned the presence of TiN particles; however, Ti_2O_3 particles with a MDZ were found in weld metal but their result is similar to the results observed by Yamamoto et al. [68]. According to Gregg and Bhadeshia [73], and Xiong et al.[74]; therefore, it is considered that MnS on Ti_2O_3 acts as a nucleation site for intragranular ferrite. Furthermore, Uto et al. mention that amorphous particles consisting of Si-Mn-Al-O near a Ti-O shell acts to promote the MDZ around particle, supporting the manganese depletion zone theory [75]. In the case of results obtained in this work, in particular the feature in **Figure 2-7**, precipitates including titanium oxide and manganese sulphide (MnS) were found by the TEM observation for AA-30. Although the titanium oxides could not be conclusively identified by TEM, it is high possibility that these are Ti_2O_3 particles because the observations are similar to those compared with the results of Yamamoto et al. and Seo et al. [68-71].

For further investigation, the phase diagram for AA-30 was calculated with MatCalc which is thermodynamic calculation software based on the chemical composition resulting from chemical analysis as the result is shown in **Figure 2-13**. This figure illustrates that the most stable titanium oxide form at the temperature range for intragranular ferrite nucleation, around 1100K to 800K is Ti_2O_3. This can support indirectly that Ti_2O_3 is present as IGF nucleation sites.
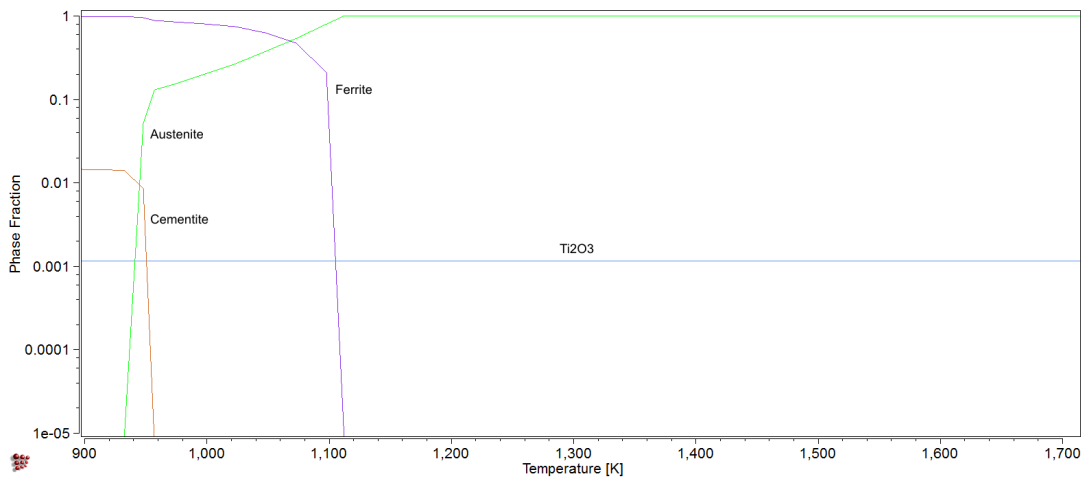
Figure 2-13 Calculated Scheil diagram for weld metal specimen in AA-30

In order to determine the best balance between titanium and oxygen content to maximize IGF volume fraction in the weld metals, the following hypothesis can be proposed; in that the most effective balance of titanium and oxygen contents to maximize IGF is the ideal stoichiometric balance for Ti_2O_3. For instance, if excess oxygen remains after reaction with titanium, the overall silicon and manganese contents will be decreased because oxygen reacts with them next and generates SiO_2 and MnO, which can remain in the weld metal, but some is removed as slag oxide. As shown in **Table 2-7**, the silicon and manganese decreased with increasing CO_2 content in shielding gas. This can be supported by the explanation as follows. The decreasing of silicon and manganese would lead to the decrease intragranular ferrite in the weld metals since it is known that compounds such as $MnOSiO_2$

and Al_2O_3MnO containing spinel structures will be nucleation sites for intergranular ferrite [52]. In addition, Terashima et al. claim that oxygen can result in increased grain boundary ferrite [76]. Hence, as the mentioned above, it is suggested that surplus oxygen will decrease the intragranular ferrite. Support for this can be noted that B-50, which has low titanium and high oxygen content and also shows a higher volume fraction of grain boundary ferrite as shown in **Figure 2-4**.

In contrast, in the case of titanium remaining in surplus, titanium will react with nitrogen after reaction with oxygen, and is then expected to generate TiN. TiN also provides a preferential ferrite nucleation sites because of low lattice misfit; however, it may increase bainitic microstructures such as upper and lower bainite since it is known that TiN distributes at austentite grain boundaries because it acts as grain boundary pinning sites before TiO containing steels were developed [77]. In addition, according to Babu, a coarse prior austenite grain size is required for intragranular ferrite formation [78]. Thus, the formation of TiN resulting from surplus titanium will interrupt intragranular ferrite nucleation due to austenite grain refinement. Support for this notion is observed in a higher volume fraction of bainitic structures found in AA-15 which has a high titanium content and low oxygen content as shown in **Figure 2-4**.

The relationship between the ratio of molar number between titanium and oxygen when their ratio is 2:3 and volume fraction of IGF is shown in **Figure 2-14**. The ratio, $R_{Ti2/O3}$ is calculated with the equation below;

$$R_{Ti_2/O_3} = \frac{Ti/2Ti_m}{O/3O_m}$$

Where;

Ti = Titanium contents in the weld metals (wt.%)

Tim = Atomic weight for Titanium (= 47.867 g/mol)

O = Oxygen contents in the weld metals (wt.%)

Om = Atomic weight for Oxygen (= 15.999 g/mol)

If this ratio is one, it means that neither titanium nor oxygen is in surplus when Ti_2O_3 is generated by reactions during welding. The **Figure 2-14** illustrates that the curve has a peak when the ratio is approximately one, and corresponds with the hypothesis above. Also, for the values <1 on the horizontal axis, oxygen is surplus in the weld metal, which occurs for example in specimen B-50 which contains a large amount of grain boundary ferrite. On the other hand, when the horizontal axis in **Figure 2-14** is >1, one expects a surplus of titanium and high fractions of TiN in the weld metal, which leads to high fractions of bainite structures obtained as expected in specimen AA-15. Also, this figure agrees well with the curve drawn based on data mentioned by Seo et al. [70], who also observed a peak when the ratio is one as in the present study. A slight difference in the slope of the curves is observed. It is suggested that this was caused by differences in silicon and manganese content in the weld metals since the welds in the present work contained up to 0.28% more silicon and 0.51% more manganese. Additionally, there is the difference between acicular ferrite and IGF, in which case their plots only indicate acicular ferrite, but the present study illustrates the IGF plots. This approach for maximizing IGF in the weld metals is cannot be universally applied because it does not consider other chemicals which influence intragranular ferrite nucleation such as aluminum, but it can be a useful engineering guideline.
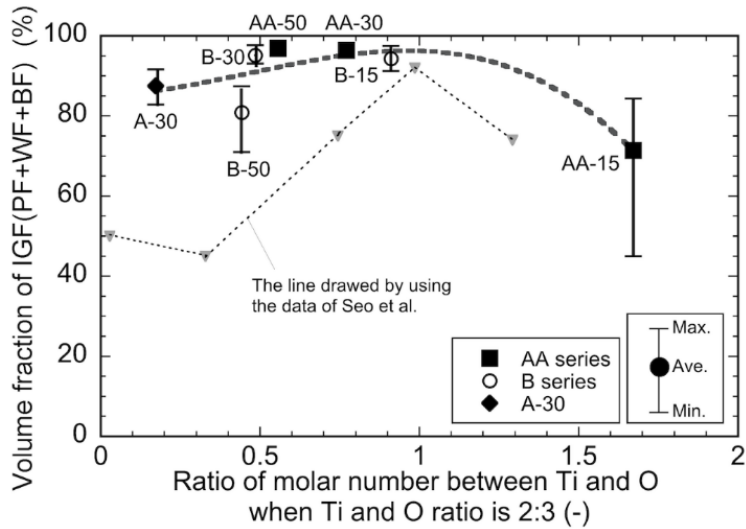
Figure 2-14 IGF volume fraction versus titanium and oxygen ratio when Ti:O ratio is 2:3.

Since hardness is another critical consideration in the present work, it is worth exploring whether the carbon equivalent (Ceq) is useful to estimate hardness of steels. There are many Ceq equations published, and users have to choose by considering the most relevant alloying elements involved. In this research, the CE(WM) value proposed by Yurioka et al. was chosen since the equation includes the effects of titanium and oxygen, and can assess hardness in weld metals [79]. The equations are shown in below:

$$CE(WM) = C + \frac{Si}{24} + \frac{Mn}{8} + \frac{Cu}{15} + \frac{Ni}{12} + \frac{Cr}{8} + \frac{Mo}{4} + \Delta H \ \ldots\ldots\ldots (1)$$

Where

$$\Delta H = -\frac{0.14}{600}(O - 20) + \Delta B_H \ \ldots\ldots\ldots (2)$$

$$\Delta B_H = 0 \ (B < 2)$$

$$= 0.09\frac{B - 2}{B_x - 2} \ (2 \le B \le B_x) \ldots\ldots\ldots (3)$$

$$= 0.09(B_x < B)$$

52

$$B_x = 4 + \frac{45}{300}O^* + \frac{45}{50}N^* \ldots\ldots\ldots (4)$$

$$O^* = O - \frac{48}{54}(0.85Al) - \frac{16}{48}(0.70Ti) - 20 \ldots\ldots\ldots (5)$$

$$N^* = N - \frac{14}{48}(0.3Ti) - 20 \ldots\ldots\ldots (6)$$

where quantities for oxygen, nitrogen, boron, aluminum, and titanium are included in units of parts per million by weight, while others are inputted by wt.%. Also, as indicated in equation (3) and (4), oxygen decreases the value of CE (WM). The weld metals investigated in this paper do not involve boron. Most case for pipeline materials and welds also do not add boron to avoid hardening after thermal process such as welding. Therefore, in this case, ΔB_H=0 will be defined in equation (3) so the effect of titanium does not affect directly. The relationship between CE (WM) and hardness is illustrated in **Figure 2-15**. It can be found that hardness values have a strong correlation with CE (WM). Therefore, it is suggested that the hardness of weld metals can be fairly well estimated by using CE (WM), and this will help to establish limits for possible weld metal chemical compositions which can be considered for developing weld metals.
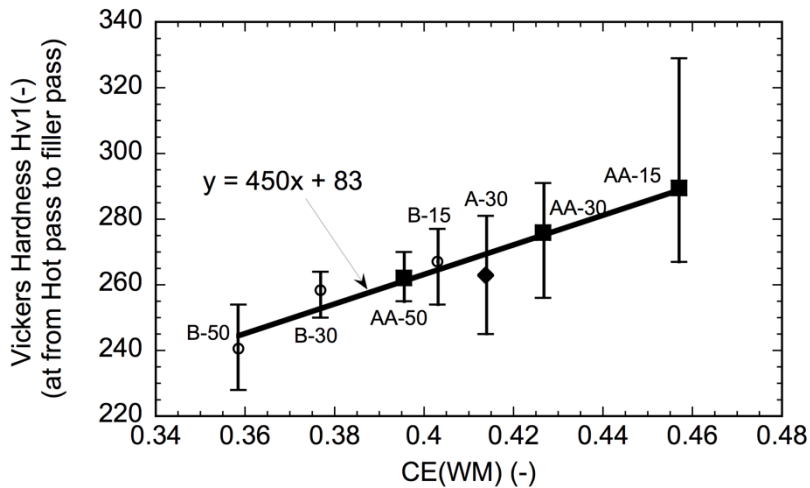
Figure 2-15 Relationship between carbon equivalent for weld metals and hardness in the welds

2.5 Conclusions for chapter 2

In this chapter, in order to maximize IGF volume fraction in weld metals, correlation between chemical composition, IGF volume fractions, and hardness values in the weld metals were investigated using varying weld metals produced by in-situ alloying thin titanium wire and employing various Ar/CO_2 ratio of shielding gas. The main findings are summarized as:

1. It was demonstrated that volume fraction of intragranular ferrite in the weld metals can be controlled with in-situ alloying thin pure titanium wire and applying shielding gas differed Ar/CO_2 ratio.

2. It was indicated that the most effective balance between titanium and oxygen contents to maximize IGF corresponds to the ideal stoichiometry of Ti_2O_3.

3. It was found that the hardness of weld metals have strong correlation with the carbon equivalent for weld metals, CE (WM), which is consistent with prior work.

Chapter 3
Effects of microstructures in terms of Sulphide Stress Cracking susceptibility of GMA girth welds in X80 grade pipes

3.1 Introduction

As mentioned in Chapter 1, the acicular ferrite microstructure consisting of fine intragranular ferrite (IGF) might decrease Sulphide Stress Cracking (SSC) susceptibility because of dispersed trapping of hydrogen by fine grains, restraint of mobile dislocations which can carry diffusible hydrogen via pinning at nano-carbides, etc. Furthermore, in Chapter 2, methods to maximize IGF volume fraction in gas metal arc weld metals were discussed. The present chapter discusses the results of SSC testing performed on weld metals with varying ratios of intragranular ferrite (IGF) and grain boundary ferrite (GBF). Next, the observation of hydrogen trapping site is demonstrated, where, a novel combination of hydrogen microprinting combined with SEM and TEM electron microscopy analysis techniques are applied. Based on those results, the roles of microstructure in terms of SSC susceptibility, and the correlation between microstructure, hardness, and SSC resistance in GMA welds are then evaluated for weld metals containing slightly different levels of titanium and IGF to GBF ratios.

3.2 Materials and experimental methods

The specimen list employed for the SSC tests is shown in **Table 3-1**. The specimen IDs corresponding with the IDs mentioned in Chapter 2. In order to explain the methods used to fabricate those specimens, it is worthwhile to review the parameters used during welding. All specimens were produced by robotic gas metal arc (GMA) welding with a U-shape groove in butt joint configuration, in the flat position. Pipe segments from 1/8 circumferential sections of API 5L X80 grade pipe of 610mm (24") diameter and a 15.1mm thickness was used as the base material, with sample lengths of approximately 230mm.

Table 3-1 Specimen list for SSC test

Specimen ID	Welding wire	Shielding gas	Chemical composition of weld metals (wt.%)								
			C	Si	Mn	P	S	Al	Ti	O	N
A-30	Wire A	70%Ar-30%CO$_2$	0.082	0.48	1.69	<0.010	<0.005	<0.01	0.01	0.029	0.0032
AA-30	Wire A +Ti wire	70%Ar-30%CO$_2$	0.082	0.53	1.72	<0.010	<0.005	<0.01	0.04	0.026	0.0036
AA-50	Wire A +Ti wire	50%Ar-50%CO$_2$	0.079	0.47	1.63	<0.010	<0.005	<0.01	0.03	0.027	0.0036
B-30	Wire B	70%Ar-30%CO$_2$	0.055	0.50	1.66	<0.010	<0.005	<0.01	0.03	0.031	0.0039

In order to obtain varying weld joints which have differing IGF volume fraction, the titanium and oxygen contents were controlled by adding a thin titanium wire and employing shielding gases with varying Ar to CO_2 ratios, since it is well known that this will promote formation of titanium oxides which act as nucleation sites for acicular ferrite in weld metals. Titanium content in the weld metals was varied by using two kinds of welding consumables; wire "A" which did not include titanium, and wire "B" containing 0.06 wt. %. A third variant, designated "AA" was produced through in-situ alloying by adding a 0.2mm diameter titanium wire, where the wire was fixed before welding by resistance spot welding every approximately 10 centimeters in order to avoid being blown away by shielding gas and arc plasma. The oxygen content which is another key element to form titanium oxides was controlled by utilizing two shielding gases; Ar + 30% CO_2 and Ar + 50% CO_2 (described as AA-30 and AA-50 respectively). The chemical compositions of the weld metals are also shown in **Table 3-1**, which were measured in accordance to ASTM E1019-11, E2097-12(modified), and E1479-99(2011).

Multi-pass GMA welding utilizing six passes was performed by applying the following welding conditions for the wire current, voltage, and travel speed; 290-320A, 24.5-28.0V, and

56

120cm/min for the root pass, 280-310A, 24.5-28.0V, and 70cm/min for hot and filler pass, and 210-230A, 21.5-25.0V, and 30cm/min for the cap pass. Preheat and interpass temperatures were controlled by limiting them to 150°C.

After welding, Vickers hardness testing and metallography were conducted in order to evaluate properties for all weld metals. Test specimens for those were extracted from near crater at the end of welding bead for each specimen. The conditions for the Vickers hardness test were determined at 9.8 N load and 0.5mm pitch, in which the sampling position was a line 2mm from the bottom edge (inner diameter) of the pipe as shown in **Figure 3-1**, where the position of the hardness test is noted by the label.
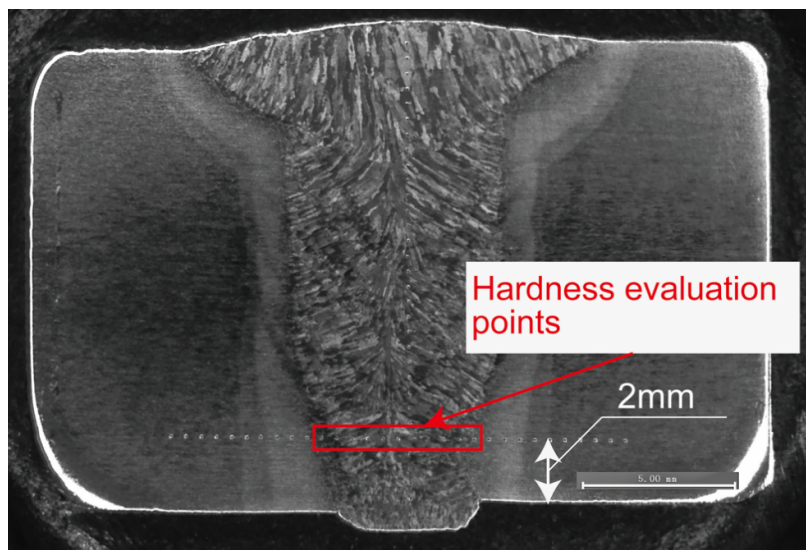
Figure 3-1 Hardness evaluation points

After hardness testing, all specimens were re-polished and etched with 5% Nital solution to observe the microstructure using an optical microscope. The volume fraction of IGF was investigated by point counting method, where a grid was drawn at a 10 micrometer pitch on micrographs taken at 200x magnification (for a total of 896 cross points per micrograph). The number of intersections for each microstructure were counted, and the average and standard deviation were calculated based on

the data of five pictures for each specimen. In this paper, microstructures were distinguished as grain

boundary ferrite (GBF), IGF (which was predominantly acicular ferrite, but could also include

Widmanstätten ferrite + polygonal ferrite + bainitic ferrite), and bainite (B, upper and lower bainite).

SSC tests were conducted according to NACE standard MR0175/ISO 15156 [2] and EFC

No.16 [3]. The dimension of the SSC test specimen is illustrated in **Figure 3-2**. The size of the

specimen is 15mm width, 115mm length, and 5mm thick, and three specimens were extracted from

each welded joint as the weld metal is positioned at the center of the specimen. The cutting plan of

cross section is illustrated in **Figure 3-3**. Each specimen was extracted from a position 2mm from the

inside surface of the base metals.
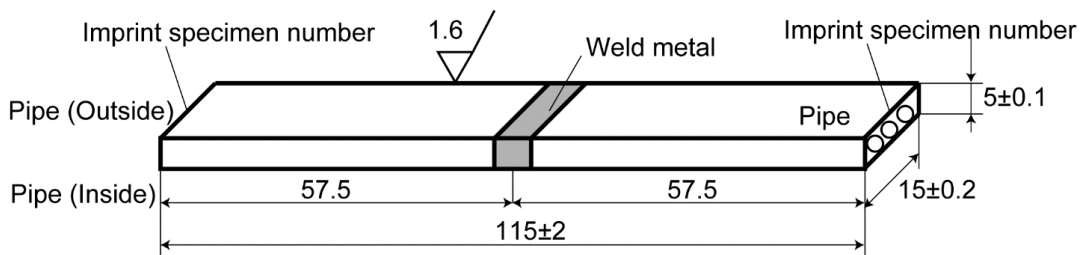
Figure 3-2 SSC test specimen
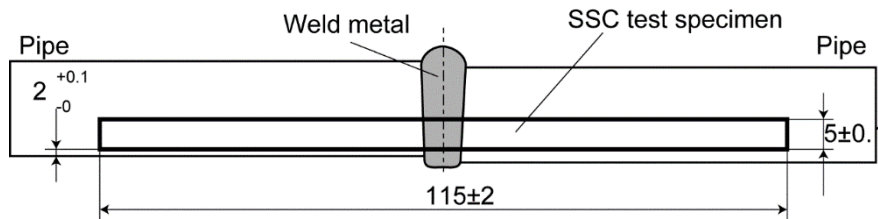
Figure 3-3 Extraction position for SSC specimen

The samples were loaded with bending fixtures so that the weld metal on the inner side of the pipe wall was under tensile stress during SSC tests. Three levels of stress were applied (nominally 452MPa, 480MPa, and 509MPa), which corresponded to 80%, 85%, and 90% of the actual yield stress for the base materials, while the joint A-30 was only tested at 480 MPa. 4-point and 3-point bending methods were employed to load the required stress. The actual yield stress of the base material was previously measured by tensile testing, which indicated a value of 565 MPa. Initially, the AA-30 series was tested with a 4-point bending method because the method can uniformly stress the welded area including weld metal, heat affected zone, and base metals; however, one specimen failed by crack initiation from the fusion line rather than the weld metal. Since the purpose of this paper is to investigate SSC susceptibility for weld metals, the method of loading was revised to the 3-point bending method for the remaining specimens in order to ensure the highest stress concentration was within the weld metal. A schematic of the 3-point bending is illustrated in **Figure 3-4**. During pre-loading of the specimens for SSC testing, deflection y is calculated with the formula;

$y = \sigma H^2/6Et$

where, y: Deflection (between outer supports) [mm]

σ: Applied Stress [MPa]

t: Thickness of specimens[mm] =5mm

E: Young modules [MPa]

H: Distance between outer supports [mm] =98.43mm

Target deflections were calculated with the formula, this is according to ASTM G39 [80] and loaded at the three levels of applied stress.
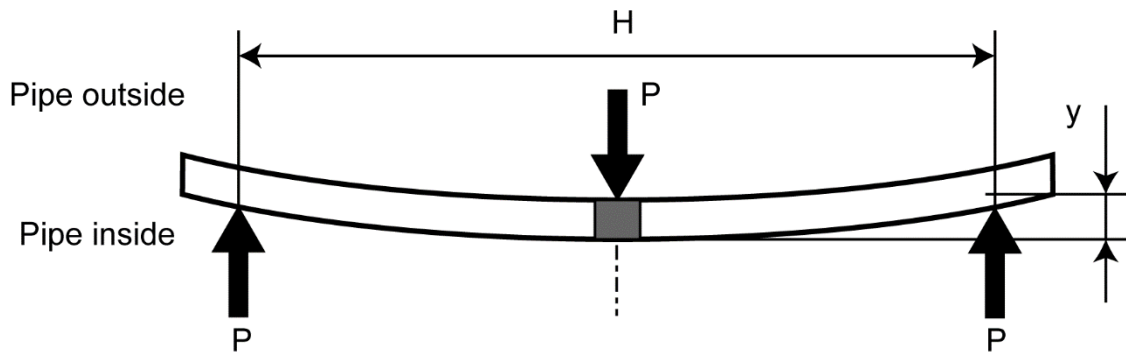
Figure 3-4 Schematic of 3-point bending

The illustration of the SSC test is shown in **Figure 3-5**. During the SSC test, one may select the most appropriate acid solution for the test according to the NACE standard. In this research, NACE "A" solution (5.0 wt. % sodium chloride and 0.5 wt. % glacial acetic acid in distilled water) was employed [2]. In this test, three test specimens were repeated from the same weld series, and immersed into one chamber after loading the bending fixtures, respectively. Then, hydrogen sulphide gas was injected to a saturating condition, a slight hydrogen sulphide gas was kept on charging to maintain the saturating condition. Then pH of the solution should be less 3.0 (while the typical pH range is 2.6 to 2.8 before testing), and the pH shall not exceed 4.0 during test. In this test, the pH of the solution was monitored by a pH meter during the SSC test throughout the 720 hours (30 day) test time, then it was confirmed that maximum pH during testing was 3.81, and pH at the finishing time of the test was 3.6.

After testing, a nitrogen purge was employed to reduce the concentration of hydrogen sulphide in the chamber, then the test specimens were taken out. In order to confirm that SSC occurred, visual inspection and magnetic particle inspection (MPI) were conducted after cleaning of the test specimen with acid solution. Furthermore, hardness testing was conducted to compare the hardness between before and after the SSC test.
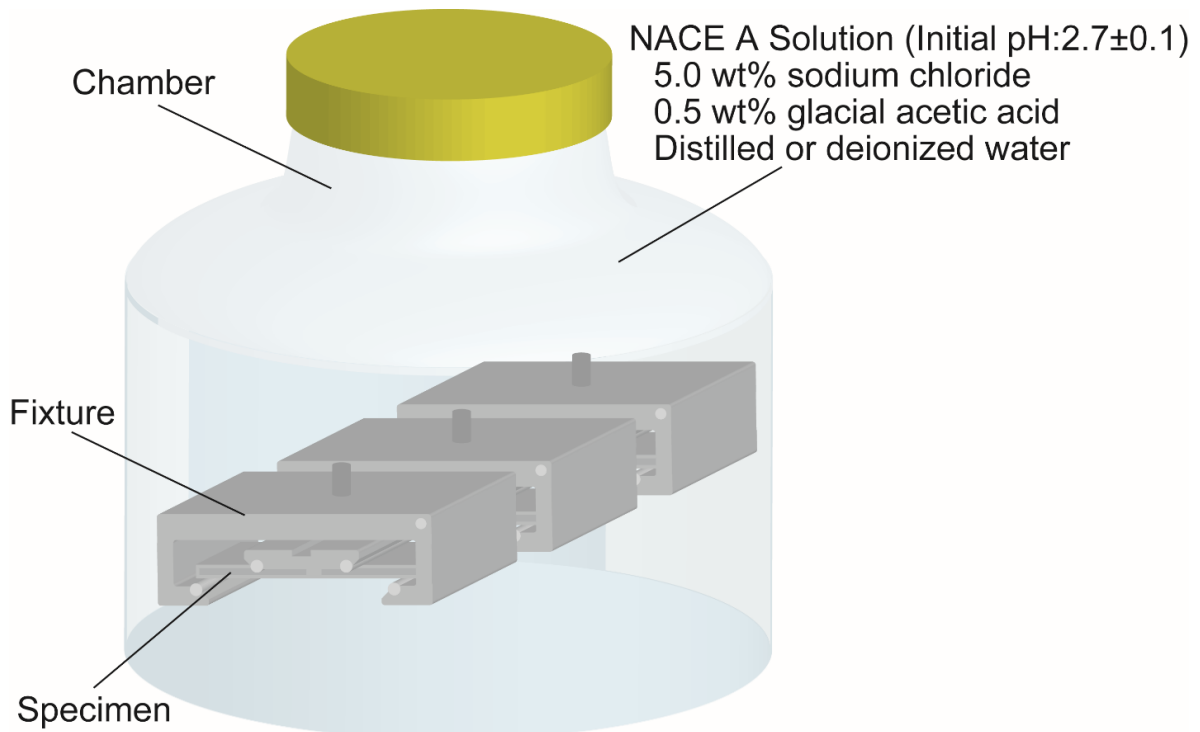
Figure 3-5 Schematic of the SSC test

It is well known that the hydrogen microprint technique is one of the methods to reveal hydrogen trapping sites in the microstructure, since it relies on a reaction between silver bromide and hydrogen [81-84]. A specimen with a 2mm thickness was extracted from the AA-50 weld metal and was found to contain a marginally higher IGF volume fraction than the other welds (refer to **Figure 3-8**). The hydrogen microprint procedure employed in this research is illustrated in **Figure 3-6**. First of all, the specimen was mounted with conductive resin and polished with # 600 grit paper. Then the specimen was connected to the cathode side of a constant current generator and immersed in 0.1M NaOH at room temperature, where a Pt plate was utilized as a counter electrode. The electrical charging was performed, with a current density of $27mA/cm^2$ for approximately 110 hours (4 days and 15 hours) to promote hydrogen saturation at the surface. During charging, the solution had been supplied once a day because of evaporation of the solution. After hydrogen charging, the specimen

was re-polished quickly with alumina paste then 1 micron diamond paste, then covered by with liquid emulsion (Ilford L4 which contains AgBr particles 0.11 μm in size, diluted with 1.4 mol/L $NaNO_2$ solution) with a wire loop method [81-84]. After drying for approximately 30 minutes, the specimen was kept at 150 °C for 3 hours in order to promote a chemical reaction between silver bromide and hydrogen. For hardening, the specimen was subsequently dipped in formalin (37 mass% HCHO water solution) for approximately 3 seconds then for fixing, the specimen was immersed in a fixing solution (15 mass% $Na_2S_2O_3$ with 1.4 mol/L $NaNO_2$ solution) for about 5 minutes. After that the specimen was cleaned with distilled water. Through this process, silver particles precipitated on the surface, the locations of hydrogen trapping sites were then observed by Scanning Electron Microscope (SEM). Moreover, the particles were confirmed that the precipitates were compounds involving silver with Energy Dispersive X-ray Spectrometry (EDS).
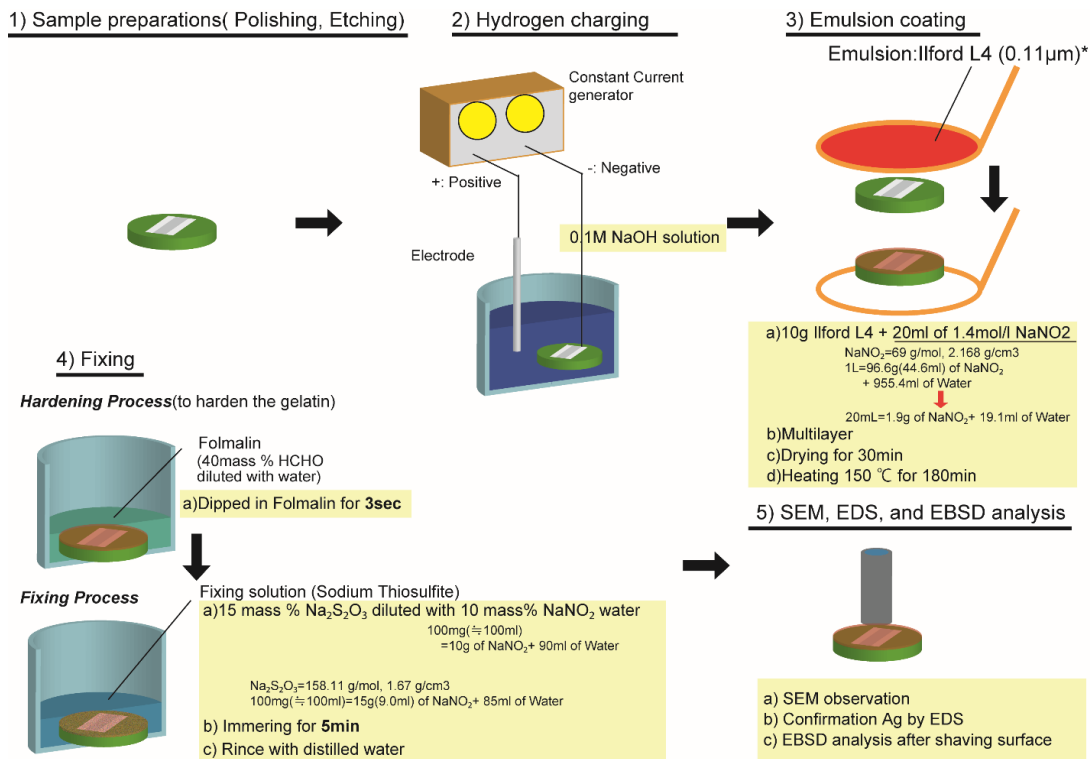
Figure 3-6 Schematic for procedure of hydrogen microprint technique

Finally, the specimen surface was ion milled approximately 0.1-0.2µm to remove the silver particles

and surface deformation utilizing a tilted focused ion beam, where an Ar beam was used for ion

milling for 60 seconds. Electron Back-Scattered Diffraction (EBSD) analysis was carried out on the

surface to reveal more detail regarding the locations of silver particles, in terms of grain boundary

characteristics, using a step size of 0.6 µm, with an accelerating voltage of 20kV. Data collection

during EBSD involved fitting to within a mean angular deviation (MAD) factor of less than 0.6, and

no further filtering was used to interpolate non-indexed points.

Furthermore, in order to investigate differences in microstructure at the nano-scale level,

Transmission Electron Microscopy (TEM) observation was also performed at the Canadian Centre for

Electron Microscopy in Hamilton Ontario, using an FEI Titan 80-300 LB, operated at 300 kV.

Specimens for TEM were extracted using focused ion beam (FIB) milling, performed using a Zeiss

NVision 40. The steps of this milling process for the sample extraction are shown in **Figure 3-7**. First

of all, the position of specimen extraction was determined by observation in the SEM. Next, a layer of

tungsten was deposited on the plane of the specimen to prevent excavating the material. Further low

energy milling was performed in multiple steps at 10 kV and 5kV to remove amorphous material

from the surfaces. These specimens were used to observe nano-scale inclusions and dislocation

structures in the weld metals.
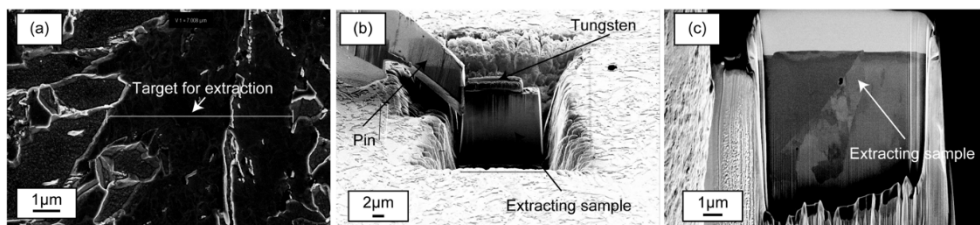
Figure 3-7 Schematic of the milling process for the sample for TEM observation with a focused ion

beam, (a) Target selection for sample extraction by SEM, (b) Excavating situation around an

extracting sample, (c) Lifting up for an extracting sample

3.3 Results of each analysis and SSC test

A comparison of the microstructures in the weld metals by optical microscopy is demonstrated in **Figure 3-8**. It can be observed that intragranular ferrite (IGF), which includes acicular ferrite or other microconstituents nucleated within the interior of prior austenite grains, is the most dominant structure for all welds. The IGF volume fraction was quantified by the point counting method by evaluating five fields dividing by 10 microns, and counting 896 points in each micrograph. As shown in **Figure 3-8**, 88% or more of each weld corresponds to IGF. The average and calculated standard deviation across five pictures for each specimen is also shown as IGF_{ave} and σ in **Figure 3-8**. The balance of the microconstituents aside from IGF was composed of grain boundary ferrite (GBF). It is worth noting is that Sample A-30 included a significantly lower IGF volume fraction (88%) than the other weld metals which ranged from 95 to 97%. This indicates that the fraction of GBF fraction in A-30 was significantly higher than the other specimens (12%, versus 3 to 5%).
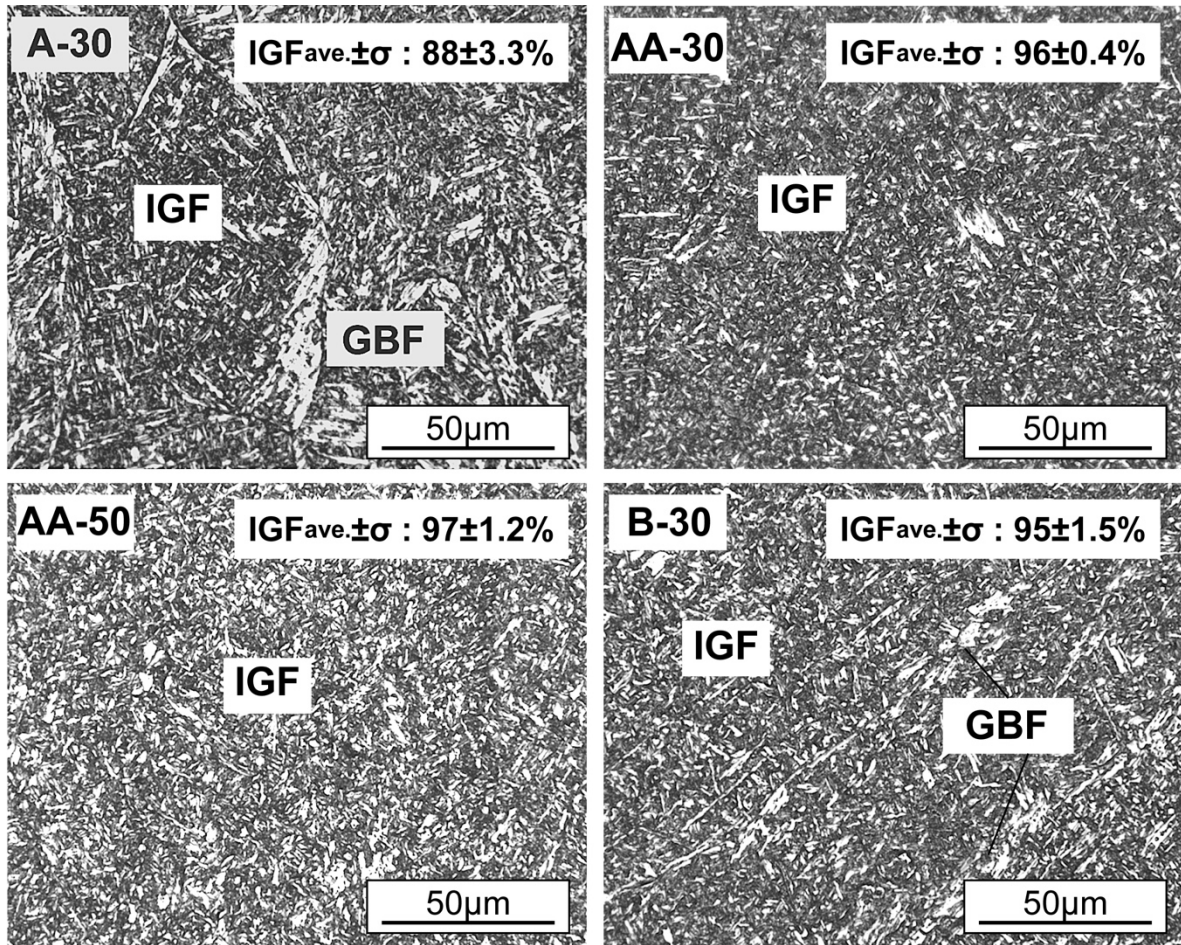
IGF: Intragranular ferrite, GBF Grain boundary ferrite, IGFave: IGF volume fraction averaged by five pictures
σ:Standard deviation

Figure 3-8 Comparison of the as-deposited microstructures in each weld metal

The hardness test results for each weld metal are show in **Table 3-2**. The average of hardness test results before the SSC testing indicates the values are exceeding 250 HV, which is a criterion limit of NACE/ISO standard and EFC publication [2, 3]. This point should be emphasized, considering these standards would lead one to expect that the specimens should not pass the SSC test.

Table 3-2 Hardness test results before SSC test

Specimen ID	Welding wire	Shielding gas	Hardness, 2mm from pipe bottom surface, HV_{98N}	
			Maximum	Mean,$\pm\sigma$
A-30	Wire A	70%Ar-30%CO_2	258	251±11.7
AA-30	Wire A+Ti wire	70%Ar-30%CO_2	295	273±11.7
AA-50	Wire A+Ti wire	50%Ar-50%CO_2	268	257±5.6
B-30	Wire B	70%Ar-30%CO_2	267	259±6.3

SSC test results are summarized in **Table 3-3**, and the surface condition of all specimens after cleaning by ultrasound plus, nylon brush, and acid solution (10%HCl) for highly adherent layer, are shown in **Figure 3-9**. The joints comprising weld metals A-30 and AA-30 series were rejected following the SSC test, since it could be observed that a crack had initiated. All specimens for AA-50 series and B-30 series, however, were considered acceptable and did not suffer from crack initiation, despite a hardness value exceeding 250 HV. It can be seen that the influence of applied stress may not be directly correlated to crack susceptibility from those results, although SSC initiation should be affected by applied stress level. The macrograph of the A-30 specimen after the SSC test is demonstrated in **Figure 3-10** as one of the examples of a rejected specimen. It can be seen that the SSC initiated at root area in the weld metal and propagated through the bead center along the grain boundaries.

Table 3-3 SSC test results

Specimen ID	Welding wire	Shielding gas	Results of SSC tests	
			Applied Stress (MPa)	Acceptability
A-30	Wire A	70%Ar-30%CO_2	480	Rejected
AA-30-1	Wire A+Ti wire	70%Ar-30%CO_2	452	Rejected
AA-30-2	Wire A+Ti wire	70%Ar-30%CO_2	480	Rejected
AA-30-3	Wire A+Ti wire	70%Ar-30%CO_2	509	Rejected
AA-50-1	Wire A+Ti wire	50%Ar-50%CO_2	452	Acceptable
AA-50-2	Wire A+Ti wire	50%Ar-50%CO_2	480	Acceptable
AA-50-3	Wire A+Ti wire	50%Ar-50%CO_2	509	Acceptable
B-30-1	Wire B	70%Ar-30%CO_2	452	Acceptable
B-30-2	Wire B	70%Ar-30%CO_2	480	Acceptable
B-30-3	Wire B	70%Ar-30%CO_2	509	Acceptable
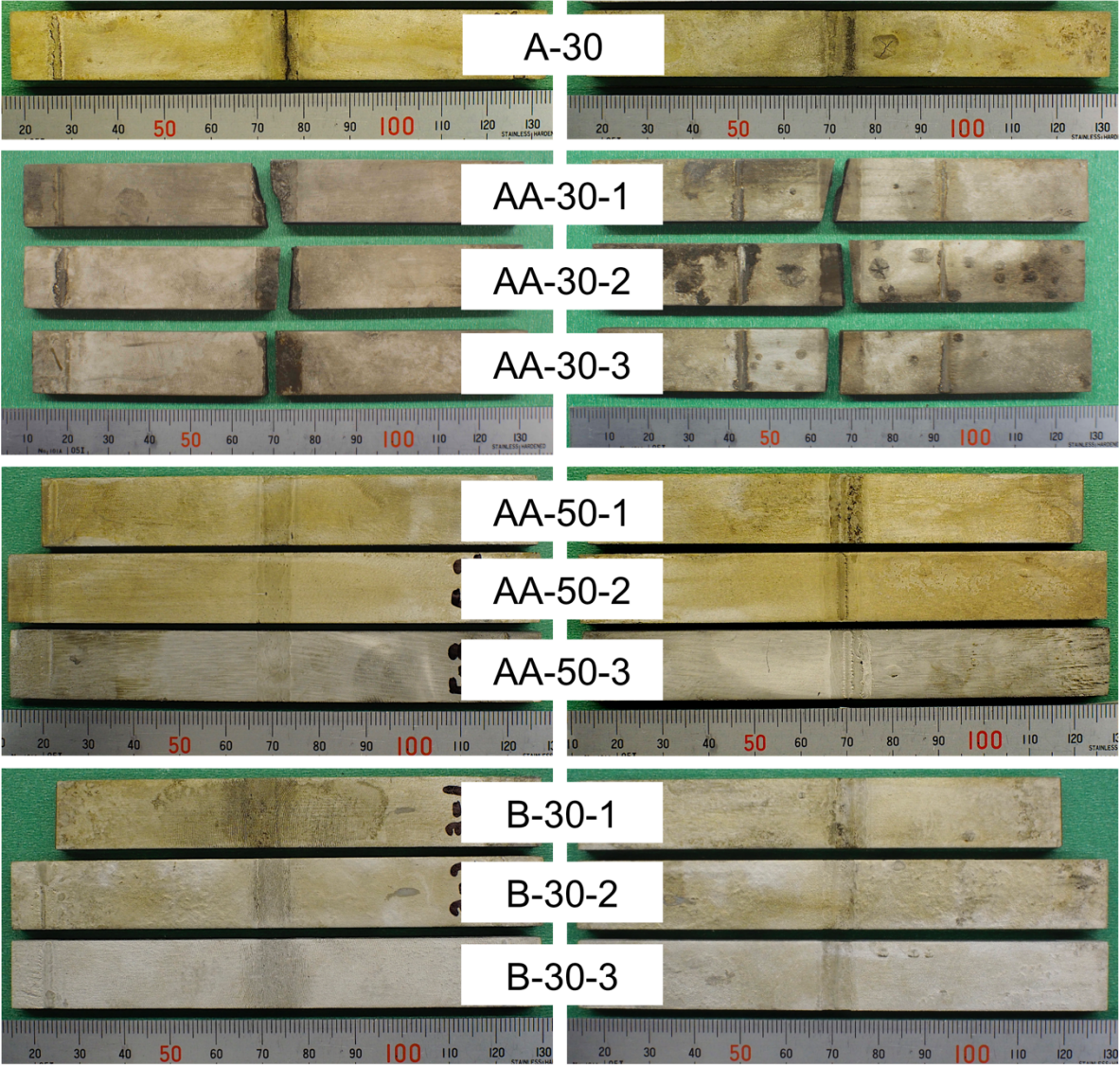
Tensile surface side   Compressive surface side

Figure 3-9 Surface condition of all specimens after SSC testing (after cleaning)
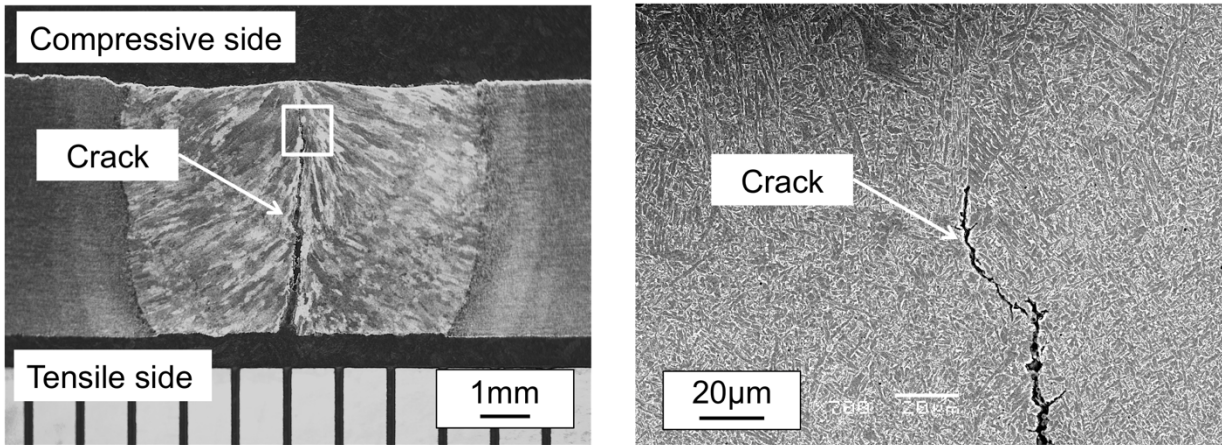
(a) Macro photo for cracked specimen (A-30)

(b) SEM photo focused on the crack tip in cracked specimen (A-30)

Figure 3-10 Macrograph of the A-30 specimen after the SSC test

A comparison of the hardness values before and after SSC testing are given in **Table 3-4**. For all specimens, the hardness values after the SSC test are slightly higher, especially the A-30 weld which exhibited the most significant increase. Moreover, it can be seen that the increase in average hardness after SSC testing is higher (13.3 to 22.7 HV) when using welding consumable A is employed than when welding consumable B is used (4.7 HV).

Table 3-4 Comparison of hardness value between before and after SSC testing

Specimen ID	Hardness, 2mm from pipe bottom surface, $HV_{9.8N}$		Hardness, after SSC test, 0.2mm from tensile surface, $HV_{4.9N}$		Difference before and after SSC			
	Maximum	Mean, $\pm\sigma$	Maximum	Mean, $\pm\sigma$	ΔMax	Avg. of Max $\pm\sigma$	ΔMean	Avg. of Mean $\pm\sigma$
A-30	258	251±11.7	291	283±8.5	33	33	32	32
AA-30-1	295	273±11.7	330	295±13.7	35	20.7±12.7	22	22.7±5.7
AA-30-2	295	273±11.7	300	289±6.6	5	20.7±12.7	16	22.7±5.7
AA-30-3	295	273±11.7	317	303±15.4	22	20.7±12.7	30	22.7±5.7
AA-50-1	268	257±5.6	287	270±8.2	19	16.0±2.2	15	13.3±1.2
AA-50-2	268	257±5.6	282	257±5.3	14	16.0±2.2	13	13.3±1.2
AA-50-3	268	257±5.6	283	269±7.5	15	16.0±2.2	12	13.3±1.2
B-30-1	267	259±6.3	281	262±11.8	14	10.3±2.9	3	4.7±2.4
B-30-2	267	259±6.3	274	262±7.4	7	10.3±2.9	3	4.7±2.4
B-30-3	267	259±6.3	277	267±7.1	10	10.3±2.9	8	4.7±2.4

The distribution of hydrogen trapping sites revealed by the hydrogen microprint technique is shown in **Figure 3-11**. For the procedure, the locations of the silver particles were revealed by EDS mapping first, then the surface was cleaned up by milling utilizing a tilted focused ion beam in order to remove surface layers strained by mechanical polishing before EBSD mapping. The milling process using an ion beam was able to remove most of the silver particles. After this ion milling, the location mapped by EDS was also analyzed by EBSD; however, in some locations many silver particles were found to have low EBSD indexing rates due to reduced ion milling rates of the silver. So, the locations that silver particles were removed was selected for the EBSD analysis.

(a) SEM photo

(b) Distribution of silver obtained with EDX

(c) Distribution of silver and grain boundaries of IGF obtained with EBSD
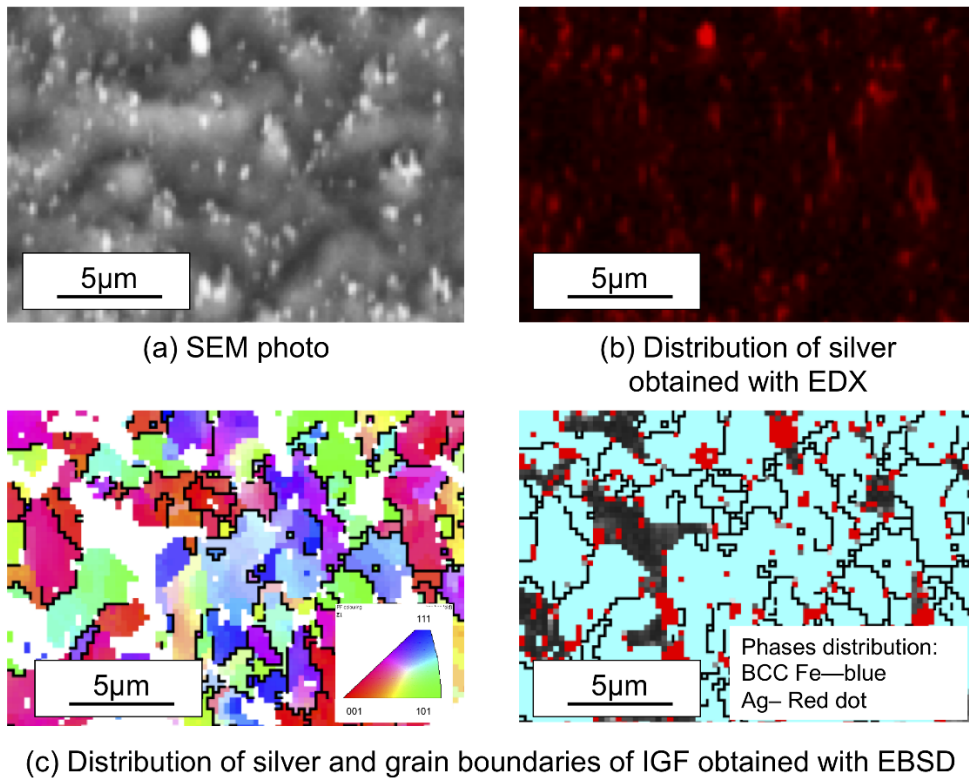
Figure 3-11 Distribution of hydrogen trapping site revealing by combination method of hydrogen microprint technique and EBSD

Figure 3-11 (a) shows the SEM micrograph of the surface containing silver nanoparticles, while (b) indicates the distribution of silver particles, which was obtained based on EDS mapping. From those results, it is noted that the particles distributed on the surface in **Figure 3-11**(a) are composed of silver. The result of EBSD analysis on this same location is illustrated in **Figure 3-11**(c), where the color into the figure means phase orientation. Some white areas indicate locations which suffered poor EBSD indexing shown in the left-hand figure (due to non-uniform ion milling caused by the prior presence of silver). In the right-hand figure, red dots indicate silver and the black lines indicate the high angle grain boundaries misorientations of more than 15 degrees. The results of measurement for the silver locations are shown in **Table 3-5**. It can be noted that location of the silver particles almost all corresponding to the locations of black lines. In other words, locations of the red dots, silver particles coincide with grain boundaries of acicular ferrite, while fewer silver particles were detected within the interior of grains. According to Koyama et al. [82], more hydrogen can be trapped at high angle grain boundaries than low angle grain boundaries, and the segregation and accumulation of hydrogen at grain boundaries increases with hydrogen flux. The results obtained in this research are in support of this finding as well.

Table 3-5 Measurement result of silver location in Figure 3-11(c)

Locations	Number of pixels (Pixels)	Percentage (%)
Grain boundaries in IGF	284	81
Inner grain	27	8
Ambiguity	39	11

Total number of pixels = 4292 pixels
Total number of pixels for silver particles = 350 pixels

3.4 Discussions

SSC initiated in all the A-30 and AA-30 series welds as shown in **Table 3-3**, although it was not observed in A-50 series and B-30 series. Weld metals of AA-30 series contained a much higher volume fraction of IGF and they exhibited high hardness, with a maximum exceeding 290 HV. According to NACE MR0175/ISO 15156 and EFC publication number 16, the critical hardness value should be less than 250 HV. This is based on the principle that one must avoid local hard microconstituents with high hardness that will be prone to concentrating hydrogen and initiating a crack. The average hardness values of AA-30 series specimens were uniform and exceeded 250HV; thus, it would be expected that the weld metals would not be able to survive this SSC test.

In contrast, the specimens comprising the A-30, AA-50, and B-30 series welds appeared to exhibit almost the same hardness values before and after the SSC test, but the A-30 specimens were the only material to fail the SSC test, so it is worth further consideration in terms of this result. First of all, the IGF volume fraction of A-30 weld metal was lower than others. As shown in **Figure 3-11**, hydrogen trapping sites correspond to IGF grain boundaries. Hence, in the case of higher IGF volume fraction, the ability to trap diffusible hydrogen would be excellent. According to Wang et al., diffusible hydrogen can be trapped at grain boundaries in acicular ferrite, which is one type of IGF noted in the investigation of the effect of acicular ferrite in submerged arc weld metals [55]. The present results are consistent with this work, although the welding process is different. Additionally, Zhao et al. mentioned that nano-sized carbides within IGF provide hydrogen trapping sites [48, 49]. A micrograph of grain boundary of an IGF in A-30 weld metal taken by TEM is shown in **Figure 3-12**. This was observed in the root area of the weld metal after extracting by in-situ lift-out using ion milling. The IGF microstructure was analyzed by bright field TEM, which reveals nano-sized precipitates noted by the white arrows in **Figure 3-12**. Those precipitates are extremely similar to the morphology, size, and distribution, previously reported for similar material in the results by Zhao et

al. [48, 49]. Hence, it can be noted that those precipitates are likely to be carbides and their role in trapping diffusible hydrogen is similar. It is suggested that, therefore, a rich density of nano-scale carbides in the IGF regions should reduce SSC susceptibility.
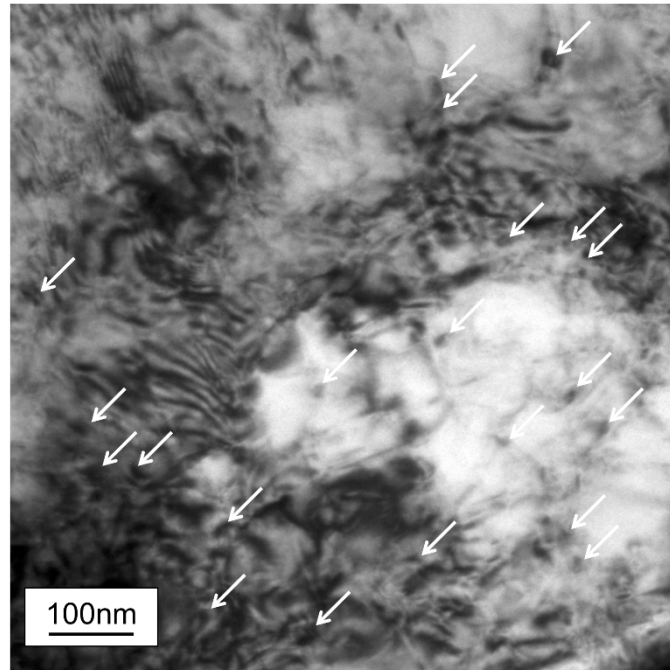
Figure 3-12 Carbides observed by TEM in A-30 weld metal

On the other hand, the A-30 series specimens contain much more GBF compared with AA-50 and B-30 series. In addition, as indicated in **Figure 3-10**, SSC propagated though prior austenitic grain boundaries. Therefore, the influence of GBF located near prior austenitic grain boundaries is also important to consider, and the following two hypotheses can explain the effects of GBF on SSC susceptibility. First of all, the grain size of GBF is larger than IGF typically. It is well known that fine grains provide high fracture toughness so that weld metal containing much more IGF will resist SSC crack propagation. Secondly, if local yielding occurs during SSC test, dislocations which can transport diffusible hydrogen would be accumulated in the GBF, especially around the crack since

GBF has a low strength compared to IGF due to a coarse grain size. Based on this hypothesis, GBF would suffer brittle fracture by concentrating diffusible hydrogen during SSC testing. In order to test this second hypothesis, the difference in dislocation density in the GBF of the weld metal both before SSC testing (at the root area, 2 mm from inner surface), and near a crack tip after SSC were investigated. The precise location for the test coupon extractions are illustrated in **Figure 3-13**, which was observed by SEM.

The bright field image micrographs for each location are shown in **Figure 3-14**. It seems that there is no clear difference between the dislocation density in GBF at the SSC crack tip and the virgin material. Thus, the second hypothesis that the dislocations will increase within the GBF due to locally low strength could not be confirmed. Hence, the results indicate that the first hypothesis, that GBF has a low fracture toughness derived from a coarser grain size, is main reason for deteriorated SSC resistance. According to Lopez et al. [85], SSC propagated among prior austenitic grain boundaries in the case of API 5L X80 pipeline steels, and they claim that certain impurities, such as phosphorous are typically brittle, segregate at grain boundaries, and facilitate crack propagation along the grain boundaries. This indicates GBF, or grain boundaries in GBF exhibits low fracture toughness compared with IGF. As mentioned above, specimen A-30, which involves more GBF indicated a poor SSC susceptibility compared with AA-50 series and B-30 series were confirmed. It can be suggested that therefore decreasing the GBF volume fraction is desirable to avoid SSC initiation.
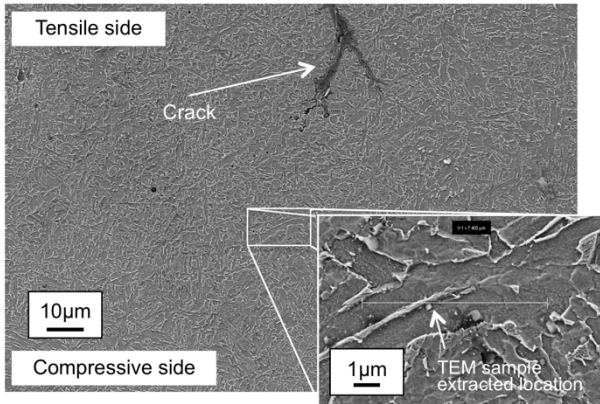
(a) TEM sample extracted location
at near crack tip in A-30
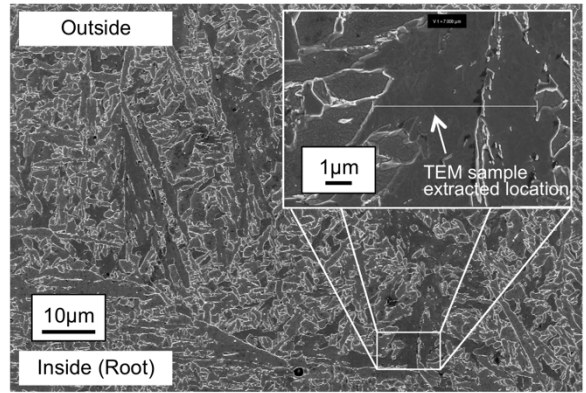
(b) TEM sample extracted location at
near tensile side in the virgin specimen

Figure 3-13 TEM specimen extraction location prepared by focused ion beam milling, (a) TEM

sample extracted location at near crack tip in A-30, (b) TEM sample extracted location at near tensile

side in the virgin specimen
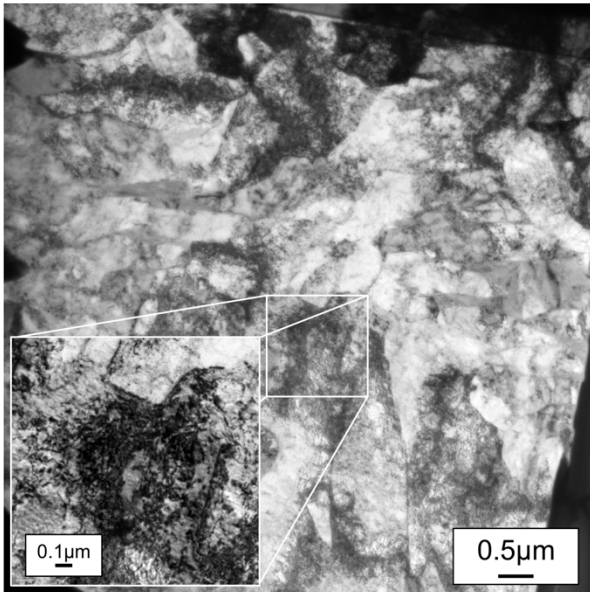
(a) A GBF near crack tip
in the cracked specimen
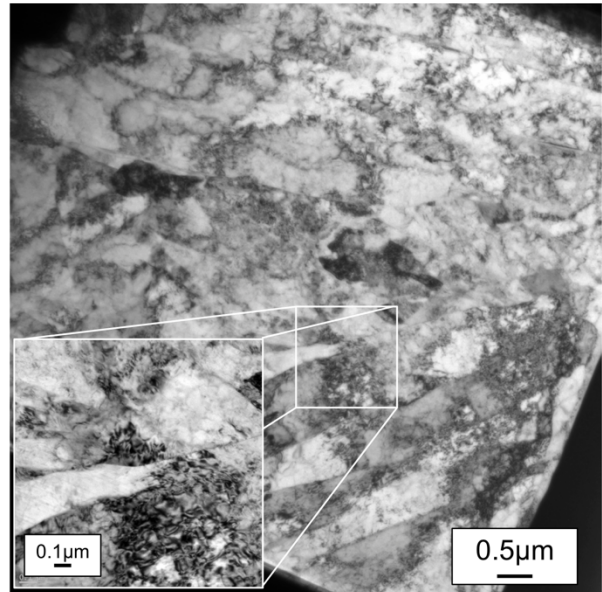
(b) A GBF near tensile surface
for the virgin specimen

Figure 3-14 Comparison of dislocations at a location of grain boundary ferrite, (a) A grain boundary

ferrite at near crack tip in the cracked specimen, (b) A grain boundary ferrite at near tensile surface

for the virgin specimen

76

Finally, the difference between the performance of B-30 series and AA-50 series weld metals is worth comparing. As shown in **Table 3-1**, both were judged acceptable by the SSC test. Based on the difference of chemical composition in weld metals, it is found that carbon contents of B-30 series is lower than in the AA-50 series, refer to **Table 3-1**. It has been reported that lower carbon contents result in lower hardenability [86, 87], so B-30 series are difficult to be hard comparing with AA-50 series potentially. Actually, the difference of hardness before and after SSC testing was less pronounced for the B-30 series than the AA-50 series as shown in **Table 3-2**. This might indicate that B-30 series do not involve much hard phases which can trap hydrogen than AA-50 series. Furthermore, Pcm value which is an index used to evaluate hydrogen crack susceptibility for B-30 and AA-50, was determined to be 0.20 and 0.23 respectively, where the Pcm value of weld metal has been suggested to follow the following equation [88].

$$Pcm = C + Si/30 + Mn/20 + Cu/20 + Ni/60 + Cr/20 + Mo/15 + V/10 + 5B \text{ [wt. \%]}$$

Based on this, series B-30 has a lower Pcm value than AA-50; thus, this it would have lower hydrogen susceptibility. Hence, B-30 might have lower SSC susceptibility than AA-50, based on the lower carbon content and Pcm value.

3.5 Summary of Chapter 3

In this chapter, by conducting SSC testing using varying welded joints differing IGF volume fraction, the influence of SSC susceptibility on microconstituents was investigated. The knowledge obtained in this research is shown in below.

1) The weld specimens with the highest intragranular ferrite to grain boundary ferrite ratio passed SSC tests, although they exhibited hardness values exceeding 250 HV, which is the accepted threshold guideline to avoid SSC initiation.

2) Grain boundaries of intragranular ferrite act as key hydrogen trapping site based on their fine grains and finely dispersed nano-size carbide precipitates.

3) Microstructures containing more grain boundary ferrite are potentially suffering from higher SSC susceptibility than one dominated by intragranular ferrite due to mainly low local fracture toughness deriving from coarse grain size.

As mentioned above, microstructure involving rich intragranular ferrite should be preferred to increase SSC resistance.

Chapter 4
Effects of hydrogen embrittlement on the mechanical properties of GMA girth welds in X80 grade pipes

4.1 Introduction

In Chapter 3, the role that microconstituents such as intragranular ferrite (IGF) and grain boundary ferrite (GBF) play on sulphide stress cracking susceptibility was investigated. Based on the experiments, it appears that a large IGF volume fraction leads to increased SSC resistance by providing hydrogen trapping sites at grain boundary interfaces provided by the fine ferrite size in IGF, while also increasing the fracture toughness as the grain size decreases. On the other hand, whether other mechanical properties change after hydrogen charging should be investigated. There are many research papers investigating hydrogen embrittlement fatigue properties, and tensile behavior in carbon steel charged with hydrogen [89-91]. Those studies, however, are focused on high carbon steels, while few papers have mentioned low carbon steel, especially in the case of weld metals. Therefore, the aim of this chapter is to investigate the influence of microstructure, especially weld metals based on IGF or acicular ferrite in low carbon steels with susceptibility to hydrogen embrittlement. In this chapter, two kinds of weld joints differing IGF volume fractions and hardness properties were produced, then mechanical properties including the tensile behaviour after hydrogen charging were investigated. The differences in behaviour is explained based on microstructural features observed via electron microscopy.

4.2 Experiments

Two kinds of weld joints were produced as shown in **Table 4-1**. Both were applied to join commercial API 5L X80 grade pipe of 24" diameter and 15.1mm thick base materials, and the same combination of welding wire and shielding gas were utilized as specimens A30 and AA-50 shown in Chapter 2 and Chapter 3. To produce the weld joints, pipe coupons were cut to lengths of

approximately 300mm along the axial direction, and 100mm in width along the circumferential

directions, then beveled to a U-shape groove when fitting the 300mm edges. The layout of the

welding set up are shown in **Figure 4-1**.

The welding joints were produced with robotic gas metal arc welding in a butt joint

configuration in the flat position. Multi-pass welding was performed by applying individual passes

utilizing the following parameters; 290-320A welding current, 24.5V-28.0V arc voltage, and

120cm/min travel speed for the root pass, with 280-310A, 24.5-28.0V, and 70cm/min for the (second)

hot pass and subsequent filler pass, and 210-230A, 21.5-25.0V, and 30cm/min for the final cap pass.

Preheat and interpass temperatures was maintained under 150°C before the first pass and between

passes. For the welding joints, one welding wire consumable was used to fill the joints, classified as

AWS A5.18, along with a thin commercially pure titanium wire of 0.2 mm diameter spot welded to

the weld metal surface, while two kinds of argon and carbon dioxide mixed shielding gas with

different ratios of 30 to 50% CO_2 were employed.

Table 4-1 Specimen List

Welding joint name	Welding consumable	Shielding gas
A-30	Wire A	70%Ar-30%CO_2
AA-50	Wire A + Ti wire	50%Ar-50%CO_2
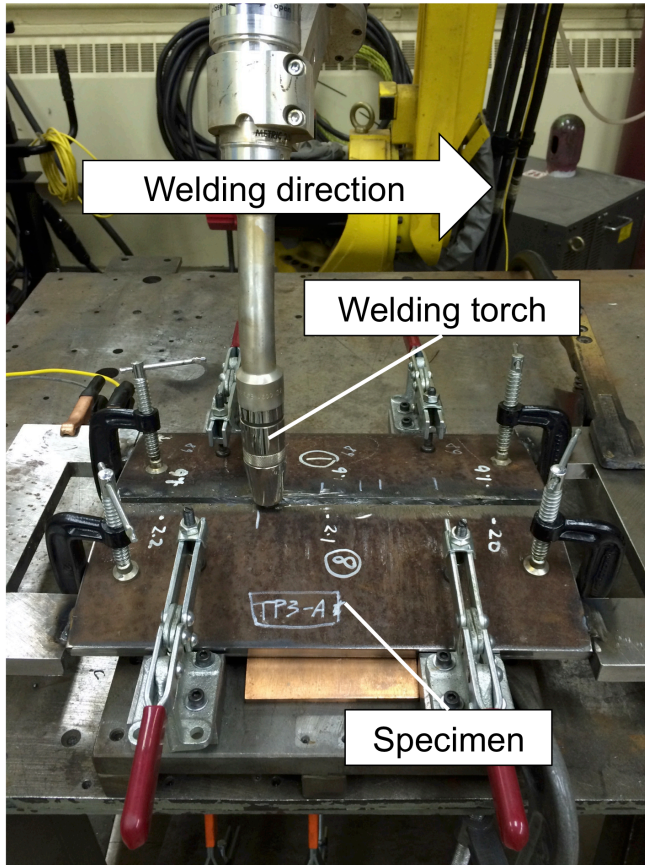
(a) Appearance of welding setup condition
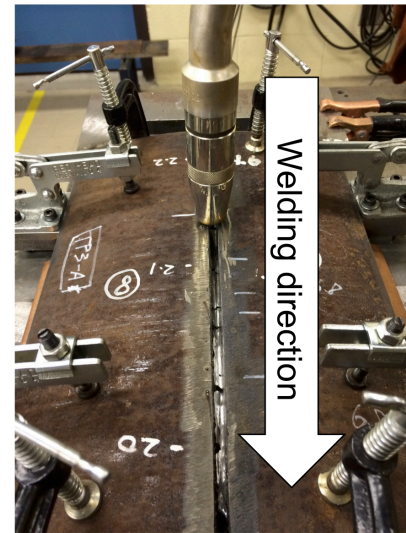
(b) View from welding direction
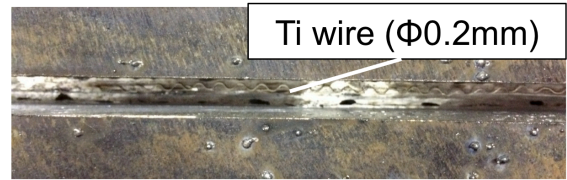
(c) Ti wire setting condition

Figure 4-1 Welding set up condition

The first joint test plate weld metal designated A-30 was produced by using only the welding wire consumable, and 70%Ar- 30%CO_2 premixed gas as a shielding gas. By contrast, a second test plate designated AA-50 included the commercially pure titanium 0.2 mm diameter wire inserted into the pool, which mixed into the molten weld metal to increase the amount of titanium. This in-situ titanium alloy was conducted in each weld pass of specimen AA-50 as shown in **Figure 4-1**(c). The actual titanium content in the weld metal of AA-50 containing the titanium wire was 0.02 wt.%, which was confirmed by chemical analysis conducted after welding. Also, 50%Ar-50%CO_2 premixed gas was employed as shielding gas to increase oxygen content in the weld metal. The main motivation for this alloy addition is to promote titanium oxide formation, which is well known to promote IGF

nucleation sites [52], which was achieved by a higher content of both titanium and oxygen in the AA-50 weld metal.

After welding, four tensile specimens were extracted from each weld metal, and the tensile specimen dimension are illustrated in **Figure 4-2**. As shown in **Figure 4-3**, the transverse location of two specimens are shown, and two sets of these were cut were cut from the axial length of the welding bead to obtain material from near center of weld metal. Three tensile tests were conducted following various levels of hydrogen charging for each weld joint. Hydrogen charging was performed by the electrical charging method, where 0.1M NaOH solution was used as an electrolyte. The amount of hydrogen charging was controlled by varying the current density and charging time. The A-30 weld series were charged in the following conditions; non-charged (N), 21mA/cm^2 current density for 4 days (CA), and 42mA/cm^2 for 6 days (CB), then AA-50 series were evaluated in the N and CB condition in addition an even more severe charging cycle of 84mA/cm^2 for 6 days (condition CC).
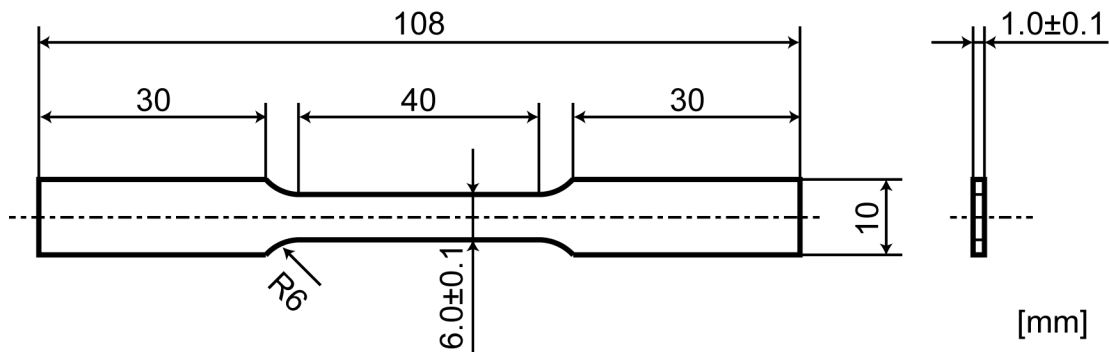
Figure 4-2 Dimensions of weld metal tensile specimen used to evaluate hydrogen charging on mechanical properties.
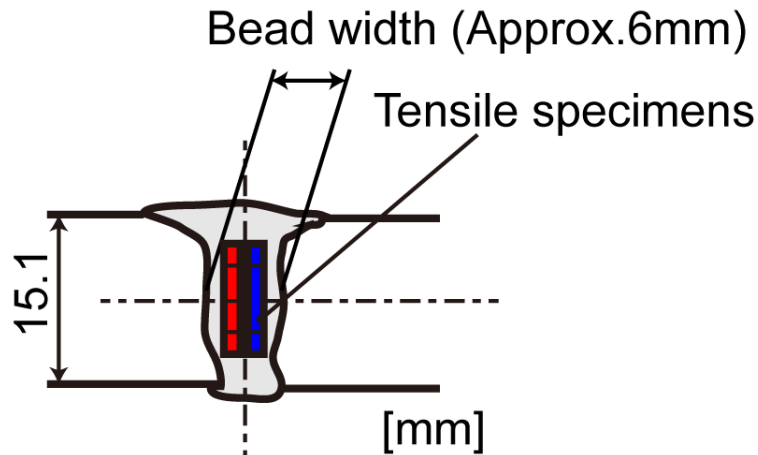
Figure 4-3 Transverse location of tensile specimens extracted from weld metal.

The tensile tests were conducted after removing the specimen from the beaker containing the 0.1M NaOH solution, rinsing and drying then mounting the sample in the tensile test frame to measure the properties within approximately 20 minutes. This was done in order to ensure that most of the diffusible hydrogen could also be retained within the sample during the test, considering that diffusible hydrogen will evolve from the samples over a period of up to 72 hours [92]. Digital image correlation (DIC) was applied during the tensile tests in order to obtain the local strain distribution data in the weld metal, heat affected zone, and base metal, especially in the necking area before fracture. A requirement for the DIC measurements included painting speckles onto the specimen, which accounts for part of the 20 minutes preparation time before tensile loading. Tensile tests were conducted at a constant rate of 1mm/min until fracture based on the crosshead displacement speed, corresponding to an initial strain rate of 4.2 x 10^{-4} /s.

Micro-Vickers hardness tests were also conducted at a position 5mm away from the edge of the grip area of the tensile specimen as shown in **Figure 4-4**. This was selected considering this near the grip was not strained during tensile test, as confirmed by DIC observations. The test load for indentation was 4.9N, with a pitch of 0.5mm between indents. Additionally, microscopic observation was performed to confirm microstructure with optical microscopy, then IGF volume fraction was measured by the point counting method using five pictures taken at the center width direction in the specimens for the as-deposited weld metals, where the IGF was defined as acicular ferrite, intragranular Widmanstätten ferrite, polygonal ferrite, and Bainitic ferrite in accordance of the definitions introduced by Thewlis [7]. Furthermore, the fracture surface of each specimen after tensile test were investigated by Scanning Electron Microscopy (SEM). Finally, thermal desorption analysis was conducted in order to check the amount of trapped (non-diffusible) hydrogen absorption in the specimens. This was analyzed using a IonScience Hydrosteel 6000 as a machine for thermal desorption analysis, in which the temperature ramp was 6°C /minute up to 800°C, and then was held at 800°C for up to 200 minutes.
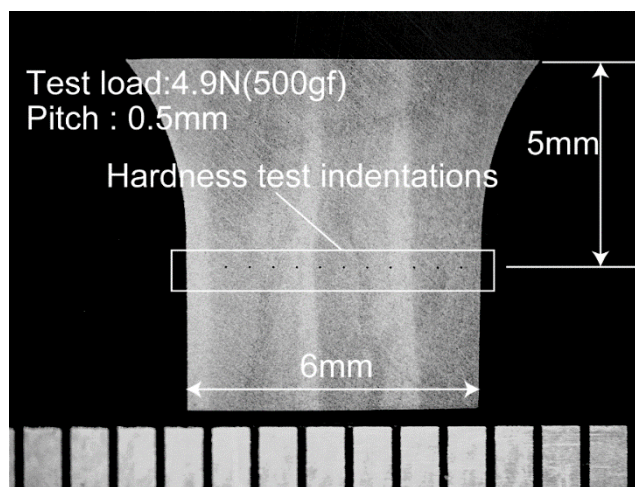
Figure 4-4 Hardness testing positions

4.3 Results

The summary of the tensile test results is shown in **Table 4-2**, and the engineering stress – engineering strain curves obtained for both welded joints are shown in **Figure 4-5**. The 0.2% proof stress and ultimate tensile stress for the AA-50 series weld metal were higher, and the elongation and the area reduction were lower compared with A-30 series weld metal. Also, it can be noted that the 0.2 % proof stress and ultimate tensile strength for A-30 series increased as the severity of hydrogen charging increased; however, the behaviour of the AA-50 series weld metal remained more stable, and actually exhibited a slight decrease in proof stress and tensile stress with increased hydrogen charging. The elongations for both weld metals deteriorated with hydrogen charging, although the A-30 series weld metal decreased more significantly than AA-50 series weld metals. Furthermore, the maximum local strain just before fracture, which was measured by DIC decreased more drastically for the A-30 series weld metal with hydrogen charging compared to the A-50 series. Hardness test results are summarized in **Table 4-3**, with the maximum, minimum, mean, and standard deviation values shown. The average hardness values observed in AA-50 series were higher compared with the A-30 series, and the values were negligibly changed due to the hydrogen charging in the AA-50 weld metal. The indentation results are consistent with the tensile test results based on the average values for the weld metals and response to hydrogen charging.

Table 4-2 Result of tensile tests

Welding joint name	Specimen ID	Hydrogen charging condition	0.2% proof stress (MPa)	Tensile stress (MPa)	Elongation (%)	Area reduction (%)	Maximum local strain (%)
A-30	A-30-N	Non-charged	647	729	9.6	29	49.58
	A-30-CA	Charged (21mA/cm^2, 4 days)	697	768	9.1	25	49.26
	A-30-CB	Charged (42mA/cm^2, 6 days)	736	805	8.2	20	37.63
AA-50	A-30-N	Non-charged	765	853	8.7	25	46.20
	A-30-CB	Charged (42mA/cm^2, 6 days)	749	844	8.2	24	46.47
	A-30-CC	Charged (84mA/cm^2, 6 days)	730	824	8.1	23	47.15

*0.1M NaOH was used as hydrogen charging solution
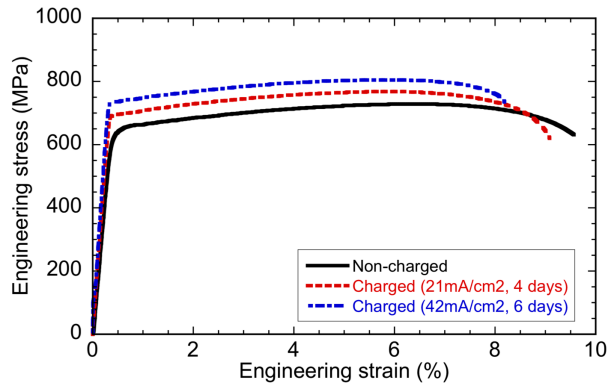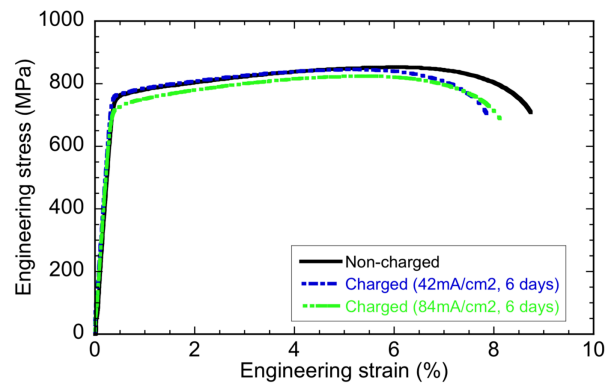
(a) A-30 series　　　　　　　(b) AA-50 series

Figure 4-5 Comparison of stress-strain curves for A-30 series and AA-50 series

Table 4-3 Hardness test results

Specimen ID	Hydrogen charging condition	Hardness Hv$_{4.9N}$			
		Maximum	Minimum	Mean	Standard Deviation
A-30-N	Non-charged	286	270	277	5.7
A-30-CA	Charged (21mA/cm^2, 4 days)	-	-	-	-
A-30-CB	Charged (42mA/cm^2, 6 days)	310	277	290	8.7
AA-50-N	Non-charged	311	278	293	10.1
AA-50-CB	Charged (42mA/cm^2, 6 days)	315	287	298	7.4
AA-50-CC	Charged (84mA/cm^2, 6 days)	320	290	306	9.7

-: No data

It is widely accepted that steel microstructures with a higher hardness are expected to have higher hydrogen susceptibility; however, the experimental results indicate the opposite trend. A comparison of the microstructures in the weld metals for both specimen series is given in **Figure 4-6**. A microstructure dominated by very fine intragranular ferrite (IGF) can be found in both weld metals, where it should be noted that a higher fraction of grain boundary ferrite (GBF) was found in the A-30 series weld metal. Comparison of fracture surfaces for both specimens observed by SEM are shown in **Figure 4-7**, where evidence of ductile features containing fibrous dimples can be found in all locations. The mean sizes of the dimples were measured with point counting methods by projecting vertical, horizontal, and diagonal lines on the SEM images (taken at 7000x magnification), and counting the intersection points of the dimple edges, such that the dimple edge intercepts could be quantified in the SEM images. The measurement results are summarized in **Table 4-4**. The quantified dimple sizes were: 2.2 μm for A-30-N, 2.1 μm for A-30-CB, 1.9 μm for AA-50-N, and 1.8 μm for AA-50-CB. Although dimple size for the AA-50 series tend to be smaller compared with the A-30 series weld metal, it is difficult to conclude that there are any trends derived from hydrogen charging.
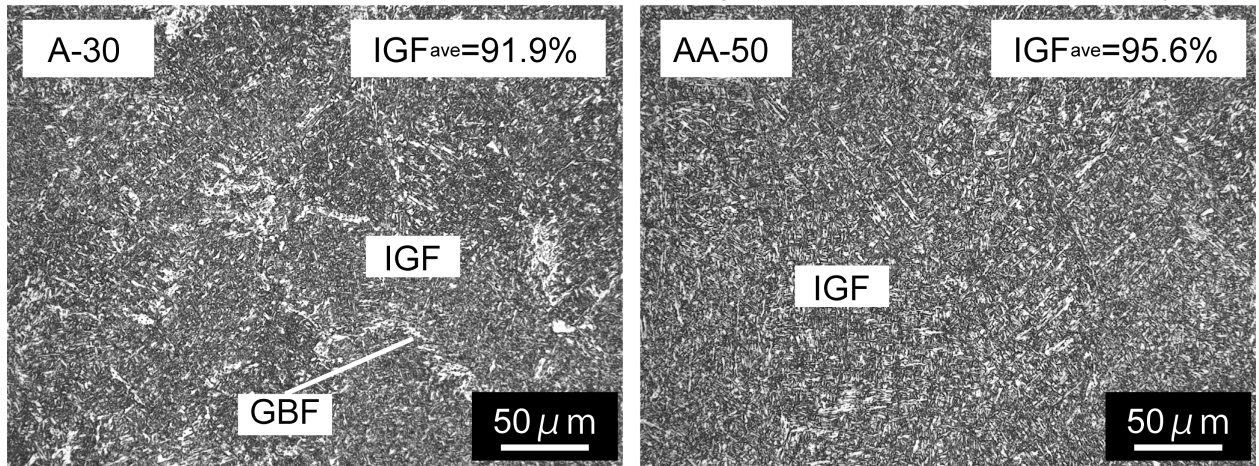
Figure 4-6 Comparison of microstructures in A-30 and AA-50 series weld metals
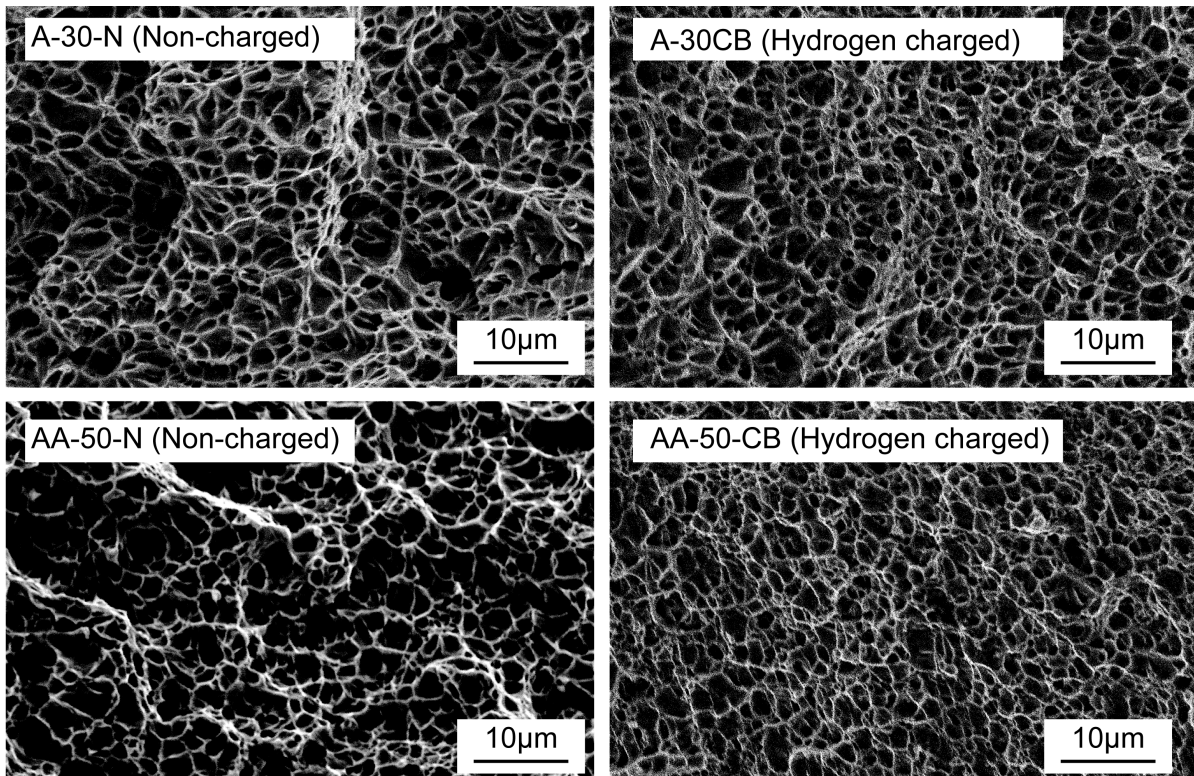
Figure 4-7 Comparison of fracture surfaces observed in A-30 and AA-50 weld metals after tensile

testing

Table 4-4 Results of dimple size measurement for fracture surfaces following tensile tests

| Specimen ID | Hydrogen charging condition | Dimple size (μm) | |
		Mean	Standard Deviation
A-30-N	Non-charged	2.23	0.27
A-30-CB	Charged (42mA/cm^2, 6 days	2.10	0.21
AA-50-N	Non-charged	1.85	0.30
AA-50-CB	Charged (42mA/cm^2, 6 days)	1.80	0.19

Thermal desorption analysis was carried out in order to quantify the fraction of trapped hydrogen in the weld metals after hydrogen charging. The relationship between temperature and measured hydrogen, evaluated from thermal desorption is demonstrated in **Figure 4-8**. Here the first portion of the x-axis represents the temperature during the linear heating stage at 6º/minute up to 800ºC, and then the second half of the axis shows the desorption during the 200 min holding time. The tests were conducted for the weld metals before and after hydrogen charging at 42mA/cm^2 for 6 days, corresponding to samples A-30-N, A-30-CB, and AA-50-CB. The specimens A-30-N and AA-50-CB indicate no peak around 500°C, although the A-30-CB specimen exhibits a peak at that temperature. Furthermore, the measured hydrogen for A-30-N and AA-50-CB continued to be released at 800°C for over 100 minutes in both cases.
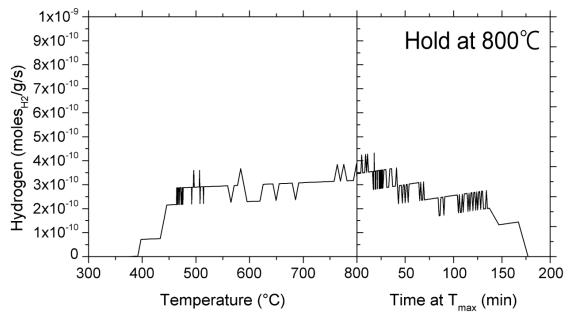
(a) A-30-N(Non-charged)
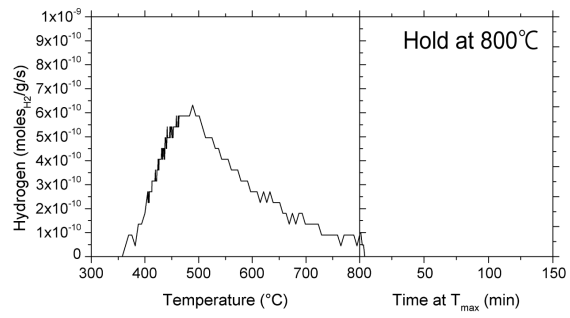
(b) A-30-CB(Hydrogen-charged)
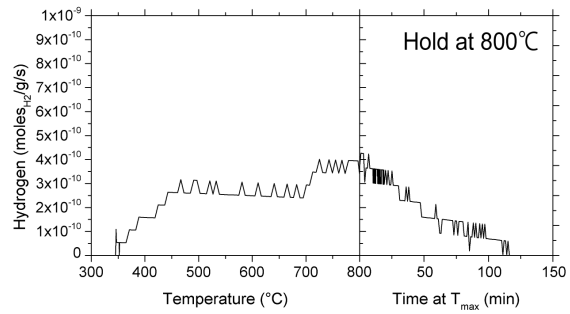
(c) AA-50-CB(Hydrogen-charged)

Figure 4-8 Thermal desorption analysis results, indicating hydrogen release during heating up at

6°C/min up to 800°C, followed by isothermal desorption at 800°C for up to 200 min

4.4 Discussions

The AA-50 weld metals exhibited a higher 0.2% proof stress, tensile stress, hardness, along with a lower elongation compared with the A-30 series. This indicates that the AA-50 series weld metals are composed of a microstructure which offers slightly increased strength, and this is consistent with the higher IGF volume fraction observed. This microconstituent is derived from a much higher and optimized ratio of titanium and oxygen, which promotes the nucleation of IGF (acicular ferrite) microstructure within the austenite grains during cooling from high temperature as mentioned in Chapter 2. The IGF volume fraction for the AA-50 series were much higher than the A-30 series as illustrated in **Figure 4-6**. As shown in **Figure 4-5**, both weld metals exhibited elongation values that decreased when hydrogen charging was applied. It is well known, that tensile elongation to fracture will typically decrease when hydrogen is present in the steel [91, 93-94], thus the results obtained here support this general tendency. The 0.2% proof stress and tensile strength of the A-30 series welds, however, revealed the tendency for hydrogen charging to stimulate an increase in strength in this weld metal, whereas those properties did not change for the AA-50 series weld metal after charging. According to some recent research on high carbon steels and stainless steels, it has been suggested that the 0.2% proof stress is not influenced by hydrogen charging [91, 93-94]. This contradicts the behaviour of the A-30 series weld metals, although it should be noted that the present weld metals are not high carbon steels. One may still question how to account for the increase the in strength in the AA-30 material when hydrogen is introduced. According to Zhao et al., a large fraction of nano-sized carbide precipitates such as TiC, VC, and NbC are present in the IGF structures of steel with high acicular ferrite content, and these can prevent dislocation motion by pinning [49]. The TEM micrograph of the IGF in the AA-50 weld metal reveals similar microstructures containing acicular ferrite as shown in **Figure 4-9**. Here one can note that there are many nano-carbides as

reported by Zhao et al. [51]. These nano-carbide interactions contribute significantly to the strengthening of the steel, while work-hardening and dislocation strengthening plays a lesser role.

It is well known that diffusible hydrogen can be trapped by dislocations [93], and then as these dislocations move during deformation, the hydrogen may be carried along with the moving dislocations. Considering that A-30 series involves a lower number of nano-scale carbide precipitates due to the lower fraction IGF, dislocation activity will play an increased role in strengthening versus the AA-50 weld metal. Thus, dislocation trapping hydrogen will have an increased influence on the microstructure. In other words, hydrogen will diffuse in the weld metals, which may also lead to increased drag on the dislocations and higher stress required to move them. Further details regarding the dislocation activity and work hardening in the A-30 series weld metal following hydrogen charging in order to clarify this mechanism should be investigated.
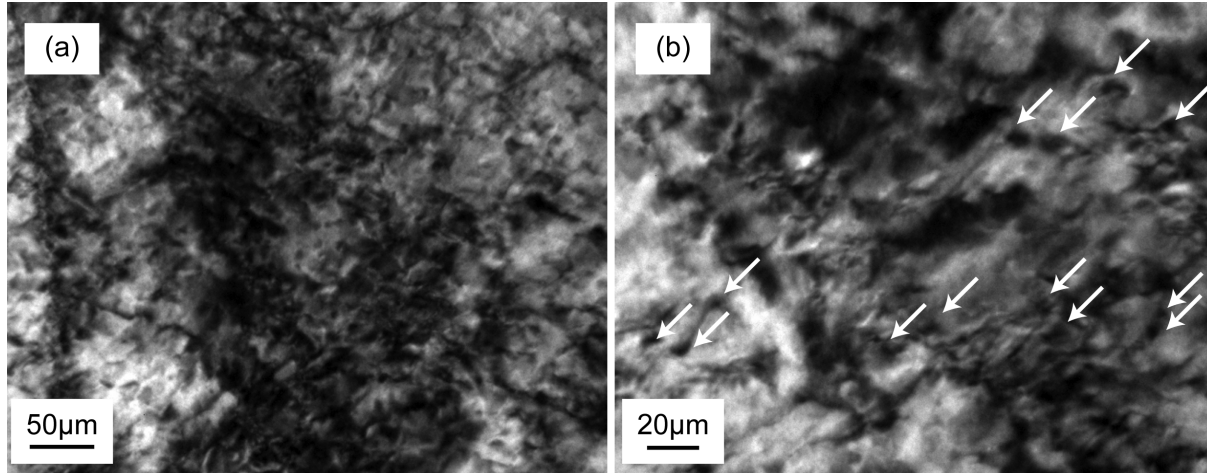
Figure 4-9 Nano-side carbides in IGF (acicular ferrite microstructure) for AA-50 series (a) Low magnification photo, (b) High magnification photo, allows indicate nano-sized carbides

Based on the thermal desorption observed in **Figure 4-8**, the A-30-CN weld metal exhibited a peak around 500°C; however, the AA-50-CN weld metal did not exhibit a peak at the same temperature, but instead the measured desorbed hydrogen continued to evolve beyond 700 °C. According to Beidokhti et al., the peaks observed at 235°C, 355°C, 492°C, and approximately 700°C correspond to hydrogen released from dislocations, microvoids, MnS inclusion, and Ti(C, N), respectively [95]. In addition, these authors showed that the peak temperature correlates with activation energy to release the hydrogen [95]. In other words, a high desorption peak temperature indicates a strong hydrogen trapping site. They also mention that the crystal structure of titanium compounds and their interface with acicular ferrite act as hydrogen trapping sites with a potentially higher capacity than other grain boundaries or other nucleation particles based on MnS, or TiC particles present in the structure [95].

Recently, investigating the mechanism for hydrogen trapping has been performed with atom probe tomography by other researchers [94,96], which can analyze a structure at the atomic level. For example, the investigation of hydrogen trapping sites in ANSI 4040 steel (0.38% carbon steel) using atom probe tomography conducted by Jiang et al., indicated that hydrogen atoms are mainly trapped at the carbide/ferrite interfaces [94]. Also, Takahashi et al. investigated hydrogen trapping in a vanadium alloyed steel, and revealed that hydrogen is trapped at interfaces between VC precipitates and ferrite [96]. From these works, it appears that the interface of carbide/ferrite acts as a strong hydrogen trapping site. Thus, it should be anticipated that if there is a higher fraction of these high energy trapping sites around acicular ferrite and titanium particles, a lower fraction of the total hydrogen will be available for the lower activation sites, such as dislocations. This would account for the observed behaviour in which the yield strength is not significantly affected by hydrogen in the AA-50 series weld metals. On the other hand, since the A-30 series weld metal contains negligible titanium and less acicular ferrite, there will be more hydrogen available to be trapped at dislocations.

93

Therefore, this may explain the increase in yield strength post-charging for the A-30 series weld metal.

The fracture surfaces for both specimens after tensile test observed by SEM and the resulting chemical analysis for precipitate measured by Energy Dispersive X-ray Spectroscopy are shown in **Figure 4-10**. The results show that precipitates in the A-30 weld metal were predominantly Fe-O compounds; on the other hand, precipitates observed in the AA-50 series weld metal were rich in Ti as well as Fe, and O. From the results noted for the AA-50 weld metal, it is expected that these titanium bearing particles are TiC and Ti-O precipitates, since the interaction volume of the beam will indicate increase the detected Fe, and the SEM-EDS system cannot reliably detect carbon. Also, it is expected that the AA-50 weld metals contain a large number of titanium oxides which are a strong hydrogen trapping site due to the higher titanium and oxygen content; however, the A-30 weld metals do not expect to contain these titanium particles due to lower titanium content. Hence, this can support the notion that the A-30 series weld metal will have a higher hydrogen susceptibility due to the lack of strong trapping sites.

(a) A-30   (b) AA-50
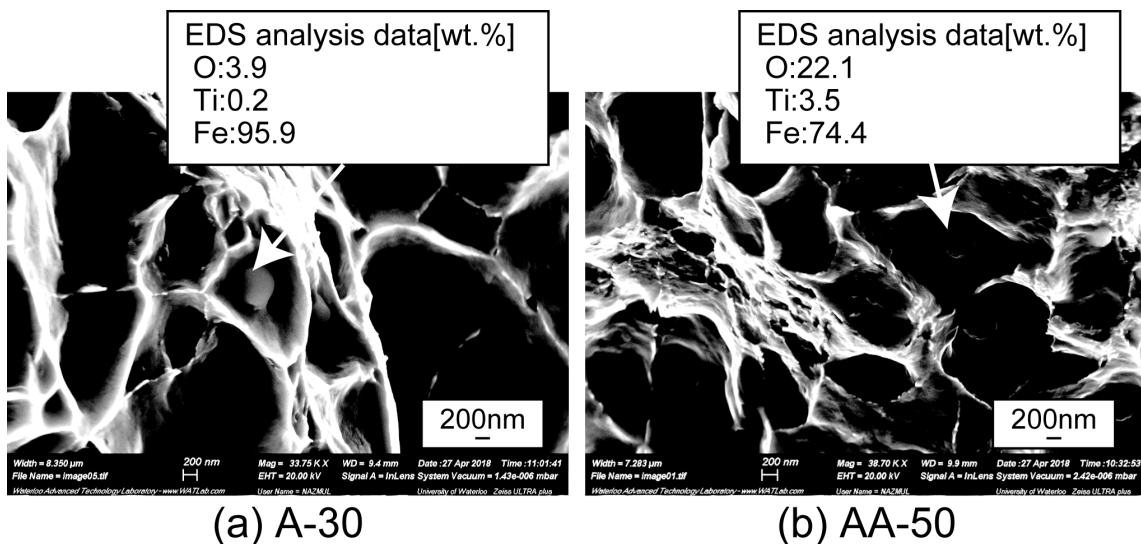
Figure 4-10 Analysis results with Energy dispersive X-ray Spectroscopy of Ti compounds on those fracture surface by tensile test

4.5 Summary

In this chapter, the differences in mechanical properties observed between two weld metals with slightly differences in titanium and oxygen content were investigated in terms of the IGF volume fraction and response to hydrogen charging. The two weld joints exhibited differences in hardness and tensile behaviour after hydrogen charging, and the following new knowledge was derived:

1) A microstructure which contains a higher fraction of intergranular ferrite produced when more titanium and oxygen are included in the weld metal will have lower susceptibility to hydrogen. The AA-50 series weld metal containing titanium and 95.6% IGF volume fraction revealed stable strength, ductility, and hardness after charging compared to the weld metal containing 91.9 % IGF.

2) The hydrogen desorption and TEM analysis AA-50 weld metal series which contain much titanium oxides and carbo-nitrides lead to lower hydrogen susceptibility than A-30 series. This indicates that titanium compounds act as strong hydrogen trapping sites.

Based on the results mentioned above, it can be stated that the strategy to suppress the detrimental effects of hydrogen on mechanical properties is more dependent on the constituent microstructures and distribution of nano-scale precipitates rather than solely on the hardness value. This is a vital observation that can be used to further refine standards and practices for avoiding sulphide stress cracking and potentially other hydrogen induced cracking mechanisms in high strength steels.

Chapter 5
Conclusions

5.1 Conclusions

The present research provided a methodology of maximizing intragranular ferrite which offers finer microstructures in steel weld metal, and a detailed investigation of the influence of microconstituents on sulphide stress cracking susceptibility, which is a form of hydrogen embrittlement. The main findings were observed as follows: The most effective balance between titanium and oxygen contents in order to maximize intragranular ferrite volume fraction correspond to the ideal stoichiometry of Ti_2O_3 since this becomes a core of intragranular nucleation. Next weld metals involving large fraction of intragranular ferrite (exceeding 95%) survived sulphide stress cracking test in accordance with NACE MR0175/ISO 15156 (test solution) and European Federation of Corrosion publication number 16 (based on the 3 and 4 point bending method). Additionally, the use of combined SEM microscopy with hydrogen microprinting revealed the hydrogen trap mechanism in microstructures, in particular the case of an intragranular ferrite microstructures in high strength steel GMA weld metal. The use of electrolytic hydrogen charging followed by mechanical testing showed that weld metals which contain more than 8.1% grain boundary ferrite (while remaining 91.9% is intragranular ferrite) are more easily affected by hydrogen, such that their strength increases at the expense of ductility.

In the first finding, various weld joints with differing intragranular ferrite volume fraction were produced, and a relationship between the balance of titanium and oxygen was shown to be well correlated with intragranular ferrite fraction. It was proposed that the most effective balance between titanium and oxygen contents to maximize intragranular ferrite fraction corresponds to the ideal stoichiometry of Ti_2O_3, as discussed in Chapter 2. It was then shown that these weld metals with higher intragranular ferrite fraction performed better during sulphide stress cracking tests in accordance with NACE MR0175/ISO 15156 (test solution) and European Federation of Corrosion

publication number 16 (based on the 3 and 4 point bending method). This indicated that the key microstructure to increase SSC resistance is intragranular ferrite, and that a critical hardness value of 250 Hv is not necessarily imperative, as has otherwise been a long time consensus.

Next, hydrogen trapping sites were visualized by combining both SEM microscopy, hydrogen microprint technique and Electron Backscattered Diffraction. It was revealed that grain boundaries act as hydrogen trapping sites. Additionally, it was found that many micro and nano-scale carbides can potentially act to prevent the motion of dislocations which can carry diffusible hydrogen in intragranular ferrite. Furthermore, intragranular ferrite offers higher toughness due to a finer grain size, which also contains higher fractions of high angle grain boundaries. Hence, based on these results reasons, intragranular ferrite decreases the susceptibility to sulphide stress cracking and hydrogen embrittlement.

Finally, in order to investigate the effect of role of intragranular ferrite volume fraction on hydrogen susceptibility and mechanical properties in hydrogen charged steels, the tensile behavior before and after hydrogen charging with electrical charging was compared. Hydrogen charging had less effect on the stress-strain curves for weld metals involving a higher intragranular ferrite volume fraction than on one having slightly few intragranular volume fraction. In order to reveal hydrogen trapping ability of both weld metals, thermal desorption analysis was performed. The results showed that in the case of low intragranular ferrite volume fraction, hydrogen was present in a diffusible condition because of low releasing temperature. In contrast, in the case of high intragranular ferrite volume fraction, hydrogen releasing temperature was high, which suggests that hydrogen was trapped in a non-diffusible condition.

Based on these findings, the following recommendations can be made in order to improve the reliability of weld metals used for joining linepipe used in sour gas applications:

[1]   Establish a method to control acicular ferrite volume fraction in the weld metals

97

[2] Evaluate the relationship between kinds of microstructures and SSC susceptibility for GMA weld metals and validate a critical hardness value

[3] Investigate the role of microstructures and establish minimum acicular ferrite content values to provide SSC resistance

In conclusion, this research proposes that intragranular ferrite acts to reduce hydrogen embrittlement susceptibility, thus improving SSC resistance. Furthermore, the intragranular ferrite fraction is a dominant factor in determining the resistance to this cracking mechanism in these high strength steel weld metals and, thus, is more important than the purely the mechanical properties.

5.2 Future work

As future work, some follow-up studies and action plans may be proposed. First of all, there are controversial notions about acicular ferrite nucleation as described in Chapter 2. This paper supports manganese depletion zone theory from the result of finding manganese depletion zone around a core of intragranular nucleation site, and this is worth validating further. However, many intragranular ferrite cores could not be confirmed due to higher analyzing cost for extraction with focused ion beam and TEM observation. In the future, in order to increase accuracy, it is expected that large number of analysis will be conducted. On the other hand, recently, analyzing methods with higher resolution have been developed, for example atom probe tomography, which can analyze the position of an atom in an intragranular ferrite core at the atomic level. Due to the intragranular ferrite core size, conducting these studies is difficult; however, it is expected that revealing structure of intragranular ferrite core with the atom probe tomography will be possible in the near future.

Next, this thesis suggests the best balance of titanium and oxygen in weld metals to maximize intragranular ferrite in Chapter 2; however, the present study is limited to the case of low heat input condition, typical of gas metal arc welding for pipeline construction. Maximizing intragranular ferrite is required for most of welding applying thicker steels to achieve higher fracture toughness. As the future work, it is hopeful that investigation in terms of influence of heat input and welding methods on intragranular ferrite volume fraction will be performed.

Furthermore, this thesis indicates that intragranular ferrite increase SSC resistance and low susceptibility of tensile behavior due to dispersion of hydrogen trapping sites, pinning effect by nano-carbide precipitates, trapping hydrogen as diffusible condition. However, this thesis has not revealed quantitively the SSC susceptibility although welding joints involving much intragranular ferrite can pass SSC test. It is expected that a monitoring method for specimen condition into a chamber filled by hydrogen sulphide saturated solution will be developed, standardized, conducting quantitative

investigation for SSC susceptibility. Moreover, this paper indicates increasing hardness values by hydrogen charging especially welded metals having low intragranular volume fraction. This mechanism and cause have not been revealed perfectly. As the future work, it will be expected that the relationship between hydrogen charging and hardness would be confirmed.

Finally, as mentioned in Chapter 1, hardness guideline to avoid SSC initiation, which is standardized by NACE standard MR0175/ISO 15156 [2] and EFC publication No.16 [3] had determined based on large number of tests by many researchers. It is hoped that a large number of tests will be performed by many researchers, and the following discussion will resolve this hardness guideline in order to allow high grade linepipes to be utilized widely for natural gas transportation.

Bibliography

[1] Omura, T., Mumata, T., Takayama, T., Arai, Y., Souma, A., Ohe, T., Amaya, H., & Ueda, M., 2015), Super-high Strength Low Alloy Steel OCTG with Improved Sour Resistance, Nippon Steel & Sumitomo Metals Technical Report, No.107, pp.18-23

[2] NACE MR0175/ISO 15156 Petroleum and natural gas industries –Materials for use in H2S– containing environments in oil and gas production-containing environment

[3] European Federation of Corrosion publication number 16 –Guidelines on Materials Requirement for Carbon and Low Alloy Steels for H_2S -Containing Environments in Oil and Gas Production-

[4] Bauman, J., 2010, NACE MR0175/ISO15156 Interpretation and application, Northern area western conference, Calgary, Alberta, Canada, Feb 15-18.

[5] Patrick, D. H., 1999, MR0175-A history and development study, CORROSION 1999, NACE International.

[6] Treseder, R. S., & T. M. Swanson, T.M., 1968, Factors in sulphide corrosion cracking of high strength steels, Corrosion 24 (2), pp. 31-37.

[7] Thewlis, G., 2004, Classification and quantification of microstructures in steels, Materials Science and technology, 20(2), 143-160.

[8] Lan, L., Qiu, C., Zhao, D., Gao, X., & Du, L., 2012, Analysis of martensite–austenite constituent and its effect on toughness in submerged arc welded joint of low carbon bainitic steel. Journal of Materials Science, 47(11), 4732-4742.

[9] Abdelbaset.R. H. M., 2018, Evaluation of Mechanical Properties in Pipeline Girth Welds Using Instrumented Indentation, PhD thesis, University of Waterloo.

[10] Pickering, F. B., 1983, The Spectrum of Microalloyed High-Strength Low-Alloy Steels, HSLA Steels, Technology and Applications, 1-31.

[11] Anaraki, K. P., 2005, Microstructure and Property Examination of the Weld HAZ in Grade 100 Microalloyed Steel, PhD thesis, University of Alberta, 2005

[12] Surian, E., Trotti, J., Cassanelli, A., & De Vedia, L., 1994, Influence of chromium on the mechanical properties and microstructure of weld metal from a high-strength SMA electrode, WELDING JOURNAL -NEW YORK-, 73, 45-s.

[13] Lambot, S., Slob, E. C., van den Bosch, I., Stockbroeckx, B., & Vanclooster, M., 2004, Modeling of ground-penetrating radar for accurate characterization of subsurface electric properties, IEEE transactions on geoscience and remote sensing, 42(11), 2555-2568.

[14] Potapov, N. N., 1993, Oxygen effect on low-alloy steel weld metal properties, Welding Research Supplement, pp367-370.

[15] Zhang, Z., & Farrar, R. A., 1997, Influence of Mn and Ni on the microstructure and toughness of C-Mn-Ni weld metals, Welding Journal, 76(5), pp183.

[16] Tanaka, M., Tashiro, S., Satoh, T., Murphy, A. B., & Lowke, J. J., 2008, Influence of shielding gas composition on arc properties in TIG welding. Science and technology of welding and joining, 13(3), pp225-231.

[17] Davis, J. R., 2001, Alloying: understanding the basics, ASM international.

[18] El-Kashif, E., & Koseki, T., 2011, Effect of niobium on HAZ toughness of HSLA steels, Alloy steel-properties and use, ed. by Morales EV, pp87-108.

[19] Fletcher, L., Zhu, Z., Murudgananth, M., Zheng, L., Bai, M., Li, H., & Barbaro, F., 2011, Effect of Ti and N concentrations on microstructure and mechanical properties of microalloyed high strength line pipe steel welds.

[20] Zhang, Y. Q., Zhang, H. Q., Li, J. F., & Liu, W. M., 2009, Effect of heat input on microstructure and toughness of coarse grain heat affected zone in Nb microalloyed HSLA steels, Journal of Iron and Steel Research International, 16(5), pp73-80.

[21] Fattahi, M., Nabhani, N., Hosseini, M., Arabian, N., & Rahimi, E., 2013, Effect of Ti-containing inclusions on the nucleation of acicular ferrite and mechanical properties of multipass weld metals, Micron, 45, pp107-114.

[22] Lu, J., 2009, Quantitative microstructural characterization of microalloyed steels, PhD thesis, University of Alberta

[23] Baker, T. N., 2016, Microalloyed steels. Ironmaking & Steelmaking, 43(4), pp264-307.

[24] Junhua, K., Lin, Z., Bin, G., Pinghe, L., Aihua, W., & Changsheng, X., 2004, Influence of Mo content on microstructure and mechanical properties of high strength pipeline steel, Materials & Design, 25(8), pp723-728.

[25] Mohrbacher, H., 2010, Principal effects of Mo in HSLA steels and cross effects with microalloying elements. Central Iron and Steel Research Institute (CISRI), pp75-96.

[26] Bakkaloglu, A., 2002, Effect of processing parameters on the microstructure and properties of an Nb microalloyed steel, Materials letters, 56(3), 200-209.

[27] Sung, H. K., Sohn, S. S., Shin, S. Y., Oh, K. S., & Lee, S., 2014, Effects of oxides on tensile and Charpy impact properties and fracture toughness in heat affected zones of oxide-containing API X80 linepipe steels, Metallurgical and Materials Transactions A, 45(7), pp3036-3050.

[28] Sindo, K., Welding Metallurgy, 2003, volume 1. John Wiley & Sons Inc., New York, second edition

[29] Pargeter, R. J., 2007, Susceptibility to SOHIC for Linepipe/Pressure Vessel Steels, *Paper presented at NACE*, *11*(17).

[30] Yapp, D., and Blackman, S. A., 2004, Recent developments in high productivity pipeline welding, Journal of the Brazilian Society of Mechanical Sciences and Engineering 26(1), pp. 89-97.

[31] Hosoda, H., Ikuno, Y., Hakoda, T., Kimura, F., 2008, Automatic Welding System Characterized by High Speed Torch Oscillation and Hydraulic Clamp for Offshore Pipelines, 8th International Welding Symposium, Kyoto, Japan.

[32] Kisaka. Y., Kimura, F., Hakoda, T., Hosoda, H., & Torii, T., 2013, "A development of high-speed GMA girth welding system for pipelines." Canweld conference 2013, Niagarafalls, Ontario, Canada.

[33] Lee, C. H., & Chang, K. H., 2008, Three-dimensional finite element simulation of residual stresses in circumferential welds of steel pipe including pipe diameter effects. *Materials Science and Engineering: A*, *487*(1-2), 210-218.

[34] Elboujdaini, M., Sastri, V.S., and Perumareddi. J.R., 2006, Studies on inhibition of hydrogen-induced cracking of linepipe steels, Corrosion 62 (1), pp29-34.

[35] Shinozaki, J., Muto, I., Omura, T., Numata, M., & Hara, N., 2011, Local dissolution of MnS inclusion and microstructural distribution of absorbed hydrogen in carbon steel, Journal of The Electrochemical Society 158.(9), pp302-309.

[36] Kermani, B., Boucher, C., Crolet, J. L., Enerhaug, J., Fassina, P., Howard, R., ... & Linne, C., 2000, Limits of linepipe weld hardness for domains of sour service in oil and gas production, CORROSION 2000. NACE International.

[37] Omweg, G. M., Frankel, G. S., Bruce, W. A., Ramirez, J. E., & Koch, G., 2003, Performance of welded high-strength low-alloy steels in sour environments, Corrosion 59 (7), pp640-653.

[38] Timmins. P. F., 1997, Solutions to Hydrogen Attack in Steels, ASM international, Chap.3, pp94.

[39] Al-Mansour, M., Alfantazi, A. M., and El-Boujdaini, M., 2009, Sulphide stress cracking resistance of API-X100 high strength low alloy steel, Materials & Design 30(10), pp4088-4094.

[40] Asahi, H., and Ueno, M., 1992, Effect of austenite grain size on sulphide stress cracking resistance of low alloy martensitic steels, ISIJ international 32(9), pp1021-1026.

[41] Takasawa, K., Wada, Y., Ishigaki, R., & Kayano, R., 2010, Effects of grain size on hydrogen environment embrittlement of high strength low alloy steel in 45 MPa gaseous hydrogen, Materials transactions 51(2), pp347-353.

[42] Ichimura, M., Sasajima, Y., and Imabayashi, M., 1991, Grain boundary effect on diffusion of hydrogen in pure aluminum, Materials Transactions, JIM 32(12), pp1109-1114.

[43] Yazdipour, N., Dunne, D. P., and Pereloma, E.V., 2012, Effect of Grain Size on the Hydrogen Diffusion Process in Steel Using Cellular Automaton Approach, Materials Science Forum. 706.

[44] Fairchild, D. P., Macia, M. L., Bangaru, N. V., & Koo, J. Y., 2004, Girth welding development for X120 linepipe, International Journal of Offshore and Polar Engineering 14. JAN.

[45] Motohashi, H., Hagiwara, N., and Masuda, T., 2005, Tensile properties and microstructure of weld metal in MAG welded X80 pipeline steel, Welding international 19(2), pp100-108.

[46] Park, G. T., Koh, S. U., Jung, H. G., & Kim, K. Y., 2008, Effect of microstructure on the hydrogen trapping efficiency and hydrogen induced cracking of linepipe steel, Corrosion science 50(7), pp1865-1871.

[47] Koh, S. U., Jung, H. G., Kang, K. B., Park, G. T., & Kim, K. Y., 2008, "Effect of microstructure on hydrogen-induced cracking of linepipe steels." Corrosion 64(7), pp. 574-585.

[48] Zhao, M. C., Liu, M., Atrens, A., Shan, Y. Y., & Yang, K., 2008, Effect of applied stress and microstructure on sulphide stress cracking resistance of pipeline steels subject to hydrogen sulphide, Materials Science and Engineering: A 478(1), pp43-47.

[49] Zhao, M. C., and Yang. K., 2005, Strengthening and improvement of sulphide stress cracking resistance in acicular ferrite pipeline steels by nano-sized carbonitrides, Scripta materialia 52(9), pp881-886.

[50] Zhao, M. C., Shan, Y. Y., Xiao, F. R., Yang, K., & Li, Y. H., 2002, Investigation on the H 2 S-resistant behaviors of acicular ferrite and ultrafine ferrite, Materials Letters 57(1), pp141-145.

[51] Zhao, M. C., Tang, B., Shan, Y. Y., & Yang, K., 2003, Role of microstructure on sulphide stress cracking of oil and gas pipeline steels, Metallurgical and Materials Transactions A 34(5), pp1089-1096.

[52] Koseki, T., 2005, A Review on Inclusion-Assisted Microstructure Control in C-Mn and Low-Alloy Steel Welds, Welding in the World, 49(5-6), pp22-28.

[53] Beidokhti, B., Dolati, A., and Koukabi, A. H., 2009, Effects of alloying elements and microstructure on the susceptibility of the welded HSLA steel to hydrogen-induced cracking and sulphide stress cracking, Materials Science and Engineering: A 507(1), pp167-173.

[54] Kasuya, T., Kobayashi, J., Ohkita, S., & Fuji, M., 1998, Sulphide stress cracking of heat affected submerged arc weld metals, Science and Technology of Welding & Joining 3(1), pp25-32.

[55] Wang, S. H., Luu, W. C., Ho, K. F., & Wu, J. K., 2003, Hydrogen permeation in a submerged arc weldment of TMCP steel, Materials Chemistry and Physics 77(2), pp447-454.

[56] Ovejero-García, J., 1985, Hydrogen microprint technique in the study of hydrogen in steels, Journal of Materials Science, 20(7), pp2623-2629.

[57] Takada, A., Terasaki, H., & Komizo, Y., 2013, Effect of aluminium content on acicular ferrite formation in low carbon steel weld metals, Science and Technology of Welding and Joining, 18(2), pp91-97.

[58] Takada, A., Terasaki, H., & Komizo, Y. I., 2014, Effect of Boron Distribution on the Phase Transformation Behavior of Low Carbon Steel Weld Metal, Transactions of JWRI, 43(2), pp27-30.

[59] Takada, A., Komizo, Y. I., Terasaki, H., Yokota, T., Oi, K., & Yasuda, K., 2015, Crystallographic analysis for acicular ferrite formation in low carbon steel weld metals, Welding International, 29(4), pp254-261.

[60] Terasaki, H., Yamada, T., & Komizo, Y. I., 2008, Analysis of Inclusion Core under the Weld Pool of High Strength and Low Alloy Steel, ISIJ international, 48(12), pp1752-1757.

[61] Yamada, T., Terasaki, H., & Komizo, Y., 2008, Microscopic observation of inclusions contributing to formation of acicular ferrite in steel weld metal, Science and Technology of Welding & Joining, 13(2), pp118-125.

[62] Yamada, T., Terasaki, H., & Komizo, Y. I., 2009, Analytical Investigation of Inclusions Related to Acicular Ferrite Formation in Steel Weld Metal, Transactions of the Materials Research Society of Japan, 34(2), pp241-244.

[63] Yamada, T., Terasaki, H., & Komizo, Y., 2009, Microstructural evolution in low carbon steel Ti–B weld metals with several Al levels, Welding International, 23(5), pp376-381.

[64] Yamada, T., Terasaki, H., & Komizo, Y. I., 2009, Relation between inclusion surface and acicular ferrite in low carbon low alloy steel weld, ISIJ international, 49(7), pp1059-1062.

[65] Komizo, Y. I., Terasaki, H., & Yamada, T. , 2008, January, Morphological Development for Acicular Ferrite in High Strength Pipeline Steel Weld Metal., 7th International Pipeline Conference, American Society of Mechanical Engineers, pp.483-487

[66] Aihara, S., Shigesato, G., Sugiyama, M., Uemori, R., 2004, Microstructural control of weld heat-affected zone of steel by Mn depletion around inclusions, Nippon Steel technical Report, pp39-44.

[67] Seo, J. S., Lee, C., & Kim, H. J., 2013, Influence of oxygen content on microstructure and inclusion characteristics of bainitic weld metals, ISIJ international, 53(2), pp279-285.

[68] Seo, K., Kim, Y. M., Evans, G. M., Kim, H. J., & Lee, C., 2015, Formation of Mn-depleted zone in Ti-containing weld metals, Welding in the World, 59(3), pp373-380.

[69] Seo, J. S., Kim, H. J., & Lee, C., 2013, Effect of Ti addition on weld microstructure and inclusion characteristics of bainitic GMA welds. ISIJ international, 53(5), pp880-886.

[70] Seo, J. S., Seo, K., Kim, H. J., & Lee, C., 2014, Effect of titanium content on weld microstructure and mechanical properties of bainitic GMA welds, Welding in the World, 58(6), pp893-901.

[71] Yamamoto, K., Hasegawa, T., & Takamura, J. I., 1996, Effect of Boron on Intra-granular Ferrite Formation in Ti-Oxide Bearing Steels, ISIJ international, 36(1), pp80-86.

[72] Shim, J. H., Cho, Y. W., Chung, S. H., Shim, J. D., & Lee, D. N., 1999, Nucleation of intragranular ferrite at Ti_2O_3 particle in low carbon steel, Acta Materialia, 47(9), pp2751-2760.

[73] Gregg, J. M., & Bhadeshia, H. K. D. H., 1994, Bainite nucleation from mineral surfaces, Acta metallurgica et materialia, 42(10), pp3321-3330.

[74] Xiong, Z., Liu, S., Wang, X., Shang, C., & Misra, R. D. K., 2015, Relationship between crystallographic structure of the Ti_2O_3/MnS complex inclusion and microstructure in the heat-affected zone (HAZ) in steel processed by oxide metallurgy route and impact toughness, Materials Characterization, 106, pp232-239.

[75] Uto, K., Nakayama, K., Kisaka, Y., Kimura, F., and Terasaki, H., 2019, A Study on the Acicular Ferrite Formation in Steel Weld Metals for Gas Metal Arc Welding, Visualization in Joining & Welding Science through Advanced Measurements and Simulation, Proceeding, pp115-116.

[76] Terashima, S., & Bhadeshia, H. K. D. H., 2006, Changes in toughness at low oxygen concentrations in steel weld metals, Science and Technology of Welding & Joining, 11(5), pp509-516.

[77] Taniguchi. S, Sigesato. G., 2014, The Refinement Mechanism of Heat Affected Zone Microstructures on TiO Steels, Nippon Steel & Sumitomo Metal Technical Report, Vol.40.

[78] Babu, S. S., 2004. The mechanism of acicular ferrite in weld deposits, Current opinion in Solid state and Materials Science, 8(3), pp267-278.

[79] Yurioka, N., Horii,Y., Wakabayashi, M., Matsui, H., Tamehiro, H., Kimura, T., 1988, Heat-affected-zone hard- ness of SAW weld metals, Document IX-1524-88,IIW,Viennna

[80] ASTM G39 Standard Practice for Preparation and Use of Bent-Beam Stress-Corrosion test Specimens

[81] Ichitani, K., Kanno, M., & Kuramoto, S., 2003, Recent development in hydrogen microprint technique and its application to hydrogen embrittlement, ISIJ international, 43(4), pp496-504.

[82] Ichitani, K., Kuramoto, S., & Kanno, M., 2003, Quantitative evaluation of detection efficiency of the hydrogen microprint technique applied to steel, Corrosion science, 45(6), pp1227-1241.

[83] Ichitani, K., & Kanno, M., 2003, Visualization of hydrogen diffusion in steels by high sensitivity hydrogen microprint technique. Science and Technology of Advanced materials, 4(6), pp545-551.

[84] Koyama, M., Yamasaki, D., Nagashima, T., Tasan, C. C., & Tsuzaki, K., 2017, In situ observations of silver-decoration evolution under hydrogen permeation: Effects of grain boundary misorientation on hydrogen flux in pure iron, Scripta Materialia, 129, pp48-51.

[85] Lopez, H. F., Raghunath, R., Albarran, J. L., & Martinez, L., 1996, Microstructural aspects of sulphide stress cracking in an API X-80 pipeline steel, Metallurgical and Materials Transactions A, 27(11), pp3601-3611.

[86] Asahi,H., 2000, Hydrogen Embrittlement in Oil Country Tubular Goods and Line Pipes, Zairyo-to-Kankyo, 49(4), pp201-208. (Japanese)

[87] Hamada, M., 2011, Pipelines (materials), Journal of the Japan Welding Society, 80(2), pp180-187. (Japanese)

[88] The Japan Welding Engineering Society webpage, http://www-it.jwes.or.jp/weld_simulator/en/cal4.jsp, accessed 5 August 2018.

[89] Yamabe, J., Awane, T., & Matsuoka, S., 2015, Investigation of hydrogen transport behavior of various low-alloy steels with high-pressure hydrogen gas, International Journal of hydrogen energy, 40(34), pp11075-11086.

[90] Yamabe, J., Yoshikawa, M., Matsunaga, H., & Matsuoka, S., 2017, Hydrogen trapping and fatigue crack growth property of low-carbon steel in hydrogen-gas environment, International Journal of Fatigue, 102, pp202-213.

[91] Matsunaga, H., Yoshikawa, M., Kondo, R., Yamabe, J., & Matsuoka, S., 2015, Slow strain rate tensile and fatigue properties of Cr–Mo and carbon steels in a 115 MPa hydrogen gas atmosphere, International Journal of hydrogen energy, 40(16), pp5739-5748.

[92] Jenkins, N., Hart, P. H. M. H., & Parker, D. H., 1997, An evaluation of rapid methods for diffusible weld hydrogen, Welding Journal-Including Welding Research Supplement, 76(1), pp1-6.

[93] Hadam, U., & Zakroczymski, T., 2009, Absorption of hydrogen in tensile strained iron and high-carbon steel studied by electrochemical permeation and desorption techniques, International Journal of Hydrogen Energy, 34(5), pp2449-2459.

[94] Jiang, Y. F., Zhang, B., Zhou, Y., Wang, J. Q., Han, E. H., & Ke, W., 2018, Atom probe tomographic observation of hydrogen trapping at carbides/ferrite interfaces for a high strength steel, Journal of Materials Science & Technology, 34(8), pp1344-1348.

[95] Beidokhti, B., He, P., Kokabi, A. H., & Dolati, A., 2017, Control of hydrogen cracking in the welded steel using microstructural traps, Materials Science and Technology, 33(4), pp408-414.

[96] Takahashi, J., Kawakami, K., & Kobayashi, Y., 2018, Origin of hydrogen trapping site in vanadium carbide precipitation strengthening steel, Acta Materialia, 153, pp193-204.

List of publications

Kisaka, Y., & Gerlich, A. P., 2016, July, Review and critical assessment of hardness criterion to avoid sulphide stress cracking in pipeline welds, In *ASME 2016 Pressure Vessels and Piping Conference*, American Society of Mechanical Engineers Digital Collection.

Kisaka, Y., & Gerlich, A. P., 2015, A study on Effects on Titanium and Oxygen Contents in GMA welds in order to maximize acicular ferrite volume fraction, *CWA Journal December, pp.58-65.*

Kisaka, Y., & Gerlich, A.P. , 2016, Effects of Titanium and Oxygen to Maximize Intragranular (Acicular) Ferrite Volume Fraction in GMA Welds, *10th International Conference on Trends in Welding Research & 9th International Welding Symposium of Japan Welding Society (9WS), Tokyo, Japan*, Oct.11-14

Kisaka, Y., Senior, N., & Gerlich, A. P., 2019, A Study on Sulphide Stress Cracking Susceptibility of GMA Girth Welds in X80 Grade Pipes. *Metallurgical and Materials Transactions A*, *50*(1), 249-256.

Kisaka. Y., Gerlich. A. P., 2019, "The effects of hydrogen embrittlement on the properties of high strength steel welds." *Canweld conference 2019*, Halifax, Nova Scotia, Canada.